

Three-Dimensional Electromagnetic Imaging of Porphyry Copper Deposits with MT and ZTEM
Data

by

Benjamin Lee

A thesis submitted in partial fulfillment of the requirements for the degree of

Master of Science

in

Geophysics

Department of Physics
University of Alberta

© Benjamin Lee, 2015

Abstract

This thesis investigates the use of the airborne Z-Axis Tipper Electromagnetic (ZTEM) and ground-based magnetotelluric (MT) exploration techniques to image electrical resistivity contrasts associated with porphyry copper deposits. These techniques were individually used to construct three-dimensional (3-D) electrical resistivity models of the Morrison porphyry copper deposit that contain resistivity contrasts caused by hydrothermal alteration, faulting, and possibly sulfide mineralization. The MT resistivity model, which incorporated electric and magnetic field data, correlates very well with the ZTEM resistivity model which only used magnetic field data. 3-D joint ZTEM-MT inversions showed that with appropriate data weighting, the joint resistivity models contained shallow features from the ZTEM data as well as deeper structure required by the MT data. For deposits that require investigation below a depth of about 2 km, there is value in following up a ZTEM survey with a small-scale MT survey to constrain absolute resistivity values and to provide information about deeper structure.

Acknowledgments

I would like to thank members of the MT group at the University of Alberta, past and present, for their support and helpfulness during my time here: Greg Nieuwenhuis, Juliane Hübert, Matthew Comeau, Mitch Liddell, Enci Wang, Darcy Cordell, and particularly my supervisor Dr. Martyn Unsworth for his guidance and advice.

Collection of the MT data used in this study would not have been possible without the aid of Juliane Hübert, Paulina Hauf, Bahman Abbassi, Lijuan Liu, Jean-Baptiste Tary, and Walcott Geoscience.

Thanks to all the participants in this NSERC-funded collaboration between the University of Alberta, l'Université du Québec en Abitibi-Témiscamingue, the University of British Columbia, Amarc Resources Ltd., Geotech Ltd., and Gerald G. Carlson and John A. Chapman. I also thank Pacific Booker Minerals Inc. for providing access to their drill core and property. Computational resources for this study were provided by the Compute Canada Westgrid clusters.

Finally, I would like to thank my friends and my mother, father, and sister for continually supporting me throughout my studies.

Table of Contents

Chapter 1: Introduction.....	1
Chapter 2: Physics of the MT and ZTEM Methods.....	4
2.1 Introduction.....	4
2.2 Electromagnetic Wave Propagation in a Conductive Earth.....	6
2.3 Electromagnetic Skin Depth	9
2.4 Impedance and Apparent Resistivity	12
2.5 Dimensionality.....	16
2.6 Distortion	17
2.7 Vertical magnetic field transfer functions and the tipper.....	18
2.8 MT and ZTEM Responses of a Synthetic Porphyry Model.....	20
2.8.1 Forward Modeling.....	22
2.8.2 Synthetic ZTEM Inversion.....	26
2.8.3 Synthetic MT Inversion	28
2.9 Summary	29
Chapter 3: Geological and Geophysical Aspects of Porphyry Exploration.....	30
3.1 Introduction.....	30
3.2 Porphyry Copper Deposit Alteration and Mineralization.....	33
3.3 Geophysical Response of Porphyry Copper Deposits	35
3.4 The Morrison Deposit	39
3.4.1 Tectonic Setting	39
3.4.2 Deposit Geology	40
3.4.3 Hydrothermal Alteration.....	41
3.5 Summary	42
Chapter 4: Morrison ZTEM and MT Data Analysis.....	43
4.1 Introduction.....	43
4.2 Data Collection	43
4.3 ZTEM Data from the Morrison Deposit	46
4.3.1 Tipper Plots.....	47
4.3.2 Topographic Effect	51
4.4 MT Data at the Morrison Deposit.....	53
4.5 Ground and Airborne Tipper Comparison	58

4.6 Summary	60
Chapter 5: Individual ZTEM and MT Inversions of the Morrison Data	61
5.1 Introduction.....	61
5.2 The Inversion Algorithm.....	63
5.3 ZTEM and MT Data Convention.....	66
5.4 ZTEM Inversion.....	68
5.4.1 Assigning Data Uncertainties.....	70
5.4.2 Initial Model and Mesh.....	70
5.4.3 Single Frequency ZTEM Inversions	72
5.4.4 Spatially Downsampled ZTEM Inversion	74
5.4.5 Effect of the Starting Model.....	77
5.4.6 Preferred ZTEM Inversion Model	78
5.5 MT Inversion	81
5.5.1 Parameters and Initial Model	81
5.5.2 Removal of MT Sites with Significant Distortion	83
5.5.3 Effect of Error Floor	85
5.5.4 Preferred MT Inversion Model	86
5.6 Summary	90
Chapter 6: Joint Inversion of the Morrison MT and ZTEM Data.....	95
6.1 Introduction.....	95
6.2 Methodology.....	96
6.3 Synthetic Joint Inversion Example	98
6.4 Joint Inversion of the Morrison Data	101
6.4.1 Joint Inversion Results	101
6.5 Summary	107
Chapter 7: Interpretation.....	108
7.1 Introduction.....	108
7.2 Model Resistivity Features	109
7.2.1 Deposit Lithology	110
7.2.2 Hydrothermal Alteration	112
7.2.3 Summary of Resistivity Features	116
7.3 Previous EM and Aeromagnetic studies at Morrison	119
7.3.1 Geotech 2-D ZTEM	119

7.3.2 Aeromagnetic Data	120
7.3.3 AeroTEM Late-time Tau	123
7.4 Implications for Exploration at the Morrison Deposit	125
7.5 Implications for Mineral Exploration	125
7.6 Summary	127
Chapter 8: Conclusion	128
8.1 Summary	128
8.2 ZTEM and MT Inversions	129
8.3 Joint ZTEM-MT Inversion.....	130
8.4 Opportunities for Further Work.....	131
References.....	134

List of Figures

- Figure 2.1: Typical broadband magnetotelluric station layout. Two ~ 100 m electric dipoles measure the electric field in the x and y directions and three buried induction coils measure the magnetic field in the x, y, and z directions. The x direction is usually aligned with magnetic north and can be mathematically rotated to other coordinate systems during data analysis.
- Figure 2.2: MT signal propagation in the Earth. The blue line represents the incident wave, the red line is the reflected wave in the air, and the black line is the signal that is transmitted into the ground. Note that most of the incident wave is reflected and only a small fraction of the original amplitude is transmitted into the ground. The left and right sides represent signals with different frequency. The lower frequency 10 Hz signal penetrates deeper than the 40 Hz signal as governed by the skin depth equation. Modified from Unsworth (2014).
- Figure 2.3: Electromagnetic skin depth as a function of signal frequency. Each curve represents a homogeneous halfspace with a different electrical resistivity. For instance, at a frequency of 1 Hz, the signal is able to penetrate about three times deeper in a $10000 \Omega\text{m}$ halfspace than a $1000 \Omega\text{m}$ halfspace.
- Figure 2.4: Two layer resistivity model with a $100 \Omega\text{m}$ layer from 0 – 5 km depth and $10 \Omega\text{m}$ halfspace below. Panel C shows the model resistivity with depth. Panel A shows the apparent resistivity as a function of frequency, and panel B contains the phase angle as a function of frequency. At the highest frequencies the signal is only sampling the upper layer, so apparent resistivity equals the layer resistivity and phase is consistent at 45° . At frequencies lower than 1 Hz the lower conductive layer is detected in the apparent resistivity curve and phase is greater than 45° . When the signal begins to detect the lower layer there is a resonance effect seen as a slight rise in apparent resistivity and a slight decrease in phase angle (details in Section 2.4).
- Figure 2.5: Schematic diagram of a 2-D Earth with $\rho_1 > \rho_2$. Assume the conductive prism extends infinitely in the x-direction. Geoelectric strike is aligned with the x-direction. In the TE mode electric current flows parallel to strike and in the TM mode current flows perpendicular to strike, crossing resistivity boundaries.
- Figure 2.6: In panel A, electric current flowing along the buried 2-D conductive body C (extending infinitely into the page) induces a magnetic field, H . The tipper is the ratio of the vertical to horizontal magnetic field components, and changes sign depending on the observation point. At $y = 1$ km, the magnetic field is oriented in the negative z and positive y directions, so the ratio is negative and the Z/Y tipper component T_{zy} is negative. At $y = 3$ km the magnetic field is oriented in the positive z and positive y directions, so the ratio is positive and T_{zy} is positive. Directly over C at $y = 2$ km, the magnetic field is completely oriented in the y direction, so H_z and T_{zy} are both zero. Panel B shows how the T_{zy} response at the surface varies for different locations over C.

Note that T_{zy} changes sign directly over C, and approaches zero far from C as H decreases in magnitude.

Figure 2.7: Plan view (left) and vertical section (right) of the synthetic porphyry model. The core is a 1 x 1 km wide, 1000 Ωm resistor, surrounded by a 2 x 2 km wide 10 Ωm conductor. These two features extend to 2 km depth and are embedded in a 100 Ωm halfspace. In plan view the black dots represent ZTEM observation points, black lines are the north-south oriented ZTEM flight lines (FL2 and FL 16) shown in Figure 2.10, and sparse white dots are MT station locations. The vertical section is along profile A-A'.

Figure 2.8: Forward modelled tipper data at 90 Hz for the synthetic porphyry model shown in Figure 2.7. Data were computed for the four tipper components at frequencies of 360, 180, 90, 45, and 30 Hz. Two crossover anomalies can be seen in both the real T_{zx} and T_{zy} components as the vertical magnetic field changes direction when crossing over the low resistivity ring. The x-direction is oriented to geographic north, and the y-direction is oriented to geographic east.

Figure 2.9: Map view of real induction arrows of synthetic ZTEM data calculated over the synthetic porphyry model (Figure 2.7). The outlines of the porphyry model are shown in black. The arrow length corresponds to the magnitude of the induction arrows, and therefore the strength of the inductive response. Arrows are plotted in the Parkinson convention, and point toward the conductive 10 Ωm ring.

Figure 2.10: Tipper data for flight lines 2 (top) and 16 (bottom) over the synthetic porphyry model. The positive x-direction is oriented north, and the positive y-direction is oriented east. Flight lines start from the north (0 km) and end in the south (3 km). Red dots are the observed data and blue lines are the inversion model response. Flight line 2 is over the halfspace so there is very little response in the real T_{zx} component. The real T_{zy} component is negative toward the middle of the line due to the magnetic field induced by the conductive ring 500 m to the east. Flight line 16 contains 2 zero-crossovers in the real T_{zx} component when crossing over the conductive ring. The first occurs when crossing from the resistive halfspace to the conductive ring to the highly resistive core, and the second occurs when crossing in the opposite order. The central zero-crossover occurs when passing directly over the resistive core, where vertical magnetic fields induced by opposite sides of the conductive ring cancel each other out. There is no T_{zy} response because there are no induced fields in the y-direction for most of the flight line and the induced fields negate each other directly over the resistive core.

Figure 2.11: Real and imaginary components of the forward modelled MT impedance data for the synthetic porphyry model (Figure 2.7). The off-diagonal impedance components Z_{xy} and Z_{yx} define the resistivity boundaries well, while the diagonal components Z_{xx} and Z_{yy} are more sensitive to the corners where 3-D effects on the electric field direction are largest. The x-direction is oriented to geographic north, and the y-direction is oriented to geographic east.

- Figure 2.12: ZTEM synthetic inversion of the porphyry model at the surface (left) and vertical section through A-A' (right). The forward modeled data at five frequencies (360 – 30 Hz) were inverted with a starting 100 Ωm halfspace. Black lines show the boundaries of features in the original synthetic model (Figure 2.7). The resistivity boundaries and values are well recovered at the surface, but the signal has mostly attenuated by 800 m depth in this moderately conductive model. The lateral boundaries are defined well compared to the synthetic resistivity model, but the recovered model features do not extend to the true 2 km depth.
- Figure 2.13: MT synthetic inversion of the porphyry model at the surface (left) and vertical section through A-A' (right). The forward modeled data at ten frequencies (300 – 0.5 Hz) were inverted on a starting 100 Ωm halfspace. Black lines show the boundaries of features in the original synthetic model (Figure 2.7). The resistivity boundaries are well recovered and there is clearly more depth resolution than the ZTEM inversion.
- Figure 3.1: Worldwide distribution of major porphyry copper deposits. Note the concentration along subduction zones at ancient and modern convergent plate margins. Reproduced with permission from Sillitoe, (2010).
- Figure 3.2: Fluid pathway and resulting alteration pattern of a typical porphyry deposit. High temperature, multi-phase fluid ascends from the magma body emplaced at the level of neutral buoyancy (LNB), and produces potassic alteration at the base of the deposit. As the fluids rise and decrease in temperature the deposit grades outward into phyllic, then propylitic alteration zones. Advanced argillic alteration forms from shallow, low temperature acidic fluids. Reproduced with permission from Richards, (2011).
- Figure 3.3: Geology, alteration, and mineralization of a generalized porphyry deposit and expected geophysical responses for an uneroded and eroded deposit. Panel A: Intrusive body with feeder dikes; Panel B: Typical porphyry system alteration pattern; Panel C: Expected sulfide mineralization, note the pyrite enrichment outside of the potassic core. Panels D-F: Geophysical responses associated with alteration zones. The lower section contains expected response for an uneroded and eroded porphyry deposit. Dashed lines indicate eroded surfaces. Py = pyrite, Cp = chalcopyrite.
- Figure 3.4: Relationship between sulfide weight percentage (x-axis) and resistivity (y-axis) based on in-situ measurements at 109 porphyry deposits. For disseminated or discontinuous veins (< 3% wt.) the resistivity tends to be high and variable. As interconnectivity increases, there is a more direct relationship between increasing sulfide weight percent and decreasing resistivity. Modified from Nelson and Van Voorhis (1983).
- Figure 3.5: Terrane map of British Columbia showing the location of the Morrison deposit within the Stikinia Terrane. Modified from British Columbia Geological Survey, (2005).
- Figure 3.6: Panel A: The location of the Morrison deposit in central British Columbia, Canada. Panel B: The deposit location is outlined by the dashed black box. Copper mineralization is centered on a large (1 km) intrusive body. The deposit is contained within the Morrison

Graben and features two smaller faults that cut through the major copper mineralization zone. Adapted from McClenaghan, (2013) and Robertson, (2009).

Figure 4.1: Geologic map of the Morrison deposit with locations of the ZTEM survey (black lines) and MT survey (black circles with station number). The deposit area is circled in black. Adapted from BCGS Geoscience, (2005).

Figure 4.2: View looking west over the Morrison deposit. The MT data acquisition area was limited by available road access and terrain.

Figure 4.3: In-phase tipper data for ZTEM flight lines L1050 and L1110. The data show a similar trend at all frequencies, but lower frequency data are sensitive to larger scale resistivity contrasts and appear smoother over longer spatial wavelengths. The data diverge considerably at about 4 – 7 km due to varying sensitivity of each frequency to the sharp elevation increase along profile. The x-direction is oriented to geographic north, and the y-direction is oriented to geographic east.

Figure 4.4: Tipper response at Morrison from high (upper) to low (lower) frequency. The left column contains real T_{zx} component and right column is real T_{zy} . The high frequency data are sensitive to shallow resistivity features and topography, while the 30 Hz data are sensitive to deeper resistivity structure. The x-direction is oriented to geographic north, and the y-direction is oriented to geographic east.

Figure 4.5: Elevation of the Morrison survey area from the Shuttle Radar Topography Mission (SRTM) data. Black lines are the 15 ZTEM flight lines. Flight lines L1050 and L1110 are labelled for reference. There is a large contrast between the southwest and northeast portion of the survey, with an elevation change of over 500 m along some flight lines.

Figure 4.6: Forward modelled response of a 1000 Ωm halfspace with the Morrison survey topography. The top row contains the observed T_{zx} data at 360, 90, and 30 Hz while the bottom row shows the forward data at these frequencies. Features in the forward responses must be due to topographic resistivity contrasts. In the 360 Hz forward data some data are between -0.10 and -0.15, the same magnitude as the observed data. This implies that a significant portion of the 360 Hz observed data could be influenced by topography as well as buried conductors. The magnitude of the 90 and 30 Hz forward responses is lower since the tipper is sensitive to larger scale structures at these frequencies. The x-direction is oriented to geographic north, and the y-direction is oriented to geographic east.

Figure 4.7: Apparent resistivity and phases curves for stations MR18, MR24, MR29, and MR32. Red curves represent the xy polarization (electric field oriented in the x-direction) and blue curves are the yx polarization.

Figure 4.8: Measured MT impedance data for each component at a frequency of 8.1 Hz for the Morrison survey. There are deviations from the regional impedance at the northeast portion of the survey area, where the Morrison deposit is located. The x-direction is oriented to geographic north, and the y-direction is oriented to geographic east.

- Figure 4.9: Comparison of airborne ZTEM (red circles) and ground MT (open circles) at four MT stations. There is good agreement for all four tipper components.
- Figure 4.10: Induction arrows for the MT (red) and ZTEM (black) data at a frequency of 30 Hz. The arrows are in good agreement at this frequency. In the Parkinson convention the arrows point toward conductive features.
- Figure 5.1: Example of a rectilinear mesh with a regular cell size (left) and an octree mesh with variable cell size (right). The octree mesh contains many small cells (indicated in blue) in the core region and larger cells (red and pink) near the mesh edges. This allows for a manageable number of total cells while satisfying electromagnetic skin depth conditions to accurately model the electromagnetic fields. Figure generated using UBC-GIF MeshTools3D software.
- Figure 5.2: Sign convention of the Morrison ZTEM survey. Tipper values do not show minimums or maximums above anomalies, instead they exhibit zero-crossovers. Left: The sign of the tipper changes when traveling over a conductor in the positive x-direction from positive to negative. This is due to the change in the direction of the vertical magnetic field component. Right: Cross section view showing the sign change when flying over the same conductor.
- Figure 5.3: Initial inversion misfit using several starting model resistivities. A starting model of 1000 ohm-m was selected for the ZTEM inversion because of the lowest initial misfit.
- Figure 5.4: Core region of the inversion mesh containing 75 x 75 x 75 m cells. White lines are the ZTEM flight lines, and the Morrison deposit is outlined in red. The sharp rise in elevation to the east of the deposit must be finely discretized to accurately reproduce the true topography.
- Figure 5.5: Observed and predicted T_{zx} component data (with x-direction oriented north) for ZTEM inversions with 13,462 observation points (left panel), 6,731 observation points (middle panel) and 1,347 observation points (right panel). In each panel the upper half is the observed data, and the bottom half is the model predicted data. The tipper amplitudes are extremely similar in all three cases, so it is not necessary to invert the entire dataset.
- Figure 5.6: ZTEM inversion model depth slices at 633 m above sea level using all 13,462 ZTEM data points (left), one half (6,731) of the data points (middle), and one tenth (1,347) of the data points (right) The three models are extremely similar in structure and resistivity amplitude.
- Figure 5.7: Horizontal slices of the preferred 3-D ZTEM inversion at three elevations above sea level: (A) 633 m elevation, (B) 484 m elevation, and (C) 333 m elevation. The Morrison deposit appears as a shallow resistive feature, and is bounded by conductors C1 and C2 that correlate with the edges of the Morrison Graben, as well as the pyrite enrichment zone.
- Figure 5.8: Comparison of inversion convergence curves for the MT inversions A (black line), D (red line) and F (blue line). Dashed lines represent the target misfit for each inversion.

Inversions D and F excluded stations with severe galvanic distortion, and resulted in a much more acceptable final misfit.

Figure 5.9: Selected plots of observed and predicted data for MT inversion F at MT stations (A) MR19, (B) MR23, (C) MR28, and (D) MR32. The four components of apparent resistivity and phase (xx , xy , yx , and yy) derived from the MT impedance tensor are shown for each station. Dots are the observed data and lines are the predicted model response. The predicted data match the observed data very closely. The inversion converged to a misfit of 1982 (target 2208).

Figure 5.10: Horizontal slices of the 3-D MT inversion F at (A) 633 m, (B) 483 m, and (C) 333 m elevation above sea level. The Morrison deposit and geologic features are overlain in white, and MT stations are the black circles. The resistivity features C1, C2, R1, and R2 appear in the ZTEM-only inversion as well (see Chapters 5 and 7 for interpretation).

Figure 5.11: Vertical sections through flight line L1110 of the (A) MT inversion model and (B) ZTEM model. Both inversion models contain a shallow, conductive overburden to the west of the deposit (C1). The Morrison deposit contains an outcropping resistive body (R2) that extends to about 500 m below the surface and is flanked to the southwest and northeast (C2) by two conductive features. Hazelton Group volcanics and sediments appear resistive to the northeast (R1). The MT model contains a large conductor below the deposit while the ZTEM model contains a large resistor. Since the MT data misfit was high at lower frequencies, this is likely not a well-constrained feature. The northeastern portion of the MT section is not well resolved because no stations were located in this area.

Figure 5.12: Horizontal slices through the ZTEM and MT inversions at three elevations above sea level: 633 m elevation (A and B), 483 m elevation (C and D), and 333 m elevation (E and F). The same resistivity features present in both ZTEM and MT models are described in section 5.6.

Figure 5.13: Correlation plots for the preferred ZTEM and MT inversions. Using the same mesh, the resistivity of each cell from the ZTEM and MT inversions was plotted at four depths. Darker squares correspond with more occurrences within a specific bin. The dashed grey line is a one-to-one correlation. The correlation appears nearly one-to-one in panels A and B, but is slightly offset because of the different starting models used for each inversion. In panels C and D the correlation is not as clear because the ZTEM inversion begins to lose resolution at these depths.

Figure 6.1: Plan view (left) and vertical section (right) of the synthetic porphyry model. The core is a 1 x 1 km wide, 1000 Ωm resistor, surrounded by a 2 x 2 km wide 10 Ωm conductor. These two features extend to 2 km depth and are embedded in a 100 Ωm halfspace. In plan view the black dots represent ZTEM observation points, grey lines are the ZTEM flight lines (FL2 and FL 16), and sparse white dots are MT station locations.

Figure 6.2: Joint inversion model of the ZTEM and MT data over the synthetic porphyry model (Figure 6.1). The left panel shows a map view at the surface (0 m) and the right shows a

vertical section through 2000 m West. Black lines are the outlines of the original synthetic porphyry model. The joint inversion defines the resistivity boundaries well and has more resolution at depth compared to the ZTEM-only synthetic inversion in Chapter 2 (Figure 2.12).

Figure 6.3: Horizontal slices at 483 m elevation through joint ZTEM-MT inversion models with various MT data weights. The diagonal thick black line represents flight line L1110. The main BFP stock and dikes are overlain in white, along with the bounding faults of the Morrison Graben. Black circles are MT stations and thin black lines are the extent of the ZTEM survey. As the MT data error is decreased, the relative weighting of the MT data in the inversion is increased. In panels A-H it is clear that the inversion is incorporating information about absolute resistivity values from the MT data. The inversions in panels I and J were not able to fit the ZTEM and MT data, and do not contain the same features as the other inversions.

Figure 6.4: Vertical slices through joint inversion models with various MT data weights. As the MT error is decreased, the relative weighting of the MT data increases in the joint inversion and features required by the MT data should be replicated in the resistivity model. The inversions in panels F – H appear to be including the most structure from the MT data as there are features below the resolution of the higher frequency ZTEM data. In panels I – J the inversion is not able to closely fit either dataset, and the model does not change appreciably from the starting 1000 Ωm . Resistivity features are labelled as C1, C2, R1, and R2 (see text for interpretation).

Figure 7.1: Horizontal slices through ZTEM inversion model (A,C,E) and MT inversion model (B,D,F) at 633 m, 483 m, and 333 m elevation above sea level. Red colors represent conductive features while blue features are more resistive. The Morrison orebody and 3 BFP dikes are outlined in white, along with the bounding faults of the Morrison Graben. Black dots are MT station locations. The flight line L1110 is the profile for the vertical sections. Thin black lines show the spatial extent of the ZTEM survey. The resistive feature R2 and the conductive C2 may be associated with hydrothermal alteration, and appear in both the ZTEM and MT models. C1 and R1 are consistent with the known deposit lithologies.

Figure 7.2: Horizontal slices at 483 m elevation through joint ZTEM-MT inversion models. From panels A to J the MT data error is decreased in order to increase the relative weight of the MT data in the joint inversion. The diagonal thick black line represents flight line L1110. The main BFP stock and dikes are overlain in white, along with the bounding faults of the Morrison Graben. Black circles are MT stations and thin black lines are the extent of the ZTEM survey. As the MT data error is decreased, the relative weighting of the MT data in the inversion is increased. In panels A-H it is clear that the inversion is incorporating information about absolute resistivity values from the MT data. The inversions in panels I and J were not able to fit the ZTEM and MT data, and do not contain the same features as the other inversions.

Figure 7.3: Vertical slices along ZTEM flight line L1110 through joint inversion models. Between panels A – J the MT error is lowered to increase the relative weighting of the MT data in the joint inversion. The resistivity models in panels A – E are not very different from the ZTEM-only model since the inversion does not closely fit the MT data. In panels F – H the joint inversion is clearly adding deeper structure that is required as the MT weighting is increased. In panels I – J the MT data error is too low and the inversion cannot closely fit the data or recover a reasonable model.

Figure 7.4: Panel A: Vertical section through flight line L1110 of the preferred 3-D ZTEM inversion from Chapter 5 and B) 2-D ZTEM inversion by Geotech Ltd. of Morrison flight line L1110. Both inversions started with a 1000 Ωm starting model. The 2-D inversion used the in-line T_{zx} component at five frequencies between 360 – 30 Hz. The deposit potassic zone and flanking conductors correlate very well with their positions in the 3-D ZTEM inversion. (Modified from Legault, pers. comm., 2013.)

Figure 7.5: Comparison of ZTEM inversion resistivity model, TEM late-time tau data, and airborne total magnetic intensity map of the Morrison deposit. Panel A: Horizontal section of the ZTEM only inversion at 633 m elevation above sea level. Panel B: AeroTEM late time tau map from Aeroquest Surveys (2009). Larger values of tau correspond to lower resistivity. Panel C: Morrison total magnetic intensity map from Aeroquest Surveys (2009).

Figure 7.6: Time domain electromagnetic (TEM) survey with transmitting loop (TX), receiver (RX), secondary electric current (I_s) and induced secondary magnetic field (H_s). The resistivity of the Earth is determined by measuring the time decay of the secondary magnetic fields at the receiver. Modified from Unsworth, (2014).

List of Tables

Table 5.1: Survey conventions and corrections for the Morrison ZTEM and MT data.

Table 5.2: Inversion parameters for single frequency inversions of the Morrison ZTEM data.

Table 5.3: Inversion parameters for the down-sampled inversions of the Morrison ZTEM data.

Table 5.4: Inversion parameters for the Morrison ZTEM starting model test inversions.

Table 5.5: Inversion parameters for several trial MT inversions. Diagonal and off-diagonal are the diagonal (Z_{xx} and Z_{yy}) and off-diagonal (Z_{xy} and Z_{yx}) terms in the impedance tensor.

Table 7.1: Resistivity features at the Morrison deposit. The second column indicates the geologic or alteration feature interpreted to cause the resistivity feature. Columns 3 – 7 list whether or not the features were present in various EM studies.

List of Symbols and Abbreviations

1-D	One dimensional
2-D	Two dimensional
3-D	Three dimensional
AFMAG	Audio Frequency Magnetics
ATEM	Airborne Time Domain Electromagnetic
BFP	Biotite feldspar porphyry
C1	Conductor 1
C2	Conductor 2
Cp	chalcopyrite
CSEM	Controlled Source Electromagnetic
EM	Electromagnetic
IP	Induced polarization
LJHG	Lower Jurassic Hazelton Group
Ma	Millions of years ago
MLJB	Mid-Late Jurassic Bowser Group
MT	Magnetotellurics
Py	Pyrite
QS	Quaternary glaciolacustrine sediments
R1	Resistor 1
R2	Resistor 2
TE	Transverse electric
TEM	Time Domain Electromagnetic
TM	Transverse magnetic
UAS	Unmanned aircraft system
ZTEM	Z-Axis Tipper Electromagnetic

Chapter 1: Introduction

This thesis is motivated by the need to improve the techniques used in exploration for porphyry copper deposits, which currently provide almost 75% of the world's copper (Sillitoe, 2010). Because these deposits are formed at depth within the Earth it is impossible to observe their formation, and extensive exploration is required to understand the structure of each deposit. In addition, these deposits may experience different amounts of erosion making some mineral deposits more easily discovered than others. A combination of geologic mapping, near-surface geophysical methods, geochemistry, and drilling has proven effective at investigating deposits up to a few hundred meters below the surface. However, the need for deeper exploration methods has increased as most shallow porphyry deposits have been discovered. Geophysical methods can fill this need as a cost-effective way to obtain deeper targets for drilling.

Electromagnetic (EM) methods are employed to detect metallic sulfide deposits based on their electrical resistivity contrasts compared to the host rock. For instance, time domain EM methods (TEM) with a transmitter are particularly effective at detecting materials with large resistivity contrasts, such as low resistivity massive sulfides. These systems can be deployed quickly and inexpensively from an airborne platform. However, as targets are located at greater depth their measured TEM response at the surface becomes weaker. In addition, deposits containing disseminated sulfides, where the sulfides occur as individual crystals within the rock matrix, have smaller resistivity contrasts that may not be detected with TEM. Unlike TEM, natural source EM methods do not rely on measuring the transient decay of a transmitted signal and have a much larger depth of investigation. The ground-based magnetotelluric (MT) method measures electric and magnetic fields to determine subsurface resistivity at greater depths than

Chapter 1: Introduction

controlled-source techniques. However, since ground contact is needed to measure the electric fields, MT surveys are more costly and do not have the same spatial coverage as airborne methods. The airborne Z-Axis Tipper Electromagnetic (ZTEM) method (Lo and Zang, 2008) provides the spatial coverage of an airborne technique with the investigative depth of a natural-source method. Originally conceived as the Audio-Frequency (AFMAG) technique (Ward, 1959), the ZTEM system can resolve resistivity contrasts from the surface to a depth of 2 km based on time variations in the earth's naturally occurring magnetic field. Despite these strengths, the ZTEM method lacks information about absolute resistivity values since it does not measure electric fields. While relative resistivity contrasts contain valuable information, the actual background resistivity is necessary to create a resistivity model from ZTEM data that is comparable with models derived from other exploration techniques. To utilize the strengths of each technique, airborne ZTEM data could be combined with sparse ground MT data as a more cost effective exploration strategy (Holtham, 2012).

Chapter 2 reviews the basic principles behind the ZTEM and MT exploration techniques. While each method uses EM induction, it is important to realize that each technique has a different sensitivity to subsurface resistivity because ZTEM only measures magnetic fields and MT measures both electric and magnetic fields. Despite this, data from ZTEM and MT surveys can both be used to recover a three dimensional (3-D) resistivity model of the subsurface using the same automated inversion algorithm. I present synthetic modeling examples to show the resolution of the individual ZTEM and MT data, as well as both datasets simultaneously, in resolving the resistivity of an idealized porphyry deposit.

Chapter 3 summarizes the current role of geophysics in exploration for porphyry deposits. The latest geologic models of porphyry deposits suggest that there are resistivity

Chapter 1: Introduction

contrasts that could be imaged with natural-source EM methods such as ZTEM and MT. I introduce the geologic setting of the Morrison porphyry deposit in British Columbia, the case study for this thesis.

Chapter 4 describes the ZTEM and MT surveys conducted at the Morrison deposit. I discuss general characteristics of the data and show that the magnetic field data from ground MT and airborne ZTEM correlate very well.

In Chapter 5 the concept of geophysical inversion will be introduced, as well as the inversion algorithm used to create resistivity models from the observed ZTEM and MT data. The inversion must follow a logical procedure including mesh design, assigning data uncertainties, and choosing a starting model. Following these steps, I examine preliminary inversions before presenting preferred inversions from the individual ZTEM and MT data.

Chapter 6 investigates the method of jointly inverting the ZTEM and MT data to create one resistivity model. Jointly inverting two different datasets requires more data preparation, and one challenge is properly weighting the two datasets. I show joint inversions of the Morrison data using different weighting parameters. The results are promising as it is clear the inversion is incorporating information from both the ZTEM and MT datasets.

In Chapter 7 the resistivity features from the ZTEM and MT inversion models are correlated with known geologic features and hydrothermal alteration. The resistivity models also contain features seen in a 2-D inversion of the ZTEM data by Geotech Ltd, an aeromagnetic survey by Aeroquest Surveys (2009), and a time-domain AeroTEM survey. Finally, I evaluate difficulties encountered in this study and suggest improvements for a joint ZTEM-MT mineral exploration strategy.

Chapter 2: Physics of the MT and ZTEM Methods

2.1 Introduction

The airborne Z-Axis Tipper Electromagnetic (ZTEM) and ground magnetotelluric (MT) techniques were used to study the Morrison porphyry copper deposit. Both these methods use naturally occurring radio waves to image the subsurface electrical resistivity structure of the Earth. The naturally occurring electromagnetic (EM) signals can be divided into high frequency (> 1 Hz) and low frequency (< 1 Hz) bands. The low frequency band comes from deflections of the solar wind by Earth's magnetosphere. These interactions generate large electric currents in the ionosphere, the atmospheric region of electrically conductive particles up to 1000 km above the surface. These changes in current generate the low frequency (< 1 Hz) magnetic fields measured at the Earth's surface. Signals in the high frequency band (> 1 Hz) originate from worldwide lightning activity. ZTEM measures higher frequency signals in the band 720 - 30 Hz, while MT measures a broader range of frequencies (1000 - 0.001 Hz) originating in both global lightning and the magnetosphere.

As the EM signals enter the Earth, the rate at which they decay with depth is determined by their frequency and the subsurface conductivity (or reciprocal, resistivity). The MT technique measures perpendicular electric and magnetic fields at the surface of the Earth at varying frequencies to determine the electrical resistivity of the Earth (Tikhonov, 1950; Cagniard, 1953). A typical MT station measures five field components: two orthogonal electric field components (x and y) and three orthogonal magnetic field components (x, y, and z). As shown in Figure 2.1, the electric field components E_x and E_y are measured between two buried, non-polarizing

electrodes separated by a distance of approximately 100 m. In a broadband MT survey (1000 – 0.001 Hz) the three, mutually orthogonal, magnetic field components H_x , H_y , and H_z , are each measured with a magnetic induction coil. For low frequency measurements a fluxgate magnetometer with a lower sampling rate provides absolute magnetic field measurements of all three components. For practicality, the x-direction is usually aligned with magnetic north and data can be subsequently rotated to another coordinate system during data analysis (details in Chapter 4).

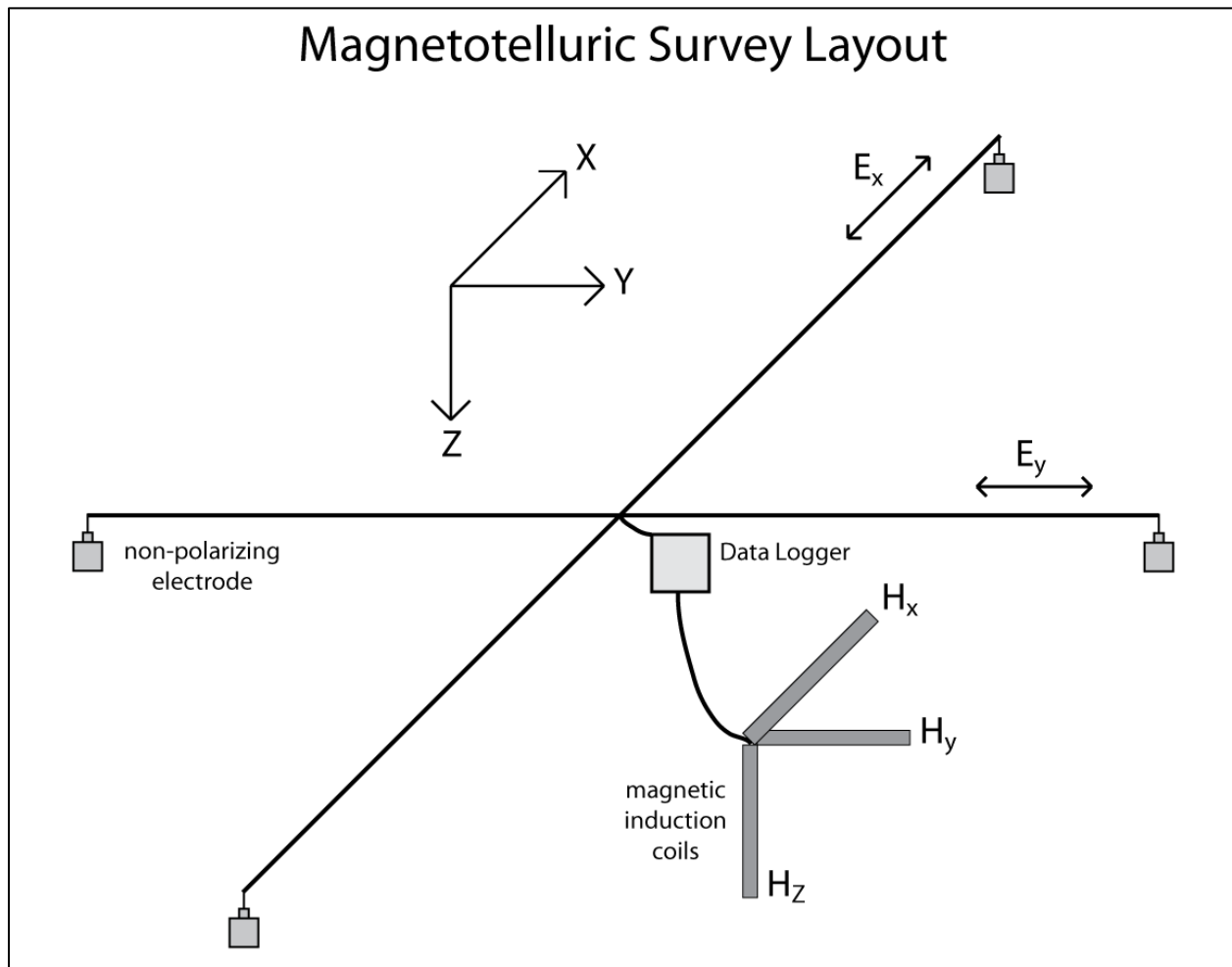


Figure 2.1: Typical broadband magnetotelluric station layout. Two ~100 m electric dipoles measure the electric field in the x and y directions and three buried induction coils measure the magnetic field in the x, y, and z directions. The x direction is usually aligned with magnetic north and can be mathematically rotated to other coordinate systems during data analysis.

Chapter 2: Physics of the MT and ZTEM Methods

MT stations require ground contact to measure the electric field and can be slow and relatively expensive to deploy in rugged terrain. While airborne surveys can collect EM data more rapidly, methods to measure the electric field in the air are still being developed (Macnae, 2010; Gurk et al., 2013) and have not been adapted for an airborne platform. However, measurements of just the three magnetic field components can still provide valuable information about the Earth's resistivity structure. The airborne Audio Frequency Magnetic (AFMAG) technique was developed to detect buried conductors based on the tilt angle of the magnetic field (Ward, 1959). This airborne technique was unique for using low frequency, natural EM fields, providing a greater penetration depth than other conventional EM methods. ZTEM is an extension of the AFMAG technique that was redeveloped by Geotech Ltd. and which measures subsurface resistivity contrasts with measurements of the vertical magnetic field with an airborne sensor and the horizontal fields with a stationary base station (Lo and Zang, 2008). While the MT and ZTEM techniques use the same signal source, electric field measurements made during an MT survey provide an estimate of the absolute value of subsurface electrical resistivity, while ZTEM provides just information about spatial contrasts in electrical resistivity structure. The theory of EM signal propagation in the Earth will be presented in the following sections, along with synthetic examples to help understand the data response of each technique.

2.2 Electromagnetic Wave Propagation in a Conductive Earth

The behavior of EM signals in the Earth is governed by Maxwell's Equations (Maxwell, 1861) and listed below as equations 2.1 - 2.4. In these equations, the Earth properties relevant to EM signal propagation are defined by three quantities:

Chapter 2: Physics of the MT and ZTEM Methods

(1) Electrical resistivity (ρ): This property quantifies how well a material opposes the flow of electric current, and is measured in ohm meters (Ωm). The reciprocal, electrical conductivity (σ), is commonly used and is measured in Siemens per meter (S/m).

(2) Magnetic permeability (μ): Magnetic permeability is the ability of a material to support an internal magnetic field, measured in Henries per meter (Hm^{-1}). At the atomic level, this property quantifies how well individual atoms within a material align to an applied magnetic field.

(3) Dielectric permittivity (ϵ): A material's electric permittivity is the measure of how much it opposes the formation of an internal electric field in farads per meter (Fm^{-1}). Individual particles within a material may be polar and act as small electric dipoles that preferentially align in an applied electric field.

To relate these properties to EM signal propagation, consider Maxwell's Equations in their general form:

$$\nabla \cdot \mathbf{E} = \frac{Q}{\epsilon} \quad (2.1)$$

$$\nabla \cdot \mathbf{B} = 0 \quad (2.2)$$

$$\nabla \times \mathbf{E} = -\frac{\partial \mathbf{B}}{\partial t} \quad (2.3)$$

$$\nabla \times \mathbf{B} = \mu\sigma\mathbf{E} + \mu\epsilon\frac{\partial \mathbf{E}}{\partial t} \quad (2.4)$$

where $\mathbf{B}(x,y,z,t)$ is the magnetic flux density, $\mathbf{E}(x,y,z,t)$ is the electric field, Q is the electric charge per unit volume, t is time, μ is the magnetic permeability, ϵ is the dielectric permittivity, and σ is electrical conductivity (the inverse of resistivity). The x,y,z coordinates are defined using the right-hand rule, with the z -direction oriented downward into the earth. Gauss's Law (Eq. 2.1) relates the amount of electric field flux to the amount of charge enclosed in a surface.

Eq. 2.2 states that there are no magnetic monopoles. This means that magnetic field lines are always closed loops and the net magnetic flux through any closed surface is always zero. Faraday's Law (Eq. 2.3) states that a time-varying magnetic field induces an electric field. The opposite effect is observed in Ampère's Law (Eq. 2.4) where a time-varying electric field or a static electric current produces a magnetic field.

Now we will use Maxwell's Equations to understand how an EM signal propagates in the Earth. Taking the curl of Faraday's Law (Eq. 2.3) and substituting into Ampere's Law (Eq. 2.4), we obtain a second order differential equation for the time-varying electric field. If we assume that the properties of the Earth (μ, σ, ϵ) do not vary with time and there are no free electric charges below ground (i.e. right hand side of Eq. 2.1 equals zero), the electric field satisfies the equation:

$$\nabla^2 \mathbf{E} = \mu\sigma \frac{\partial \mathbf{E}}{\partial t} + \mu\epsilon \frac{\partial^2 \mathbf{E}}{\partial t^2} \quad (2.5)$$

To simplify analysis we transform to the frequency domain, assuming the time variation of the EM signal is harmonic with an angular frequency ω :

$$\mathbf{E}(x, y, z, t) = \mathbf{E}_0(x, y, z)e^{-i\omega t} \quad (2.6)$$

where $i = \sqrt{-1}$ and angular frequency ω is related to frequency f by $\omega = 2\pi f$.

Thus Eq. 2.5 can be written as:

$$\nabla^2 \mathbf{E}_0 = -i\omega\mu\sigma \mathbf{E}_0 + \omega^2\mu\epsilon \mathbf{E}_0 \quad (2.7)$$

The first term on the right-hand side of Eq. 2.7 is the conduction current and the second term is the displacement current. The conduction current depends on the conductivity of the media while the displacement current depends on the dielectric permittivity. For our applications in the Earth, the signal frequency ω is never high enough, nor is the conductivity σ low enough for the displacement current term to dominate the right-hand side of equation 2.7. This means that the

conduction current dominates, and the signal will diffuse through conductivity boundaries instead of travelling as an electromagnetic wave in the subsurface. Thus, neglecting the displacement current term, Eq. 2.7 simplifies to:

$$\nabla^2 \mathbf{E}_0 = -i\omega\mu\sigma\mathbf{E}_0 \quad (2.8)$$

As seen in Eq. 2.8, electric permittivity has no effect on the signal propagation in the diffusion case. In the opposite case, a low conductivity or high signal frequency will cause the displacement current to dominate:

$$\nabla^2 \mathbf{E}_0 = \omega^2\mu\varepsilon\mathbf{E}_0 \quad (2.9)$$

In Eq. 2.9 it is clear that the subsurface conductivity does not affect the signal wave propagation. The ground-penetrating radar technique utilizes signal with frequency $1 \times 10^8 - 1 \times 10^9$ Hz, and is an example of the signal traveling as a wave below ground. Conversely, in the following chapters the MT and ZTEM applications use lower frequency signal in the range $1 \times 10^{-3} - 1 \times 10^3$ Hz, and the signal will travel by diffusion (Eq. 2.8) since the conduction current is several orders of magnitude larger than the displacement current.

2.3 Electromagnetic Skin Depth

Eq. 2.8 shows that the propagation of the EM signal depends on the conductivity and magnetic permeability of the subsurface as well as the signal frequency ω . Equation 2.8 can be solved in general for any EM field with arbitrary geometry. However, to understand the underlying physics, consider the simple case when the electric field is polarized in the horizontal x-direction and the wave is planar i.e. no variations in x and y directions. Figure 2.2 illustrates this simple case when the electric field has a harmonic variation and is polarized in the x-direction. While most of the incident signal is reflected at the Earth-air interface, a small

proportion of the signal diffuses into the Earth. To solve for the signal behavior as it enters the ground, it can be shown that a solution of Eq. 2.8 is of the form

$$|E_x(z)| = |E_x^s| e^{-\sqrt{\frac{\omega\mu\sigma}{2}}z} \quad (2.10)$$

where the electric field decreases exponentially with depth, z , and E_x^s is the electric field at the surface (Simpson and Bahr, 2005). The electromagnetic skin depth is defined as the depth at which the modulus of the electric field has decayed by $1/e$. This requires that when z equals the skin depth, δ ,

$$\sqrt{\frac{\omega\mu\sigma}{2}} \delta = 1 \quad (2.11)$$

Assuming the magnetic permeability has the free space value ($\mu = \mu_0$ if no large magnetic bodies are present), Eq. 2.11 can be simplified to:

$$\delta \approx \frac{500}{\sqrt{\sigma f}} \quad (2.12)$$

This shows that the penetration depth of an EM signal is controlled by its frequency and the conductivity of the Earth. Since the signal will travel diffusely, at a given frequency f the value of σ is the average conductivity of a hemisphere with radius δ measured in meters. For a halfspace with conductivity σ , higher frequency signals will have a smaller penetration depth than lower frequency signals. This is illustrated in Figure 2.3, which shows the skin depth as a function of frequency for four homogeneous halfspaces with different resistivity.

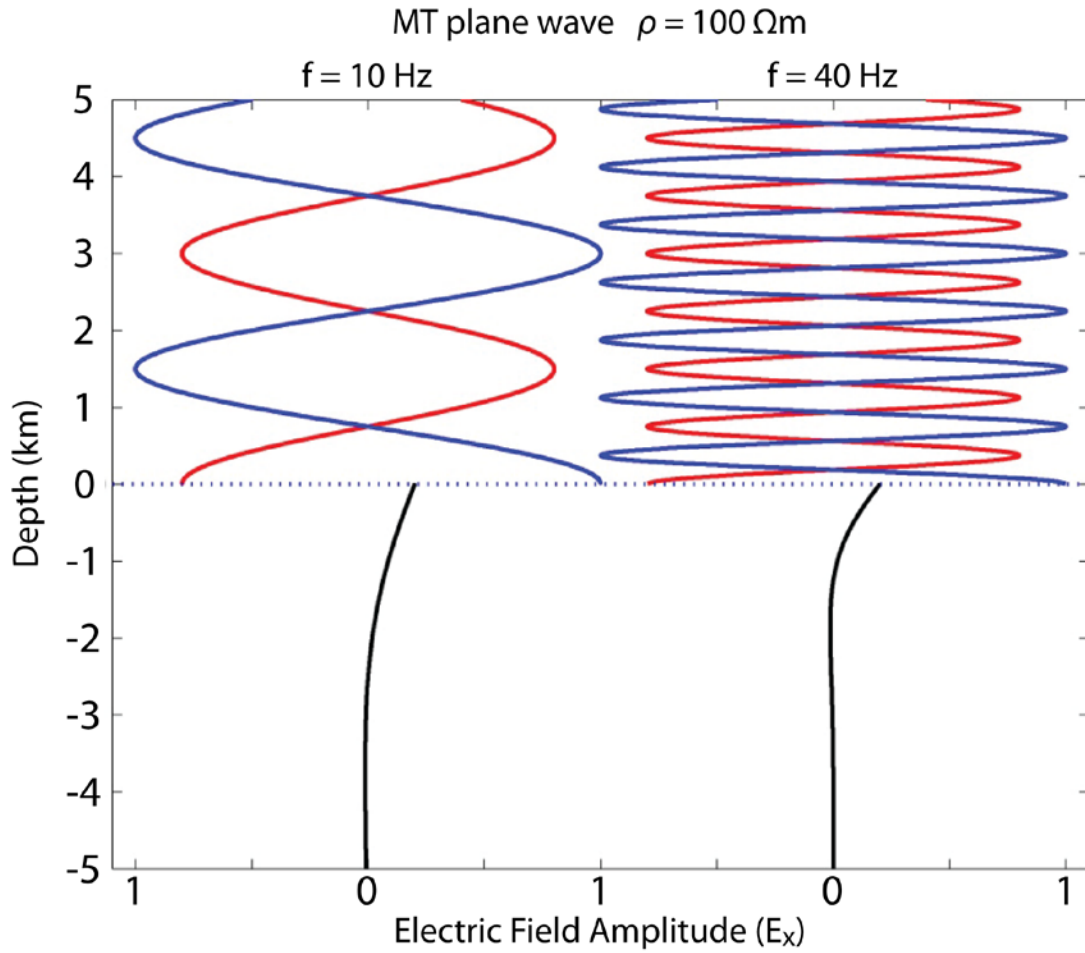


Figure 2.2: MT signal propagation in the Earth. The blue line represents the incident wave, the red line is the reflected wave in the air, and the black line is the signal that is transmitted into the ground. Note that most of the incident wave is reflected and only a small fraction of the original amplitude is transmitted into the ground. The left and right sides represent signals with different frequency. The lower frequency 10 Hz signal penetrates deeper than the 40 Hz signal as governed by the skin depth equation. Modified from Unsworth (2014).

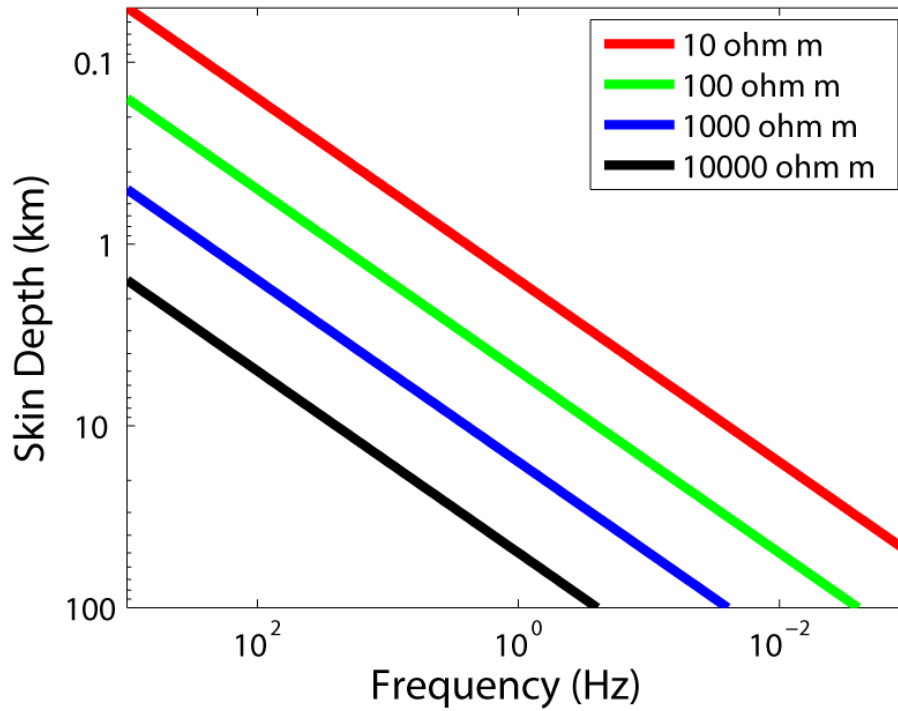


Figure 2.3: Electromagnetic skin depth as a function of signal frequency. Each curve represents a homogeneous halfspace with a different electrical resistivity. For instance, at a frequency of 1 Hz, the signal is able to penetrate about three times deeper in a 10000 Ωm halfspace than a 1000 Ωm halfspace.

2.4 Impedance and Apparent Resistivity

MT data are collected as a time series of 3 mutually perpendicular magnetic field components and 2 horizontal electric field components, for a total of five recording channels. Assuming the signal is time varying with a harmonic time dependence $e^{-i\omega t}$, the electric and magnetic fields are transformed into the frequency domain. These are used to calculate the impedance tensor Z , defined as:

$$\begin{bmatrix} E_x(\omega) \\ E_y(\omega) \end{bmatrix} = \begin{bmatrix} Z_{xx}(\omega) & Z_{xy}(\omega) \\ Z_{yx}(\omega) & Z_{yy}(\omega) \end{bmatrix} \begin{bmatrix} H_x(\omega) \\ H_y(\omega) \end{bmatrix} \quad (2.13)$$

where the electric field E , magnetic field H , and impedance Z are complex functions of angular frequency ω . The apparent resistivity ρ_{xy} , which is derived from the impedance, is the average resistivity of a hemisphere with radius equal to the skin depth at angular frequency ω :

$$\rho_{xy}(\omega) = \frac{1}{\omega\mu_0} \left| \frac{E_x(\omega)}{H_y(\omega)} \right|^2 \quad (2.14)$$

where ρ_{xy} is the apparent resistivity calculated from the electric field oriented in the x-direction and the magnetic field in the y-direction. Magnetic permeability is assumed equal to its free space value.

Another parameter used to describe the behavior of EM signal below ground is the impedance phase. This is the phase angle between orthogonally polarized, horizontal electric and magnetic components, for instance E_x and H_y . Since the impedance is a complex tensor, it can be expressed as the product of a real magnitude and an imaginary phase:

$$Z_{xy}(\omega) = |Z_{xy}(\omega)| e^{-i\phi(\omega)} \quad (2.15)$$

where $\phi(\omega)$ is the phase angle between E_x and H_y . The phase is sensitive to whether the apparent resistivity ρ_a is increasing or decreasing with period T (inverse of frequency f):

$$\phi \approx \frac{\pi}{4} \left(1 - \frac{\partial \log \rho_a}{\partial \log T} \right) \quad (2.16)$$

From Eq. 2.16, if the apparent resistivity does not change with period (i.e. a halfspace) then the phase will be $\frac{\pi}{4}$ (equal to 45°) at all periods. If the apparent resistivity increases with period, then $\frac{\pi}{4}$ will be multiplied by a term smaller than one, and the phase is less than $\frac{\pi}{4}$. Conversely if the apparent resistivity decreases with period, the phase will be greater than $\frac{\pi}{4}$.

Figure 2.4 illustrates a synthetic example of consistent apparent resistivity and phase curves. The model contains 2 layers: the upper layer is 5 km thick and 100 Ωm resistivity while

the lower layer is a halfspace with $10 \Omega\text{m}$ resistivity. The apparent resistivity and phase curves were calculated for frequencies in the range $1000 - 0.001 \text{ Hz}$. At a high frequency (10 Hz) the signal only samples the upper $100 \Omega\text{m}$ layer since the skin depth is 1.5 km . In this case the apparent resistivity equals the true resistivity of the upper layer, and the phase angle is 45° . At intermediate frequencies (about 1 Hz) the signal starts to sample the low resistivity halfspace. There is a slight rise in apparent resistivity and a corresponding drop in phase angle as the signal first detects this interface. This occurs when the attenuation rate of the electric field suddenly changes at sharp resistivity interfaces in synthetic models. However, the resistivity structure of the earth is too complicated to observe this effect in real data. At the lowest frequencies ($< 1 \text{ Hz}$) the signal is sampling both layers, so the apparent resistivity begins to decrease and approach the resistivity of the lower layer, while the phase angle increases above 45° . As the frequency decreases further the skin depth becomes large enough for the top resistive layer to become negligible compared to the volume of the low resistivity halfspace. Thus at frequencies lower than 0.01 Hz the apparent resistivity asymptotically approaches the true resistivity ($10 \Omega\text{m}$) of the conductive halfspace.

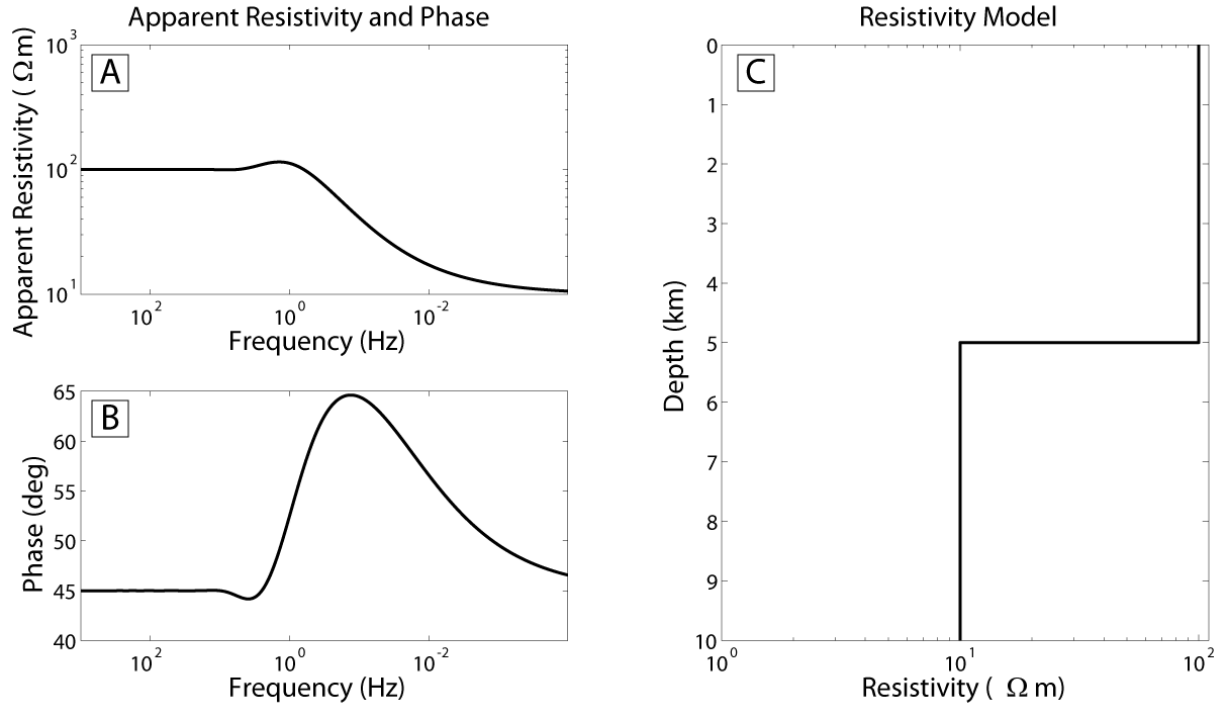


Figure 2.4: Two layer resistivity model with a 100 Ωm layer from 0 – 5 km depth and 10 Ωm halfspace below. Panel C shows the model resistivity with depth. Panel A shows the apparent resistivity as a function of frequency, and panel B contains the phase angle as a function of frequency. At the highest frequencies the signal is only sampling the upper layer, so apparent resistivity equals the layer resistivity and phase is consistent at 45°. At frequencies lower than 1 Hz the lower conductive layer is detected in the apparent resistivity curve and phase is greater than 45°. When the signal begins to detect the lower layer there is a resonance effect seen as a slight rise in apparent resistivity and a slight decrease in phase angle (details in Section 2.4).

To summarize, the electric and magnetic field data collected in the field are transformed to the frequency domain and expressed as a frequency-dependent impedance tensor. This can be used to compute the apparent resistivity, which gives the average resistivity of a hemisphere below the MT station with radius equal to the skin depth. The impedance phase is closely related to apparent resistivity, and indicates the phase angle between orthogonal, horizontal electric and magnetic fields. In high quality MT data, variations in the phase should consistently follow changes in apparent resistivity for all frequencies. This is a method for checking the quality of MT data during processing.

2.5 Dimensionality

In a 1-D Earth where resistivity only varies with depth, the impedance tensor from Eq. 2.13 will contain zeros as the diagonal elements and the off-diagonal elements will be equal and have opposite signs:

$$\mathbf{Z}(\omega) = \begin{bmatrix} 0 & Z(\omega) \\ -Z(\omega) & 0 \end{bmatrix} \quad (2.17)$$

This is because the electric and magnetic fields in the xy plane will not change with measurement angle if the Earth has a layered resistivity structure. However for a 2-D Earth the resistivity will only vary in the y-direction and depth. In this case, the diagonal elements will generally be non-zero. In the 2-D case, geoelectric strike is defined as the direction that minimizes the values of the diagonal impedance components. Only when the coordinate system is rotated to the strike direction (the x-direction by convention) will the diagonal terms be zero. The off diagonal terms Z_{xy} and Z_{yx} will generally be nonzero and not equal:

$$\mathbf{Z}(\omega) = \begin{bmatrix} 0 & Z_{xy}(\omega) \\ Z_{yx}(\omega) & 0 \end{bmatrix} \quad (2.18)$$

With a 2-D resistivity structure, two EM field polarizations can be defined:

Transverse electric (TE) mode: The electric field is polarized along strike and the magnetic field will have H_y and H_z components (Figure 2.5). Since electric current flows parallel to strike, a vertical magnetic field H_z is also generated in the TE mode.

Transverse magnetic (TM) mode: The magnetic field is polarized along strike and electric current flows across resistivity contrasts. In this case the impedance is calculated with E_y and H_x components.

In the 3-D case no simplifying assumptions are made, and the impedance tensor generally contains all non-zero components. This is because the geometry of the Earth is more complicated

and the strike direction is not defined. The TE and TM modes are not defined because Maxwell's equations cannot be decoupled into the two independent polarizations.

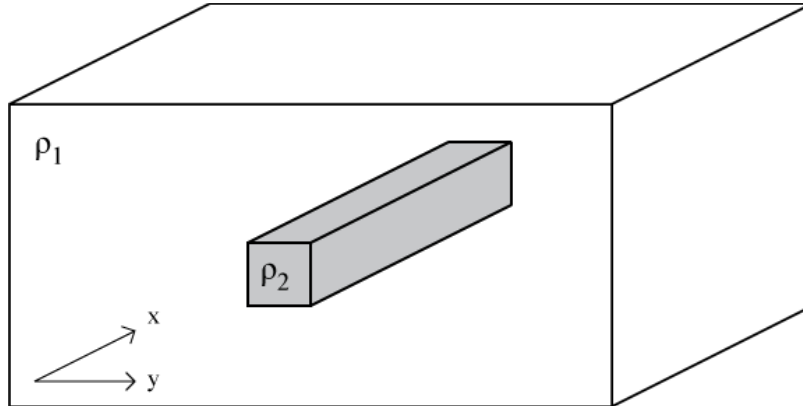


Figure 2.5: Schematic diagram of a 2-D Earth with $\rho_1 > \rho_2$. Assume the conductive prism extends infinitely in the x-direction. Geoelectric strike is aligned with the x-direction. In the TE mode electric current flows parallel to strike and in the TM mode current flows perpendicular to strike, crossing resistivity boundaries.

2.6 Distortion

The resistivity structure of the near surface is often very complicated, with small scale structures caused by local conductive overburden (e.g. clays and sands) or topographic features (Sternberg et al., 1988). As the electric currents induced in the Earth pass through these structures they are strongly distorted with the direction and magnitude of the electric fields changed significantly. This occurs when electric charge builds up on the boundaries of a small, near-surface body. The distortion is frequency-independent because the scale of the near-surface body is small compared to the signal frequency and no attenuation occurs. Galvanic distortion can make a 1-D or 2-D impedance tensor appear 3-D and complicates data analysis. Static shifts are a type of galvanic distortion that change the amplitude of the measured electric field, and result in an apparent resistivity that is shifted by a real amount at all frequencies (Jones, 1988).

Resistivity information from other MT stations may be used to correct the level of static shift. The time domain electromagnetic (TEM) sounding technique can also be used to correct static shifted MT data since it does not record electric fields (Sternberg et al., 1988; Pellerin, 1990). However, this approach works best for simple geometries (relatively 1-D) and two surveys are required to compare the level of the apparent resistivity curves.

2.7 Vertical magnetic field transfer functions and the tipper

Non-zero vertical magnetic fields at the Earth's surface can indicate the presence of a 2-D or 3-D resistivity distribution. However, Jones and Spratt (2002) showed that in some cases the source field is not a plane wave, resulting in a non-zero vertical magnetic field even in a 1-D layered Earth. These source field effects become significant at high geographic latitudes nearer to strong electric currents in the auroral electrojet (Lezaeta et al., 2007).

The tipper (\mathbf{T}) is a transfer function that relates the measured vertical magnetic field to the horizontal magnetic fields, and is defined as:

$$H_z(\omega) = [T_{zx}(\omega) \quad T_{zy}(\omega)] \begin{bmatrix} H_x(\omega) \\ H_y(\omega) \end{bmatrix} \quad (2.19)$$

where T_{zx} and T_{zy} are the tipper components derived from each polarization of the horizontal magnetic field. The tipper components are complex functions of frequency, with each containing a real and imaginary component. Induction arrows are a graphical representation of the real tipper at an observation point, and are plotted with x and y components:

$$I_x = \frac{H_z}{H_x} \quad (2.20)$$

$$I_y = \frac{H_z}{H_y} \quad (2.21)$$

Chapter 2: Physics of the MT and ZTEM Methods

Induction arrows point toward conductors when plotted in the Parkinson convention, and point away from them when plotted in the Wiese convention (Parkinson, 1959; Wiese 1962). The magnitude of the induction arrow is related to the strength of the electric current flow in conductors that produces the vertical magnetic field. Note that the tipper will be zero directly over a conductive body, as the vertical magnetic field component changes sign at this location (Figure 2.6). This means that tipper measurements at an MT station are actually sensitive to lateral resistivity variations that are not necessarily directly below. For instance, induction arrows at low frequency will point toward the ocean in Parkinson convention if the MT station is near a coastline (Bertrand et al., 2009). Vertical magnetic field data in the form of induction arrows can supplement dimensionality analysis by determining the direction of regional geoelectric strike (Unsworth et al., 2004).

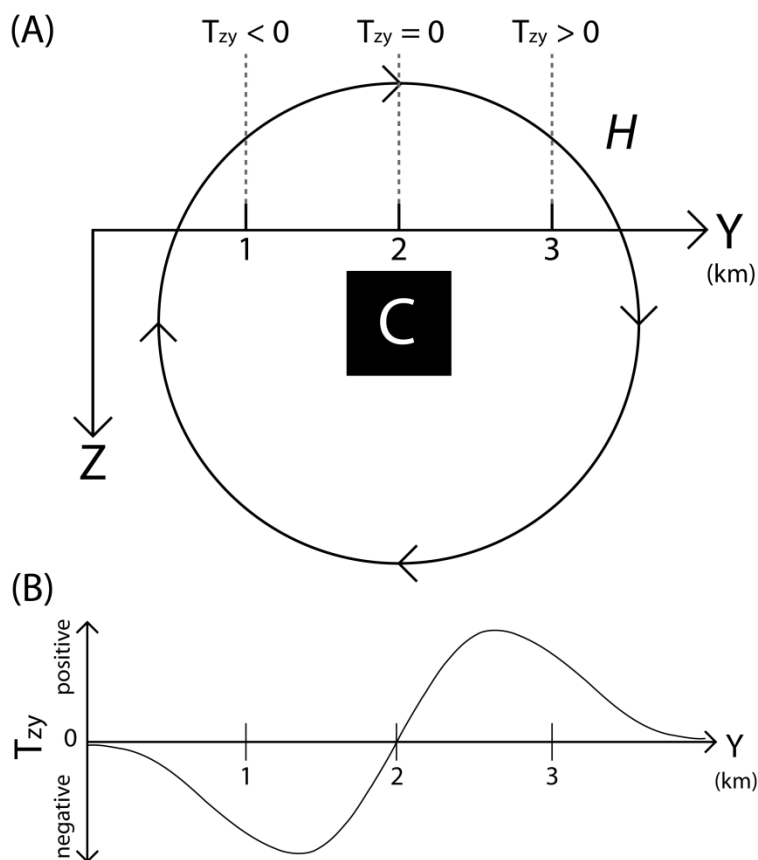


Figure 2.6: In panel A, electric current flowing along the buried 2-D conductive body C (extending infinitely into the page) induces a magnetic field, H . The tipper is the ratio of the vertical to horizontal magnetic field components, and changes sign depending on the observation point. At $y = 1$ km, the magnetic field is oriented in the negative z and positive y directions, so the ratio is negative and the Z/Y tipper component T_{zy} is negative. At $y = 3$ km the magnetic field is oriented in the positive z and positive y directions, so the ratio is positive and T_{zy} is positive. Directly over C at $y = 2$ km, the magnetic field is completely oriented in the y direction, so H_z and T_{zy} are both zero. Panel B shows how the T_{zy} response at the surface varies for different locations over C. Note that T_{zy} changes sign directly over C, and approaches zero far from C as H decreases in magnitude.

2.8 MT and ZTEM Responses of a Synthetic Porphyry Model

A synthetic modelling test was performed to illustrate the resolution of the MT and ZTEM method. The goal was to determine the ability of the methods to determine resistivity boundaries and how closely they recovered the original resistivity structure. The synthetic test

was carried out using the University of British Columbia e3dmtinv octree inversion code (details in Chapter 5). Since spatial smoothing is imposed as a constraint in inversion algorithms, a synthetic test investigates how sharply resistivity boundaries will be defined in the resistivity model. The synthetic model was designed to resemble the resistivity contrasts expected in a surface-exposed porphyry deposit. It consists of a 1 x 1 km wide resistive core (1000 Ωm) representing the intrusive porphyry stock, surrounded by a 2 x 2 km wide conductive ring (10 Ωm) representing a sulfide-rich mineralization zone, both extending to a depth of 2 km. Both features are enclosed in a 100 Ωm halfspace (Figure 2.7). In the following sections, the calculated data represent what would be observed by a ZTEM and MT survey if the subsurface was represented by the synthetic porphyry model. The resolution of each method will be evaluated by comparing the recovered inversion models to the known synthetic porphyry resistivity model.

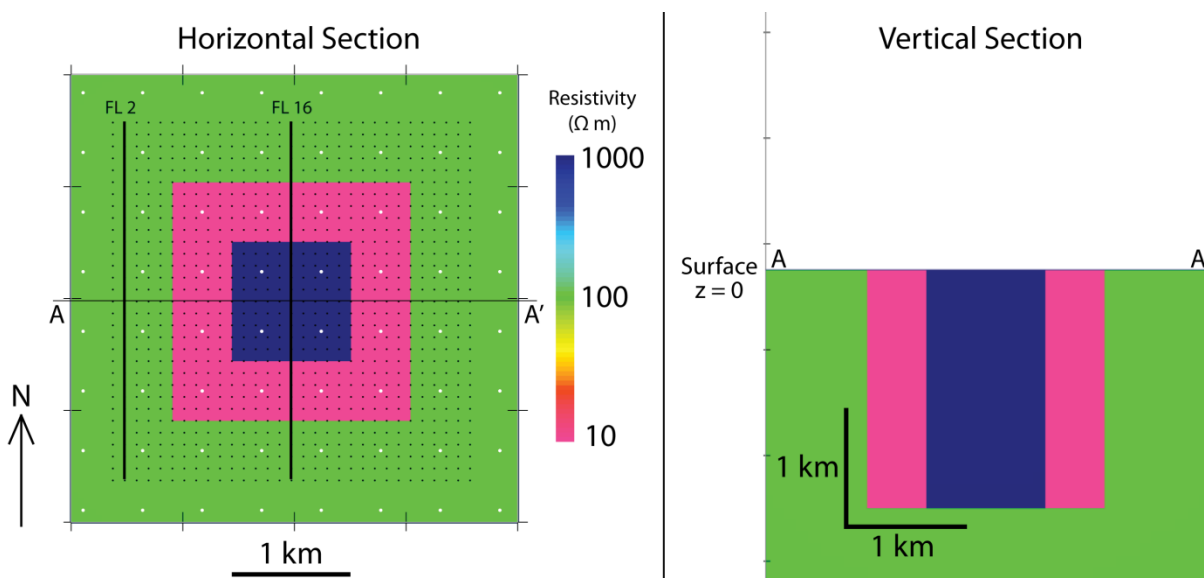


Figure 2.7: Plan view (left) and vertical section (right) of the synthetic porphyry model. The core is a 1 x 1 km wide, 1000 Ωm resistor, surrounded by a 2 x 2 km wide 10 Ωm conductor. These two features extend to 2 km depth and are embedded in a 100 Ωm halfspace. In plan view the black dots represent ZTEM observation points, black lines are the north-south oriented ZTEM flight lines (FL2 and FL 16) shown in Figure 2.10, and sparse white dots are MT station locations. The vertical section is along profile A-A'.

2.8.1 Forward Modeling

To simulate a ZTEM survey, data were calculated at 962 locations above the synthetic porphyry model. The measurement locations are shown as black dots in Figure 2.7. The four tipper components were computed at frequencies of 360, 180, 90, 45, and 30 Hz as in an actual ZTEM survey. Figure 2.8 shows a map view of the synthetic data at a frequency of 90 Hz. Here the x-direction is north and the y-direction is east. Two crossover anomalies can be seen in the real T_{zx} component at $x = 1250$ m and $x = 2750$ m as the vertical magnetic field is zero directly over the conductive ring. The crossover is only seen over the northern and southern parts of the conductive ring since the induced horizontal magnetic field will only be in the x-direction here. The resistive core ($x = 2000$ m) has no tipper response in either real component because the vertical magnetic fields induced by opposite sides of the conductive ring negate each other. In contrast, the induced horizontal magnetic field will be in the y-direction over the western and eastern parts of the conductive ring. This is apparent in the real T_{zy} data, where there are crossovers at $y = 1250$ m and $y = 2750$ m. The imaginary components have small magnitudes but still contain information about the resistivity structure. The data are not perfectly smooth because 5% Gaussian noise was applied to the synthetic data prior to inversion.

The synthetic ZTEM data at a frequency of 90 Hz are displayed as induction arrows in Figure 2.9. When plotted in the Parkinson convention, the induction arrows point toward the low resistivity ring. The ZTEM data are also shown along flight lines to illustrate tipper crossovers along a profile (Figure 2.10). The tipper data at 90 Hz are shown for flight lines 2 and 16 (black lines in Figure 2.7). Flight line 2 is not directly over the conductive ring so there is very little response in the T_{zx} components. However at 90 Hz the signal is sampling the magnetic field induced from current flow along the conductive ring, which appears as a negative response in the

T_{zy} components. There is a much more pronounced response in the real T_{zx} component for flight line 16. At the north and south ends of the flight line there are crossovers when passing above the conductive ring. The zero crossover at the middle of flight line 16 occurs directly over the resistive core, where the induced magnetic fields from opposite sides of the conductive ring cancel each other out. There is no T_{zy} response for flight line 16 because most of the induced magnetic fields are in the x-direction. Even when flying over the resistive core there is a net zero response in T_{zy} when the induced magnetic fields from the east and west sides of the conductive ring are equal and opposite each other.

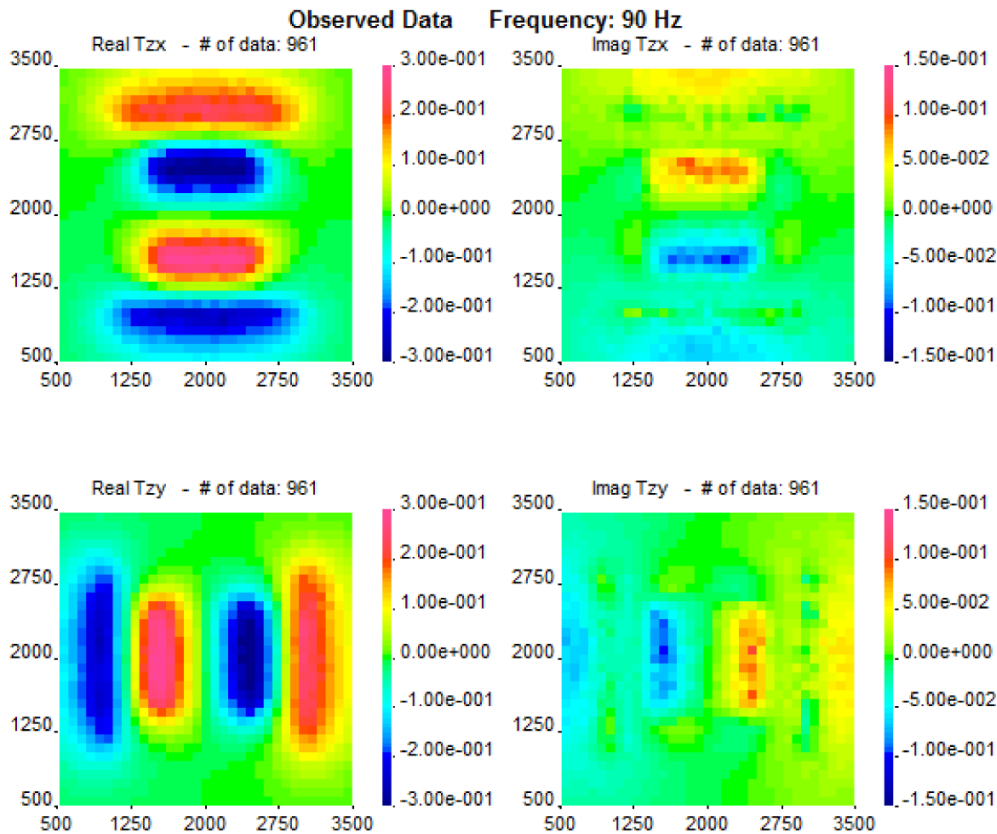


Figure 2.8: Forward modelled tipper data at 90 Hz for the synthetic porphyry model shown in Figure 2.7. Data were computed for the four tipper components at frequencies of 360, 180, 90, 45, and 30 Hz. Two crossover anomalies can be seen in both the real T_{zx} and T_{zy} components as the vertical magnetic field changes direction when crossing over the low resistivity ring. The x-direction is oriented to geographic north, and the y-direction is oriented to geographic east.

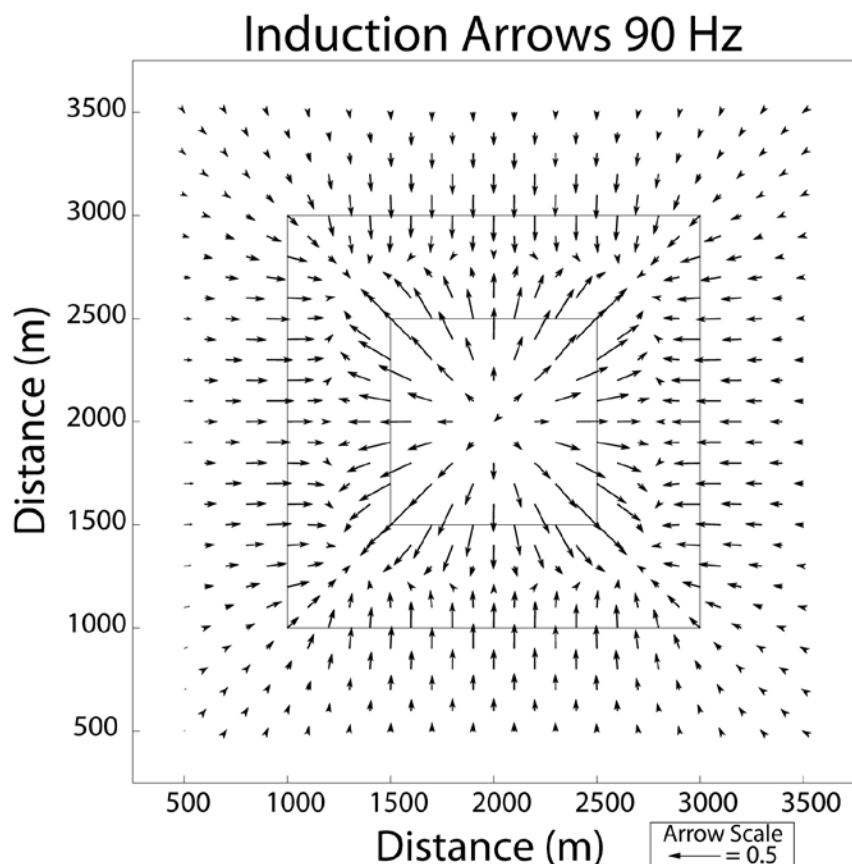


Figure 2.9: Map view of real induction arrows of synthetic ZTEM data calculated over the synthetic porphyry model (Figure 2.7). The outlines of the porphyry model are shown in black. The arrow length corresponds to the magnitude of the induction arrows, and therefore the strength of the inductive response. Arrows are plotted in the Parkinson convention, and point toward the conductive $10 \Omega\text{m}$ ring.

MT impedance data were also calculated at ten frequencies between 300 – 0.5 Hz for 64 stations above the synthetic porphyry model (Figure 2.7). Figure 2.11 shows the 10 Hz synthetic data in map view. The Z_{xy} and Z_{yx} data define the boundaries of the synthetic porphyry well since in most cases the current will flow parallel or perpendicular to resistivity interfaces. The diagonal components Z_{xx} and Z_{yy} are close to zero for most of the model except the corners, where 3-D effects are largest. 5% Gaussian noise was applied to the data before running the inversion.

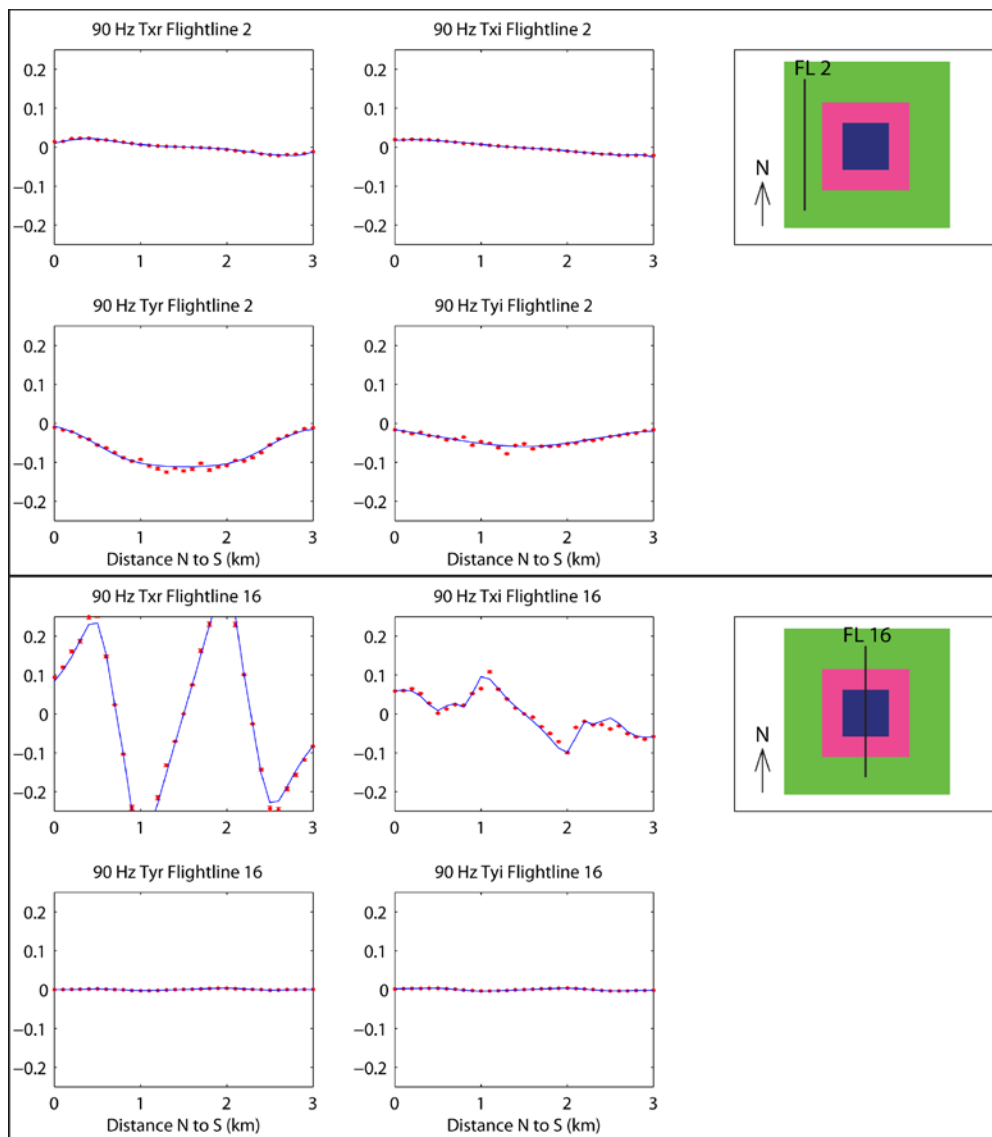


Figure 2.10: Tipper data for flight lines 2 (top) and 16 (bottom) over the synthetic porphyry model. The positive x-direction is oriented north, and the positive y-direction is oriented east. Flight lines start from the north (0 km) and end in the south (3 km). Red dots are the observed data and blue lines are the inversion model response. Flight line 2 is over the halfspace so there is very little response in the real T_{zx} component. The real T_{zy} component is negative toward the middle of the line due to the magnetic field induced by the conductive ring 500 m to the east. Flight line 16 contains 2 zero-crossovers in the real T_{zx} component when crossing over the conductive ring. The first occurs when crossing from the resistive halfspace to the conductive ring to the highly resistive core, and the second occurs when crossing in the opposite order. The central zero-crossover occurs when passing directly over the resistive core, where vertical magnetic fields induced by opposite sides of the conductive ring cancel each other out. There is no T_{zy} response because there are no induced fields in the y-direction for most of the flight line and the induced fields negate each other directly over the resistive core.

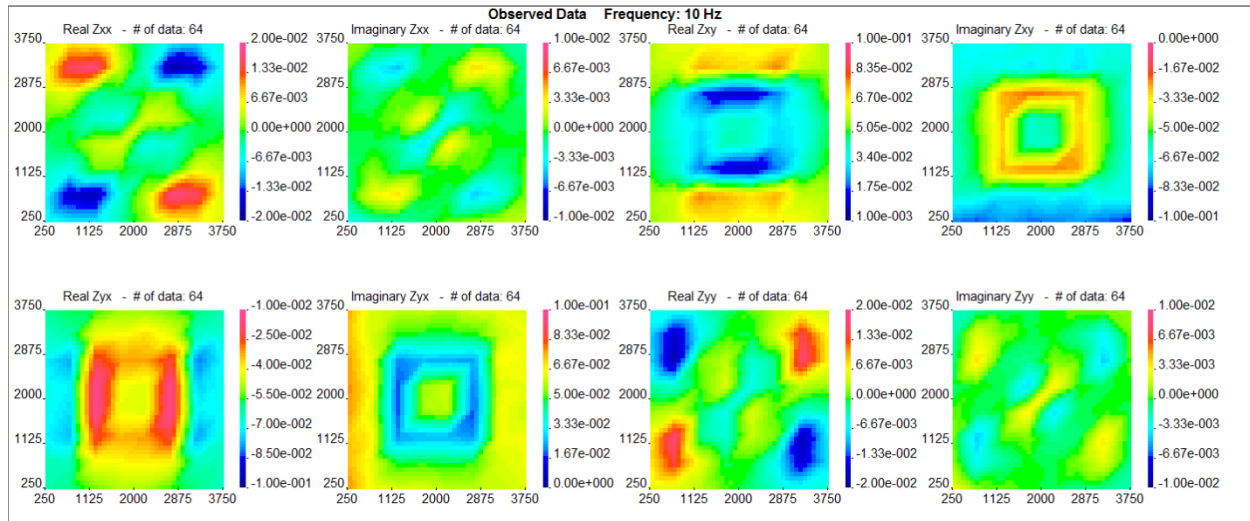


Figure 2.11: Real and imaginary components of the forward modelled MT impedance data for the synthetic porphyry model (Figure 2.7). The off-diagonal impedance components Z_{xy} and Z_{yx} define the resistivity boundaries well, while the diagonal components Z_{xx} and Z_{yy} are more sensitive to the corners where 3-D effects on the electric field direction are largest. The x-direction is oriented to geographic north, and the y-direction is oriented to geographic east.

2.8.2 Synthetic ZTEM Inversion

To test the resolution of the inversion code, the ZTEM synthetic data were inverted with a 100 Ωm halfspace starting model. 5% Gaussian noise was added to the data to more closely resemble the noise present in actual field data. The goal was to recover the resistivity structure of the original synthetic porphyry as closely as possible. The background resistivity was known in this synthetic example, but this is not usually the case in an actual field survey. The inversion results are shown in Figure 2.12. The inversion reached the desired sum of squares misfit of 1 and the model closely resembles the original synthetic model, especially close to the surface. In Figure 2.12 the black lines represent the boundaries in the synthetic resistivity model. The inversion is able to recover the resistivity structure well near the surface, but most of the signal appears to attenuate by about 800 m depth even though the synthetic resistivity model extends to 2 km depth. Using the skin depth equation (Eq. 2.12), it is clear that the signal frequency is not

low enough to resolve the deepest parts of the synthetic porphyry. For instance, in a $100 \Omega\text{m}$ earth, the lowest ZTEM frequency of 30 Hz has a penetration of about 900 m. The penetration is even less in a $10 \Omega\text{m}$ environment such as the synthetic conductive ring, where the skin depth is approximately 300 m. However, this penetration depth is still impressive for an airborne technique, and the resistivity values at the surface and 250 m depth are very close to the actual values from the original synthetic model. This is probably because the initial resistivity model in the inversion matched the true resistivity of the synthetic model.

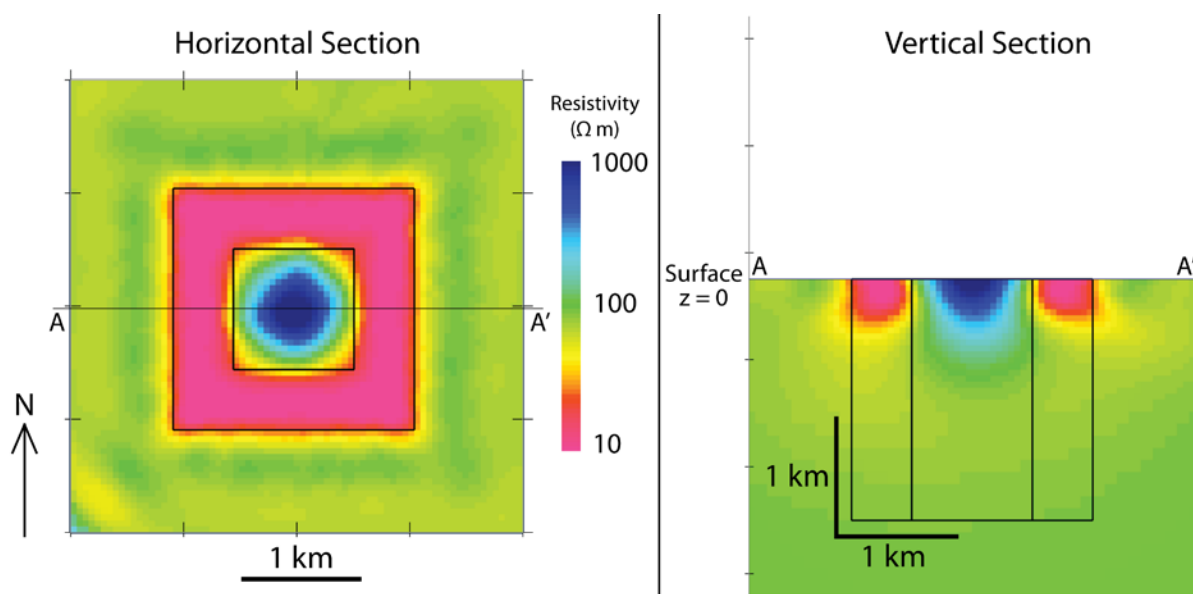


Figure 2.12: ZTEM synthetic inversion of the porphyry model at the surface (left) and vertical section through A-A' (right). The forward modeled data at five frequencies (360 – 30 Hz) were inverted with a starting $100 \Omega\text{m}$ halfspace. Black lines show the boundaries of features in the original synthetic model (Figure 2.7). The resistivity boundaries and values are well recovered at the surface, but the signal has mostly attenuated by 800 m depth in this moderately conductive model. The lateral boundaries are defined well compared to the synthetic resistivity model, but the recovered model features do not extend to the true 2 km depth.

2.8.3 Synthetic MT Inversion

The synthetic MT data were also inverted with the same 100 Ωm starting resistivity model after applying 5% Gaussian noise to the data. Compared to the synthetic ZTEM inversion there are much fewer stations but the lowest frequency of 0.5 Hz allows for deeper penetration. The inversion result is shown in Figure 2.13. The synthetic porphyry boundaries are well recovered near the surface even with the sparser station layout. The MT model contains features up to 2 km deep due to the lower frequency range. This can be attributed to the lower frequency MT data, with the 0.5 Hz data able to penetrate 2 km even in a 10 Ωm earth (from Eq. 2.12). While the conductive ring is imaged about 200 m deeper than in the ZTEM model, there is a conductor smeared across the lower portion of the porphyry. This deeper conductor is not present in the synthetic resistivity model and is clearly an artifact of the non-unique inversion. This feature may be better constrained with more stations directly over the porphyry center or by manually adjusting the inversion's spatial smoothing in the vertical direction.

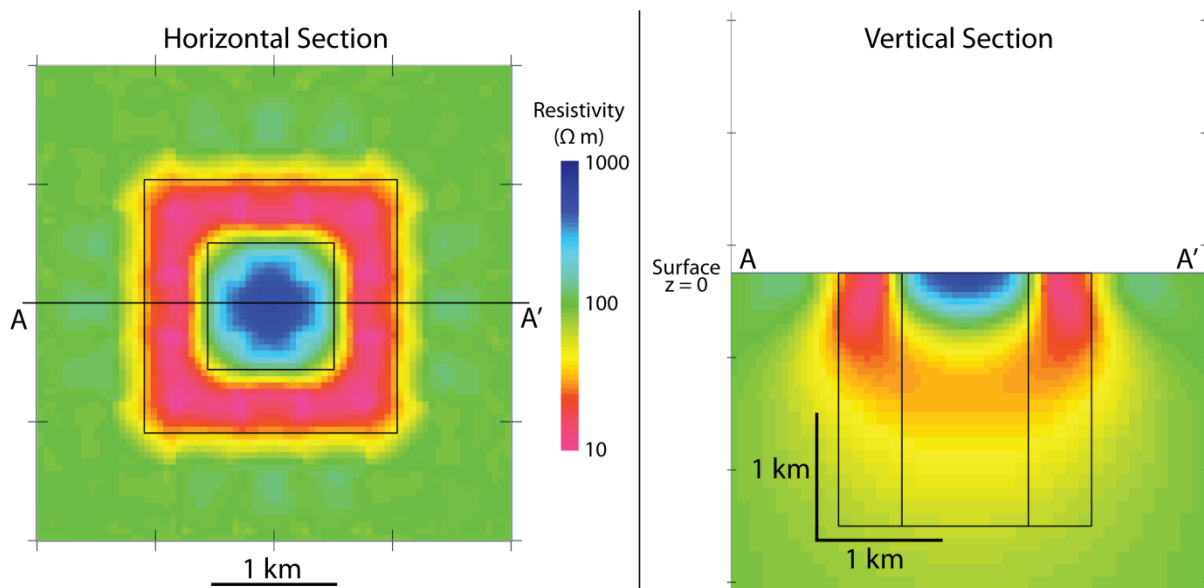


Figure 2.13: MT synthetic inversion of the porphyry model at the surface (left) and vertical section through A-A' (right). The forward modeled data at ten frequencies (300 – 0.5 Hz) were inverted on a starting 100 Ωm halfspace. Black lines show the boundaries of features in the original synthetic model (Figure 2.7). The resistivity boundaries are well recovered and there is clearly more depth resolution than the ZTEM inversion.

2.9 Summary

This chapter introduced the theory behind the naturally-occurring EM signals measured by the ZTEM and MT methods and how the impedance and tipper data are calculated. Synthetic examples of ZTEM and MT inversions show that each technique is able to image resistivity contrasts associated with an idealized porphyry deposit. Lateral resistivity contrasts are recovered well in the inversions, and it is clear that the depth resolution is controlled by the frequency-dependent EM skin depth. Chapter 3 will introduce the basics of porphyry deposit formation and expected geophysical responses of a typical porphyry deposit.

Chapter 3: Geological and Geophysical Aspects of Porphyry Exploration

3.1 Introduction

Porphyry copper deposits currently provide about 75% of the world's copper and a large fraction of the world's molybdenum and gold (Sillitoe, 2010). They are large deposits (10-1000 Mt) with typical copper grades between 0.3% and 1.0%. As seen in Figure 3.1, these deposits are mostly formed beneath the active volcanoes of magmatic arcs at subduction zones (Richards, 2009; Sillitoe, 2010). As magma rises and cools beneath a volcano, metallic sulfides are exsolved and concentrated from circulating fluids. When the volcanoes have ceased being active they are eroded and the mineral deposits are exposed at or close to the surface. Since porphyry formation cannot be observed in real time, and subsequent tectonic activity can modify them, their exact structure is not fully understood.

Historically, a combination of geophysical methods, geochemistry, and drilling has been used in porphyry exploration. This combination of geologic mapping, geochemistry, and drilling is effective at developing shallow deposits that outcrop. However, as most shallow and exposed porphyry deposits have been discovered, the need for deeper exploration techniques has increased (Holliday and Cooke, 2007). When deposits are hidden under cover or not completely exposed, geophysical methods such as magnetics, induced polarization (IP), and in particular electromagnetic (EM) induction techniques are used to map the geological structure and distribution of alteration zones in porphyry deposits at depths of 100 m or more. These

techniques are sensitive to a range of rock properties, some directly related to the distribution of economically significant minerals such as:

(1) electrical resistivity

(2) chargeability

(3) magnetic susceptibility.

(1) Electrical resistivity gives information about the distribution of sulfide minerals and the extent of alteration zones. Airborne time domain electromagnetic (ATEM) methods are used to map alteration halos in porphyry deposits at depths of several hundred meters, but the maximum penetration depth is limited by signal strength. Geotech Ltd.'s natural-source ZTEM system has the ability to detect structure at up to 2 km depth in moderately resistive rock. Compared to ATEM methods, ZTEM has been shown to be more sensitive to resistivity contrasts (Kaminski et al., 2010; Kaminski and Oldenburg, 2012) and to have a greater penetration depth (Paré and Legault, 2010). However, it is not clear if airborne EM techniques are able to detect subtle resistivity contrasts from porphyry deposit alteration zones (Smith, 2014) since these techniques are also sensitive to other nearby conductive bodies (Smith et al., 2010).

(2) Induced Polarization (IP) surveys measure chargeability and can directly detect sulfide minerals such as pyrite (Oldenburg et al., 1997; Paré and Legault, 2010) and help identify areas of economic mineralization. Disseminated sulfide mineralization is usually associated with high chargeability anomalies, making this technique valuable for porphyry deposit exploration (Abbassi, 2013).

(3) The magnetic properties of porphyry deposits are well-documented (Gunn and Dentith, 1997; Clark, 2014) and generally include a magnetite-rich intrusive core surrounded by a magnetite-depleted phyllic or propylitic alteration zone. However, these alteration zones may not directly

Chapter 3: Geological and Geophysical Aspects of Porphyry Exploration

correlate with the distribution of economically significant minerals. The magnetic survey helps define the spatial distribution of alteration zones and by inference the distribution of mineralization.

The ability of ZTEM to resolve resistivity contrasts associated with porphyry deposits will be evaluated in Chapters 5 and 7 using data from the Morrison deposit. First it is crucial to understand the known alteration and mineralization structure of typical porphyry copper deposits as well as their respective geophysical signatures.

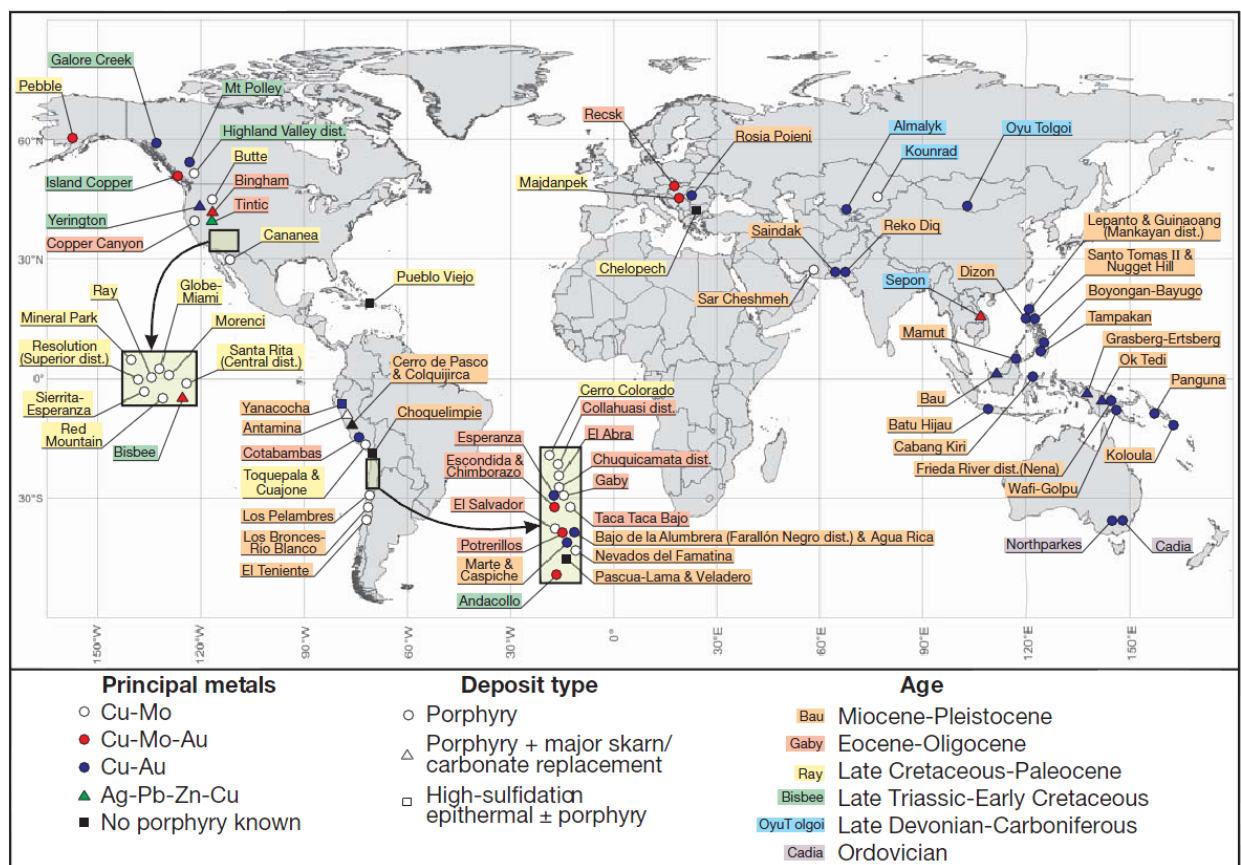


Figure 3.1: Worldwide distribution of major porphyry copper deposits. Note the concentration along subduction zones at ancient and modern convergent plate margins. Reproduced with permission from Sillitoe, (2010).

3.2 Porphyry Copper Deposit Alteration and Mineralization

Porphyry copper deposits form above intrusive stocks or dikes that originate from an underlying pluton. As a magma body cools, metal rich aqueous fluids are exsolved and move upwards. As these fluids move upwards, they cool, causing hydrothermal alteration of the host rock and the deposition of minerals (Figure 3.2). In general the alteration zones found in a porphyry deposit, their common alteration minerals, and temperatures of formation are:

- Propylitic – chlorite, carbonate, epidote, ~ 200 - 400°C
- Argillic – Quartz, kaolinite, < 300°C
- Phyllic – Quartz, sericite, ~ 300 - 500°C
- Potassic – K-feldspar, biotite, ~ 400 - 500°C

Temperature estimates are from the United States Geological Survey Scientific Investigations Report 2010 (John et al., 2010) and it should be noted that magma composition has an effect on hydrothermal alteration type as well.

In the early stage of porphyry deposit formation, the initial stock cools from temperatures in excess of 500° C, and a two-phase fluid of hypersaline liquid and vapor (Sillitoe, 2010) travels upward through the host rock. Between about 400 – 500°C these fluids generate potassic alteration as well as initial copper mineralization. Advanced argillic alteration begins as a cooler, single-phase acidic fluid migrates upward. Convecting groundwater at the margins of the potassic stock is heated and produces a broad propylitic alteration zone. As the intrusive body solidifies and the upper portion cools, fluids that cool to about 300°C begin the process of phyllic alteration, above and overprinting the potassic alteration zone. This fluid, combined with meteoric water, continues to rise into the argillic lithocap and may form a high-sulfidation epithermal deposit.

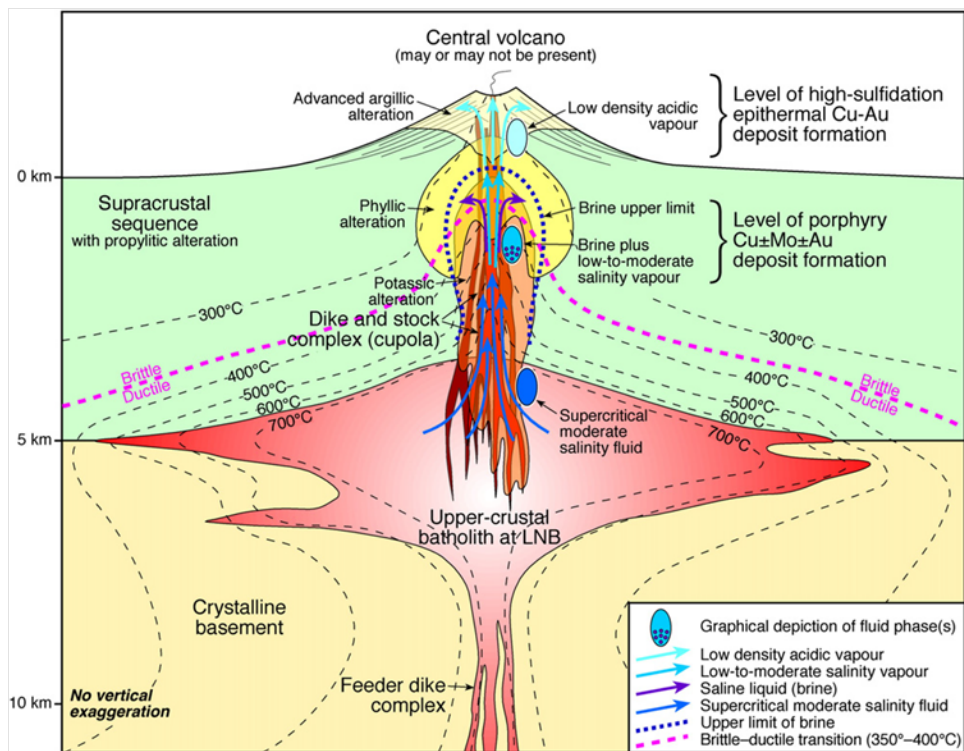


Figure 3.2: Fluid pathway and resulting alteration pattern of a typical porphyry deposit. High temperature, multi-phase fluid ascends from the magma body emplaced at the level of neutral buoyancy (LNB), and produces potassic alteration at the base of the deposit. As the fluids rise and decrease in temperature the deposit grades outward into phyllic, then propylitic alteration zones. Advanced argillic alteration forms from shallow, low temperature acidic fluids. Reproduced with permission from Richards, (2011).

The potassic alteration zone is usually located in the central and deepest part of the porphyry deposit, and is associated with biotite and K-feldspar (Figure 3.2). Economic concentrations of sulfide minerals, including chalcopyrite and bornite, are usually found in the potassic zone (Sillitoe, 2010). As shown in Figure 3.2, the potassic zone grades outward into the propylitic zone, which extends to the edge of the deposit. The propylitic zone does not usually contain sulfide minerals in economic concentrations, and is identified by the presence of chlorite and epidote. Phyllic alteration develops above the potassic zone and usually results in overprinting and destruction of potassic assemblages. As a result, the phyllic zone has an abundance of pyrite but may have lower concentrations of the previously existing chalcopyrite

and bornite. The advanced argillic zone forms a lithocap containing quartz-kaolinite and may overprint the uppermost area of the deposit. Depending on the degree of erosion and the lifespan of the porphyry system, the argillic zone may be over 1 km thick.

Most porphyry deposits are Mesozoic or Cenozoic in age presumably because these younger deposits are relatively well preserved compared to older deposits (Sillitoe, 2010). Erosion level is a large factor in the discovery and characterization of porphyry deposits since an eroded system may reveal a larger portion of the mineralized zone, while a relatively uneroded deposit could obscure alteration and mineralization below. An uneroded deposit may also contain a shallow high-sulfidation epithermal deposit (Figure 3.2) above the main porphyry stock. Erosion level can influence the magnitude of the geophysical response above a deposit, as seen in the following section.

3.3 Geophysical Response of Porphyry Copper Deposits

In mineral exploration the challenge is to identify the zone with economically significant concentrations of mineralization. This is complicated by the fact that many deposits deviate from the ideal porphyry model since they have formed under different spatial and temporal scales, or have been subsequently deformed by regional tectonics. The alteration zones can be distinguished by examining various geophysical responses such as electrical resistivity, magnetic susceptibility and chargeability. Figure 3.3 shows the expected geophysical response of alteration and mineralization zones at different levels of erosion. The strength of the geophysical response is largely influenced by erosion of individual alteration or mineralization zones. In panels A – C it is clear that an eroded deposit will contain a different amount of altered material and perhaps mineralization than an uneroded deposit. For example at the porphyry erosion level (black dashed line) the potassic alteration zone may be exposed at the surface as well as

Chapter 3: Geological and Geophysical Aspects of Porphyry Exploration

economic sulfides such as chalcopyrite. The geophysical response panels reflect the different geophysical responses due to the erosion level. These responses may not correlate directly with the mineralization, but provide valuable information about lithology and alteration.

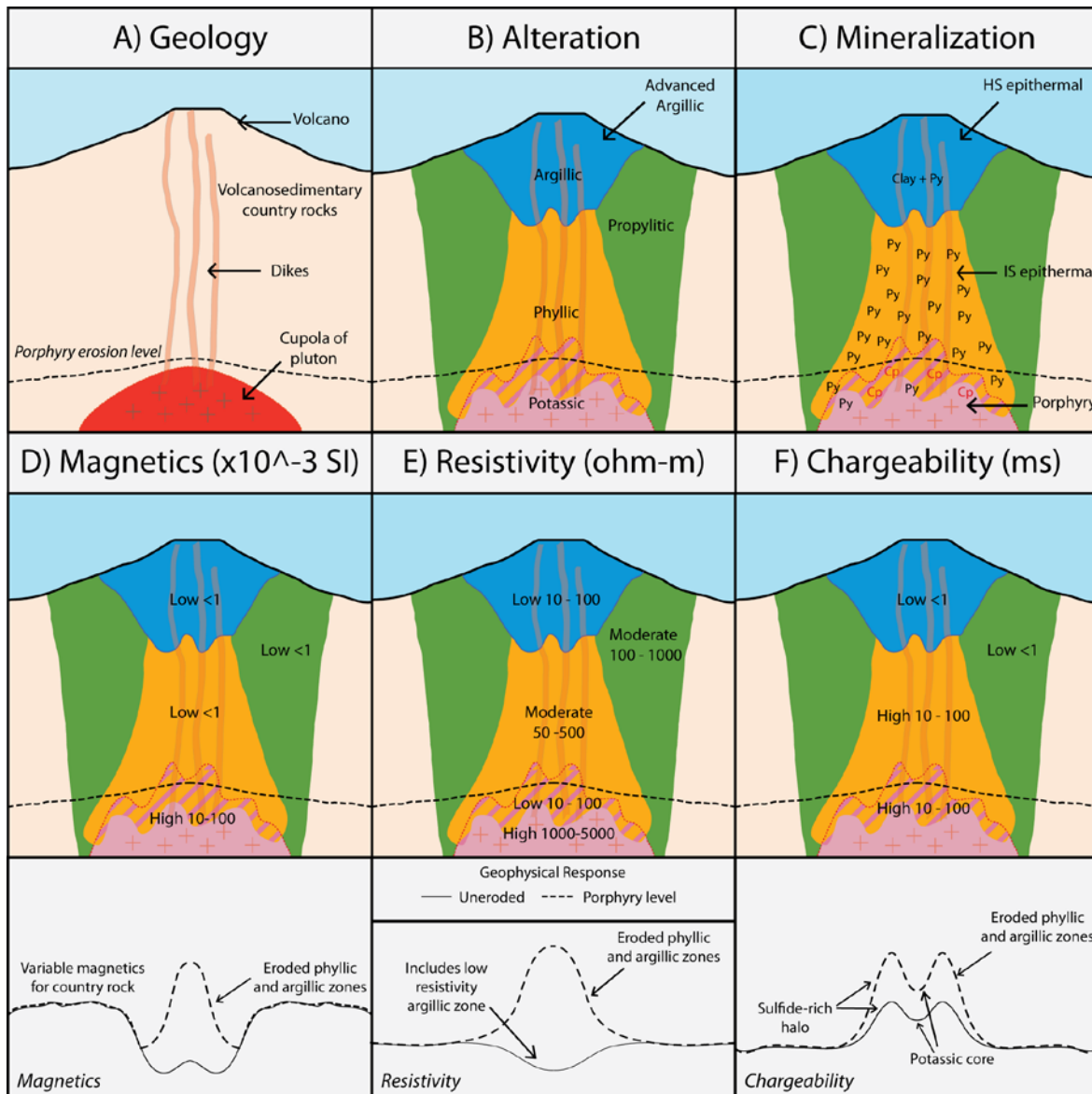


Figure 3.3: Geology, alteration, and mineralization of a generalized porphyry deposit and expected geophysical responses for an uneroded and eroded deposit. Panel A: Intrusive body with feeder dikes; Panel B: Typical porphyry system alteration pattern; Panel C: Expected sulfide mineralization, note the pyrite enrichment outside of the potassic core. Panels D-F: Geophysical responses associated with alteration zones. The lower section contains expected response for an uneroded and eroded porphyry deposit. Dashed lines indicate eroded surfaces. Py = pyrite, Cp = chalcopyrite.

Chapter 3: Geological and Geophysical Aspects of Porphyry Exploration

Magnetics has long been used for both geologic mapping and deposit detection at the regional scale (Holliday and Cooke, 2007). Since magnetite within the potassic zone undergoes destruction to pyrite in the phyllic zone, there is usually a weakly magnetic ring outside the potassic zone that corresponds with the pyrite halo. In addition, the main intrusive body should have a magnetic signature that contrasts with the surrounding host rock (Figure 3.3). For example, the regional magnetic survey at the Mt. Milligan deposit showed a magnetic high corresponding with magnetite in the potassic altered core and a nearly concentric low susceptibility zone that matched the extent of sodic-calcic and propylitic alteration (Mitchinson et al., 2013). One limitation of regional magnetic data is the lack of depth resolution. With increasing depth, the strength of the magnetic anomaly must be greater to be detected at the surface. Interpreting magnetic properties to geology may be difficult as well since lithology, regional structure, and alteration all influence magnetic susceptibility (Clark et al., 1992).

EM induction techniques can measure the electrical resistivity associated with alteration and mineralization of porphyry deposits. Figure 3.3, panel E shows the expected resistivity values at different parts of the generalized deposit. The potassic zone consists of crystalline intrusive rock, and should have a distinct resistivity signature from the host rock. For instance, a deposit hosted by sedimentary rock should have a resistive anomaly corresponding to the porphyritic stock. Intrusive rocks typically have a high resistivity because limited pore space restricts the flow of electric current. In the phyllic alteration zone the presence of sulfides also has a pronounced effect on bulk resistivity. This alteration zone is more electrically conductive than the potassic zone depending on the weight percent and interconnectivity of sulfides. Nelson and Van Voorhis (1983) collected in-situ resistivity measurements at 109 porphyry copper deposits and showed that resistivity is inversely proportional to sulfide weight percent (Figure

3.4). The mineralization is described as disseminated or in discontinuous veins for about 3% sulfide weight and below. In this case, Nelson and Van Voorhis (1983) found that the resistivity was high ($> 100 \Omega\text{m}$) and variable. At 3 – 20% weight the sulfides are vein-hosted and the resistivity decreased to below $10 \Omega\text{m}$ for samples approaching 20% sulfide weight. Although this study did not include massive sulfide samples, these would generally be above 50% weight sulfides, and have a very low resistivity ($< 10 \Omega\text{m}$).

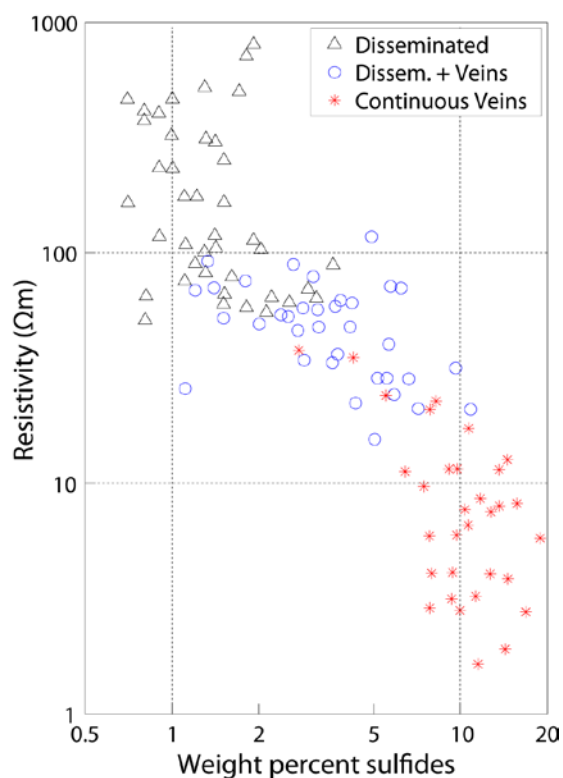


Figure 3.4: Relationship between sulfide weight percentage (x-axis) and resistivity (y-axis) based on in-situ measurements at 109 porphyry deposits. For disseminated or discontinuous veins ($< 3\%$ wt.) the resistivity tends to be high and variable. As interconnectivity increases, there is a more direct relationship between increasing sulfide weight percent and decreasing resistivity. Modified from Nelson and Van Voorhis (1983).

Induced polarization data are usually collected simultaneously with resistivity data, and has been effective in shallow porphyry deposit exploration because of its sensitivity to bodies of disseminated sulfides. The phyllic alteration zone is particularly detectable because of its high pyrite content (Figure 3.3). For example, at the Pebble porphyry deposit the presence of sulfides and especially pyrite enhancement appears as high chargeability feature (Paré and Legault, 2010).

3.4 The Morrison Deposit

Morrison is a Cu-Au-Mo porphyry deposit located in the northern Babine Lake region of British Columbia and was the focus of the geophysical data collected and analyzed in this thesis. The region is well known for previously mined porphyry copper systems at Bell (77.2 Mt, 0.48% Cu) and Granisle (52.7 Mt, 0.43% Cu) (Geotech, 2010). The Morrison deposit has a measured and indicated resource of 207 Mt at 0.39% Cu, but has not yet been developed (Simpson, 2007).

3.4.1 Tectonic Setting

Figure 3.5 shows the terrane map of the Pacific Cordillera, which is comprised of a number of accreted island and ocean arcs. The Morrison deposit is located in the Stikinia Terrane, which is a former island arc that collided with the continental margin along with several other island arc terranes in the Middle Jurassic (Monger and Price, 2002; Nelson and Colpron, 2007). After accretion, the Stikinia terrane experienced deposition of volcanic and sedimentary rocks in the Babine Lake area, including the Middle-Late Jurassic Bowser Lake Group. Porphyry deposit formation was associated with Late Cretaceous to early Cenozoic intrusions into these Mesozoic age volcanic and sedimentary rocks (McMillan et al., 1995). This includes the Morrison porphyry deposit associated with the Eocene Babine Lake igneous suite.

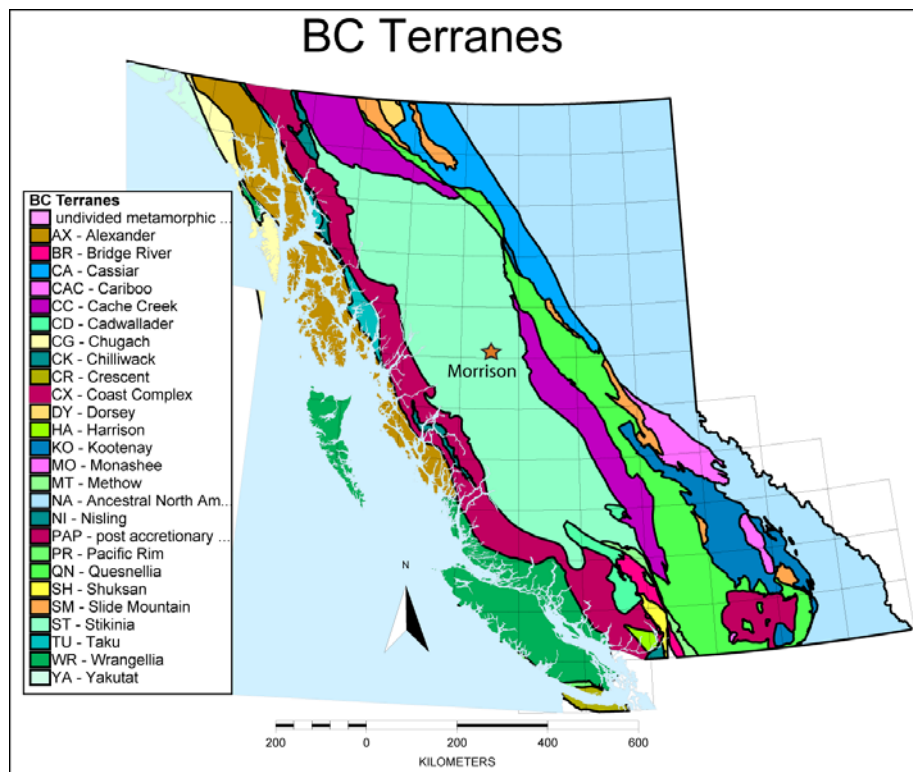


Figure 3.5: Terrane map of British Columbia showing the location of the Morrison deposit within the Stikinia Terrane. Modified from British Columbia Geological Survey, (2005).

3.4.2 Deposit Geology

As seen in Figure 3.6, the Morrison deposit is genetically and spatially related to an Eocene biotite feldspar porphyry stock (BFP), which intruded into the Middle-Late Jurassic Bowser Lake Group sediments (MLJB) about 53 Ma (MacIntyre et al. 2001). The Eocene intrusives consist of a main circular stock and a series of thin, elongate dykes. The host rock lies in the northwest trending Morrison Graben, which is downfaulted from Lower to Middle Jurassic Hazelton Group (LJHG) volcanics and sediments to the east. A prominent feature within the Morrison Graben is a pair of smaller north-northwest trending faults. The East Fault is a north trending dextral strike-slip fault that bisects the main BFP stock with an offset of about 300 m (Simpson, 2007).

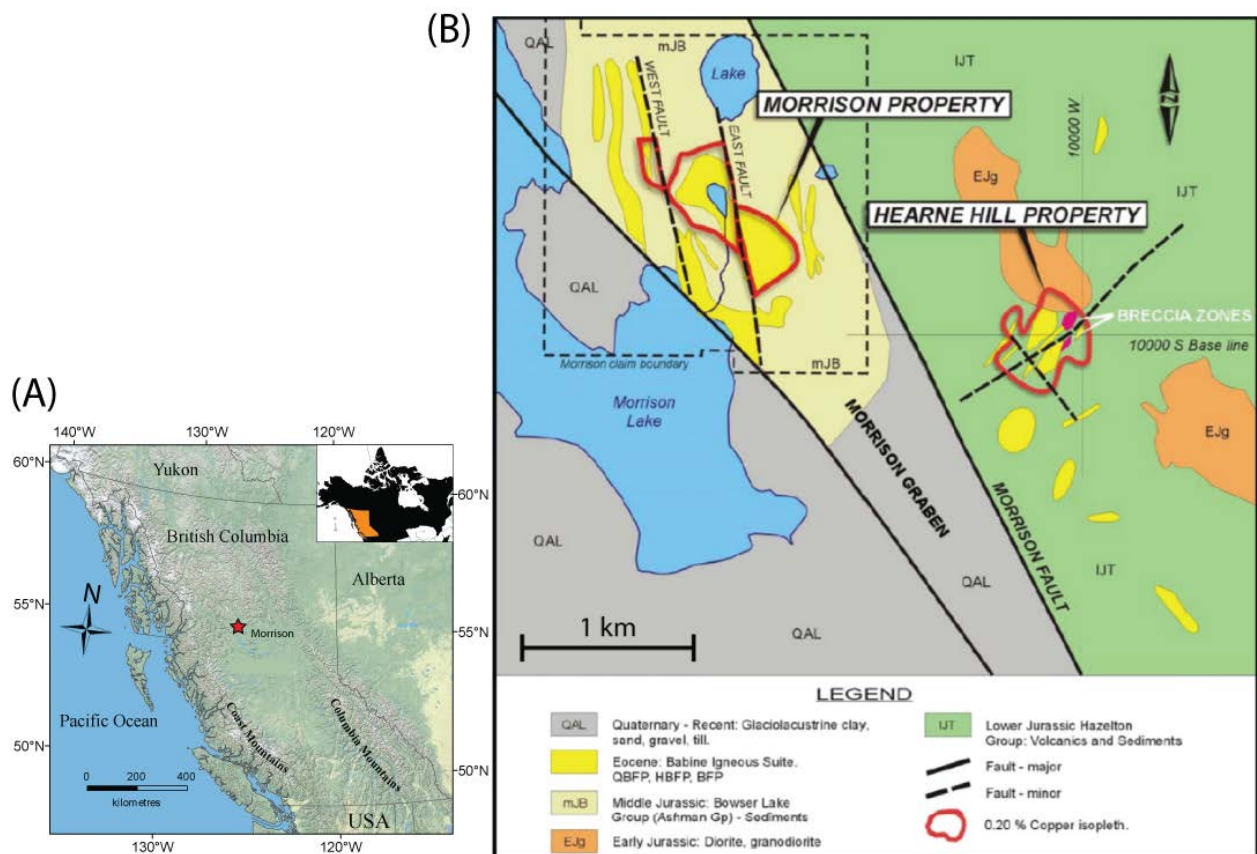


Figure 3.6: Panel A: The location of the Morrison deposit in central British Columbia, Canada. Panel B: The deposit location is outlined by the dashed black box. Copper mineralization is centered on a large (1 km) intrusive body. The deposit is contained within the Morrison Graben and features two smaller faults that cut through the major copper mineralization zone. Adapted from McClenaghan, (2013) and Robertson, (2009).

3.4.3 Hydrothermal Alteration

Potassic alteration at Morrison is mainly associated with the central BFP stock. Copper mineralization occurs as vein-hosted and disseminated chalcopyrite and bornite. Two semicircular copper zones with average grade 0.39% Cu are offset to the northwest and southeast by the East Fault. These zones are surrounded by pyrite halos related to propylitic (chlorite-carbonate) alteration. The chalcopyrite/pyrite ratio decreases outward from the concentric potassic and propylitic alteration zones. Although pyrite is usually associated with phyllic

Chapter 3: Geological and Geophysical Aspects of Porphyry Exploration

alteration, no phyllic alteration has been observed at Morrison. Argillic alteration (clay and carbonate minerals) occurs at the East Fault, and overprints other alteration types (Robertson, 2009).

3.5 Summary

Geophysical exploration provides information about deposit physical characteristics that leads to the detection of the economic mineralized zone. Porphyry deposits have a well-known alteration pattern that can be detected by various geophysical methods. Morrison is a well-studied deposit and presents an opportunity to incorporate different types of geoscientific data into the interpretation. Chapter 4 introduces the details of the ZTEM and MT surveys collected at the Morrison deposit that will be used separately and in a combined inversion to create 3-D electrical resistivity models.

Chapter 4: Morrison ZTEM and MT Data Analysis

4.1 Introduction

This chapter describes the collection and analysis of the ZTEM and MT data from the Morrison deposit. Before performing an inversion it is important to review the data to ensure quality and consistency. The ZTEM tipper data and MT apparent resistivity, phase, and tipper data were carefully examined and obviously noisy data points removed. After removing inconsistent measurements, it is important to look at the data to understand what features can be observed at each frequency. This is invaluable to determine the trends and patterns present and allow features subsequently observed in inversion models to be evaluated. For instance conductive structures and also sharp topography changes can have a large response in the ZTEM data. Similarly the MT data at each station were examined to determine regional resistivity trends or identify any distortion.

4.2 Data Collection

In May 2010 Geotech Ltd. carried out a ZTEM survey over the Morrison property, owned by Pacific-Booker Minerals Inc. Fifteen 10.9 km lines were flown with a line spacing of 250 m (Figure 4.1). The survey was flown with flight lines perpendicular to geologic strike with the x-direction aligned to N50°E. The airborne receiver coil measured the vertical component of the magnetic field, and was towed from a helicopter with an average ground clearance of 80 m. The base station receiver consisted of two orthogonal coils to measure the magnetic fields in the x and y-directions corresponding to N50°E and N40°W, respectively. Assuming the magnetic

fields used in ZTEM are spatially and temporally coherent over large distances (Holtham and Oldenburg 2010) the precise location of the base station is not important, as long as it is close enough (5 – 20 km) to represent the horizontal magnetic fields in the survey area.

During ZTEM data processing, measurements from three GPS antennas were used to correct for the motion of the airborne receiver. Filters were applied at power line frequency (60 Hz) and helicopter generated frequencies to eliminate any artificial EM signal. The in-phase and quadrature tipper transfer functions (Eq. 2.19) were processed by Geotech Ltd. to obtain T_{zx} (in-line) and T_{zy} (cross-line) components at six discrete frequencies between 30 and 720 Hz. The highest measurable frequency is the Nyquist frequency, or half of the sampling rate. With this in mind, the airborne receiver digitizing rate of 2000 Hz is capable of measuring up to 1000 Hz, so this was sufficient for the measured 720 Hz data. The lowest measurable frequency was controlled by the helicopter speed. Since the helicopter maintained a speed of 80 km/hr, the 2.5 Hz output data sampling rate gives a measurement about every 9 m. This allowed twelve 30 Hz samples at 9 m increments to estimate the tipper at the lowest frequency, which is a sufficient amount for the 75 x 75 x 75 m mesh cells used in Chapter 5 when solving for the resistivity model.

To compare the airborne ZTEM tipper data to traditional ground-based measurements, a MT survey was completed over the Morrison deposit in July 2013 by a team from the University of Alberta with the assistance of Walcott Geoscience. MT data were collected in the frequency band 300 - 0.001 Hz with Phoenix Geophysics MTU instruments and magnetic induction coils at a total of 37 stations. The station spacing was approximately 500 m over the deposit and increased to 1 km around the deposit to provide regional constraint to the 3-D inversion (Figure 4.1). Vertical magnetic fields were measured at each station to allow comparison to the

Chapter 4: Morrison ZTEM and MT Data Analysis

previously acquired ZTEM data. The MT data acquisition area was limited by available road access and terrain, and as a result the MT survey area was not as extensive as the airborne ZTEM survey (Figure 4.2). In particular the northeastern portion of the ZTEM survey was not sampled by any MT stations. The MT survey grid was not as uniform as the ZTEM survey because the presence of Morrison Lake to the west of the Morrison Graben prohibited the collection of ground MT data in this area.

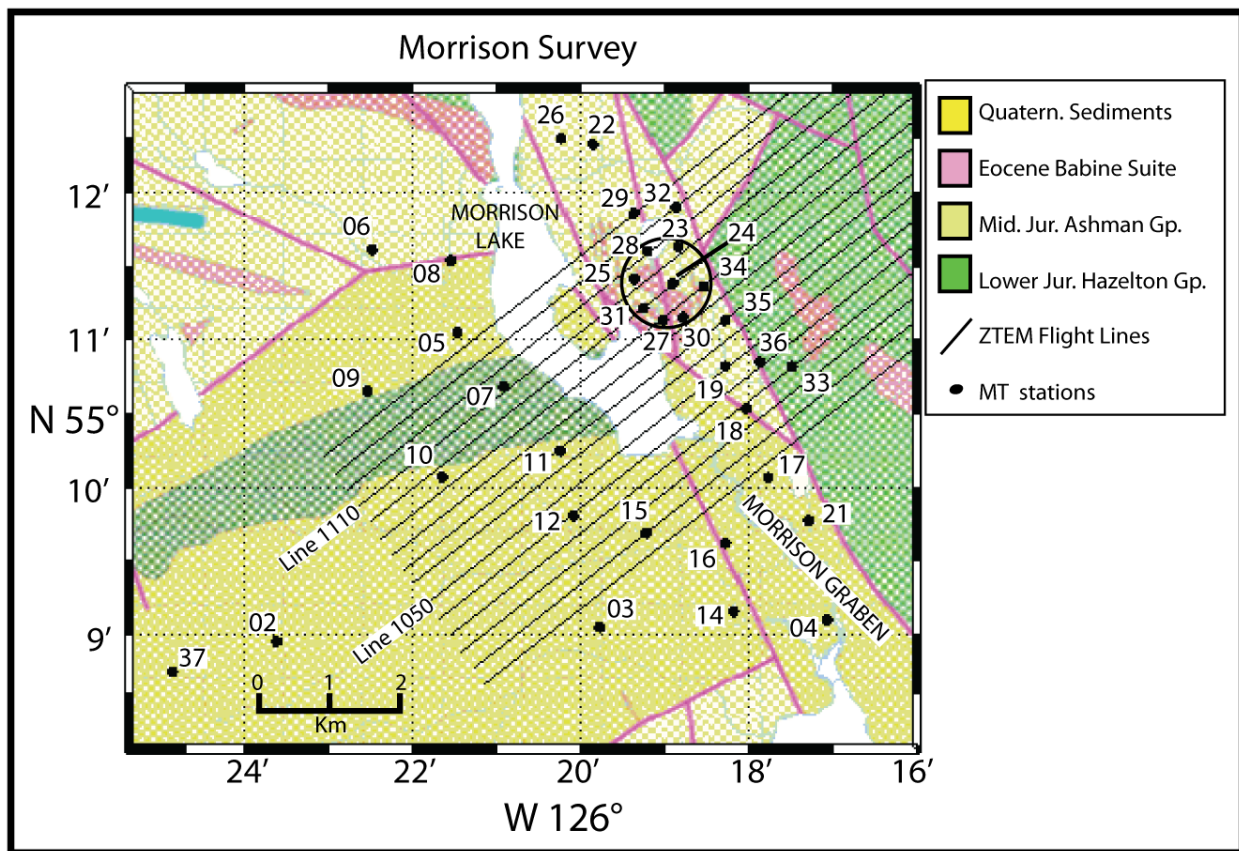


Figure 4.1: Geologic map of the Morrison deposit with locations of the ZTEM survey (black lines) and MT survey (black circles with station number). The deposit area is circled in black. Adapted from BCGS Geoscience, (2005).



Figure 4.2: View looking west over the Morrison deposit. The MT data acquisition area was limited by available road access and terrain.

4.3 ZTEM Data from the Morrison Deposit

The tipper data collected in a ZTEM survey is a dimensionless quantity since it is a ratio of measured magnetic field components in the frequency domain. Typical values are between -0.25 and 0.25, with a zero crossover occurring above a conductor. This is due to the direction of induced magnetic fields when electric current flows along a buried conductor, as shown in Chapter 2. While the tipper provides information about lateral resistivity contrasts, it is also important to consider that lower frequency data correspond to the response of a larger hemisphere below the observation point. This means that low frequency data are sensitive to resistivity structures that are not necessarily directly below the observation point. In this section

the ZTEM data from Morrison will be presented as measured along flight lines and in map view to better observe lateral contrasts. Finally, since the ground is relatively conductive compared to the highly resistive air, topography creates small scale resistivity contrasts near the surface and this effect is observed at high frequency.

4.3.1 Tipper Plots

Plotting the T_{zx} component for individual flight lines shows resistivity contrasts along a 2-D profile. Figure 4.3 shows the two in-phase tipper components in the frequency range 30 – 360 Hz for flight lines L1050 and L1110 (see Figure 4.1 for locations). The T_{zx} component is sensitive to resistivity contrasts in the north-south direction and T_{zy} is sensitive along the east-west direction. However, the flight lines were not oriented along these directions, so the two tipper components are sensitive to structures off the path of the flight lines. For L1050 there is a crossover in T_{zx} close to the deposit at about 3 km that is detected at all frequencies. From 4 – 7 km there is a noticeable difference in the magnitude of the response at each frequency. This is an example of how the tipper is sensitive to different regions of the earth at different frequencies. From 5 – 7 km the T_{zy} component has the largest anomalies at higher frequencies. This part of the profile corresponds with a drastic increase in topography, so the higher frequencies are likely sensing the resistivity contrast between the earth and the relatively resistive air while the lower frequencies are sensitive to larger scale contrasts. Flight line L1110 also shows a considerable difference in response amplitude at all frequencies. At all frequencies the tipper follows the same general trend across the profile, but it is clear that the lower frequency data are influenced by larger scale structure and do not fluctuate as rapidly as the highest frequency responses.

Chapter 4: Morrison ZTEM and MT Data Analysis

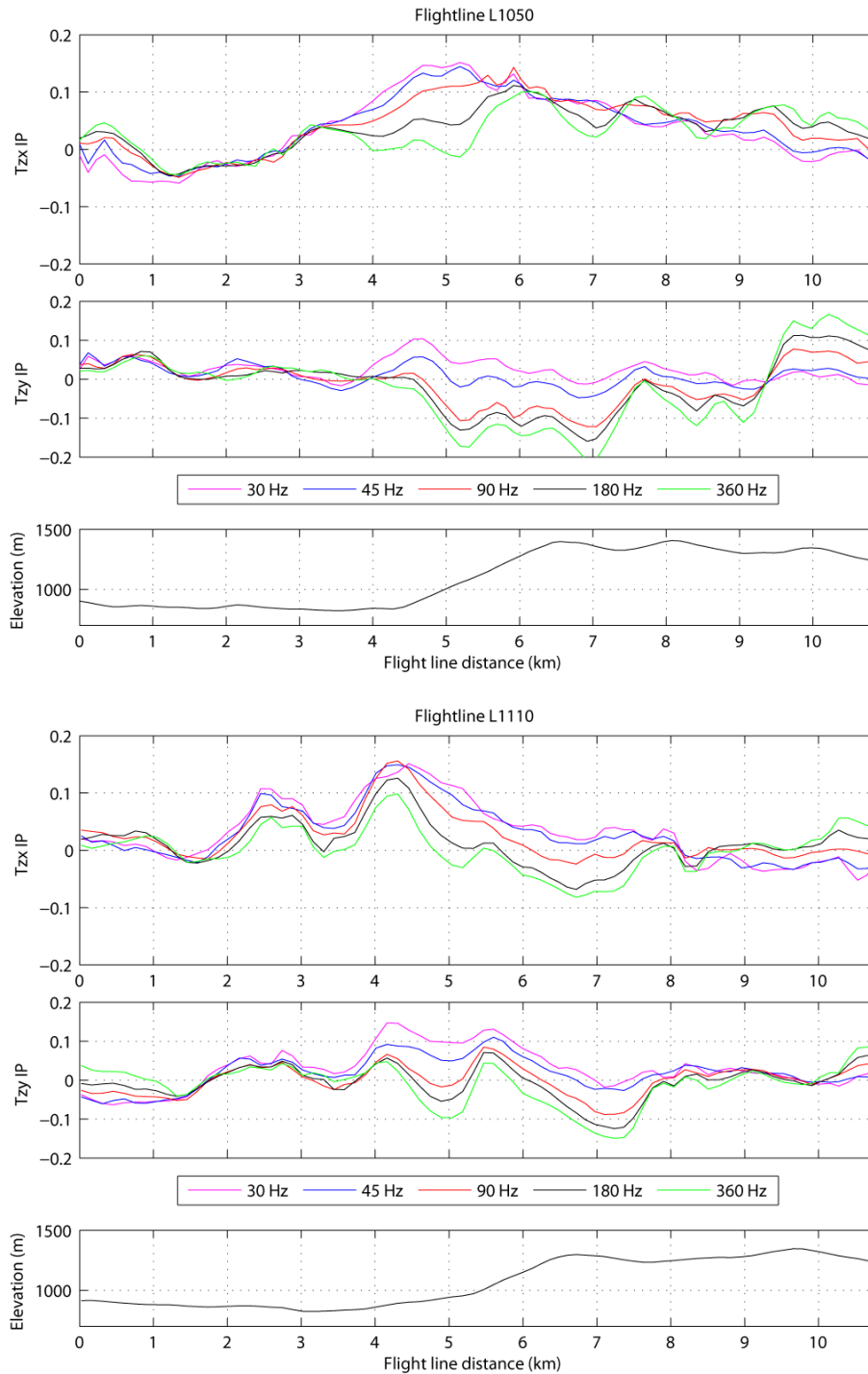


Figure 4.3: In-phase tipper data for ZTEM flight lines L1050 and L1110. The data show a similar trend at all frequencies, but lower frequency data are sensitive to larger scale resistivity contrasts and appear smoother over longer spatial wavelengths. The data diverge considerably at about 4 – 7 km due to varying sensitivity of each frequency to the sharp elevation increase along profile. The x-direction is oriented to geographic north, and the y-direction is oriented to geographic east.

Figure 4.4 shows a map view of the in phase tipper components at Morrison at 360, 90, and 30 Hz. The frequency decreases from the top to the bottom of the figure, as decreasing frequencies are sensitive to deeper areas below ground. The 720 Hz data are not shown since it was not collected for every flight line. Naturally occurring signals at frequencies between 100 – 3000 Hz have lower amplitudes (Ward, 1959), so there may not have been sufficient signal at 720 Hz for every flight line. The left column shows the real T_{zx} component while the right column contains the real T_{zy} . The data have been rotated so that the x-direction is positive north and the y-direction is positive east. In the center of the survey area there is a tipper anomaly in the real T_{zx} component that is present at all frequencies. The response becomes larger in magnitude and area at lower frequencies, suggesting a contribution from a prominent conductor at depth. At higher frequency (360 Hz) the data are sensitive to shallow conductors and large topographic changes as evidenced by multiple small anomalies in the survey area. The real T_{zy} response shows a large negative anomaly at higher frequencies that gradually fades as frequency decreases. This could be a strong response to a sharp elevation change from 750 to 1300 m around the center of the survey area (Figure 4.5). Overall the tipper data is within a reasonable range and the most obvious features correlate with the sharp elevation change in the middle of the survey area.

Chapter 4: Morrison ZTEM and MT Data Analysis

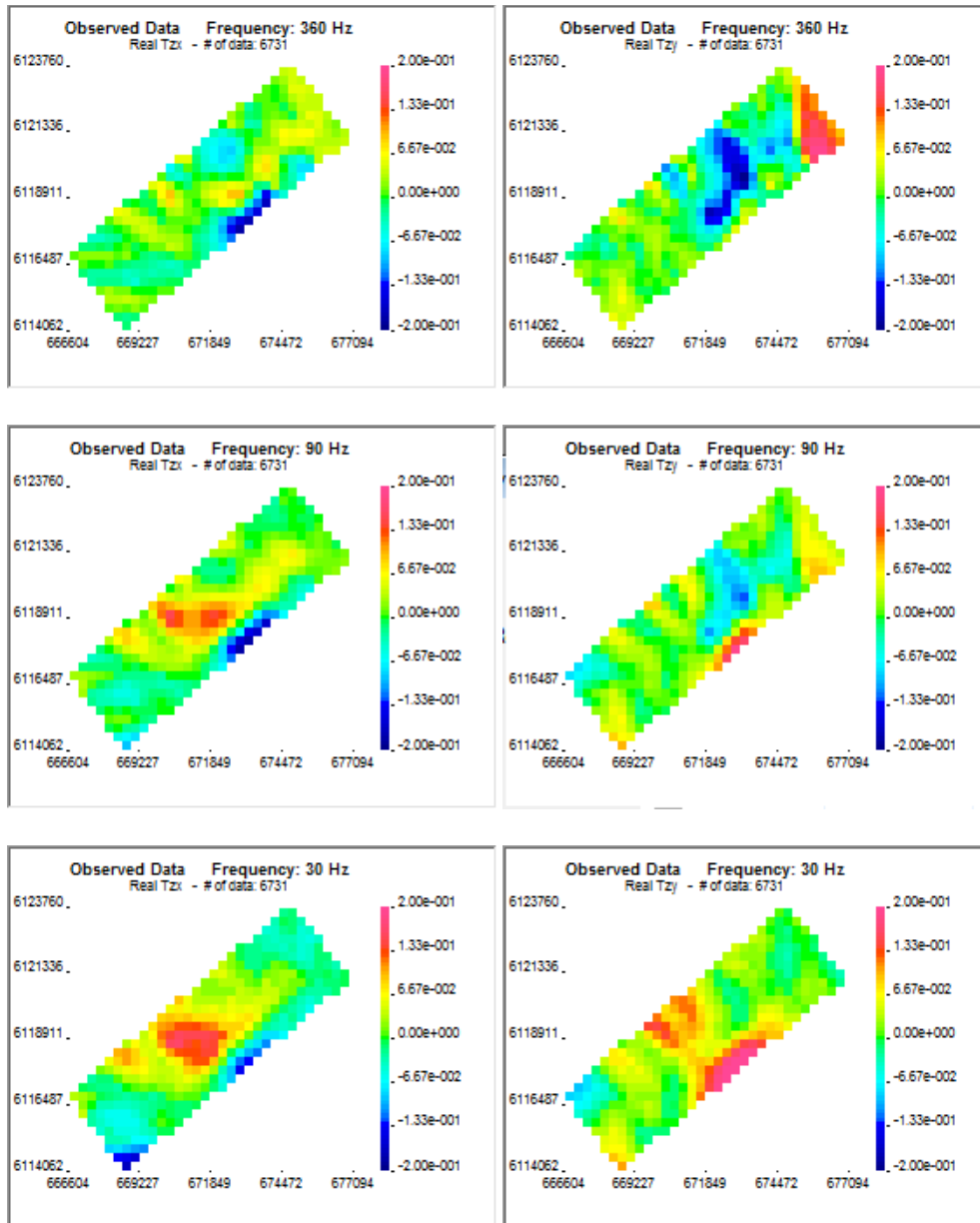


Figure 4.4: Tipper response at Morrison from high (upper) to low (lower) frequency. The left column contains real T_{zx} component and right column is real T_{zy} . The high frequency data are sensitive to shallow resistivity features and topography, while the 30 Hz data are sensitive to deeper resistivity structure. The x-direction is oriented to geographic north, and the y-direction is oriented to geographic east.

4.3.2 Topographic Effect

To evaluate the effect of topography on the measured tipper response, forward data were calculated for a 1000 Ωm halfspace model containing the Morrison topography. Results for the T_{zx} component at 360, 90, and 30 Hz are shown in Figure 4.6. Since the data were calculated from a model with uniform resistivity, all tipper responses must be due to resistivity contrasts between the ground and the air. Large responses indicate that there is significant topography for electric current to preferentially flow through the conductive earth ($\rho_{air} = 1 \times 10^8 \Omega\text{m}$). A portion of the 360 Hz forward data are the same magnitude as the observed data (-0.10 to -0.15), which means topography alone can significantly influence the observed data. This introduces more required features into the inversion and may affect how well the inversion resolves buried conductors. Clearly the resistivity model needs to be finely discretized near the surface to account for the air-Earth interface. Although there is a noticeable effect on the 360 Hz forward data, the topographic response is not as strong for the 90 Hz and 30 Hz data, with most T_{zx} responses between 0.05 and -0.05. At these lower frequencies the tipper is not as sensitive to small-scale changes in topography. This is because the skin depth is greater at these lower frequencies, and the relative contribution of the topography is small compared to the volume sampled at these frequencies.

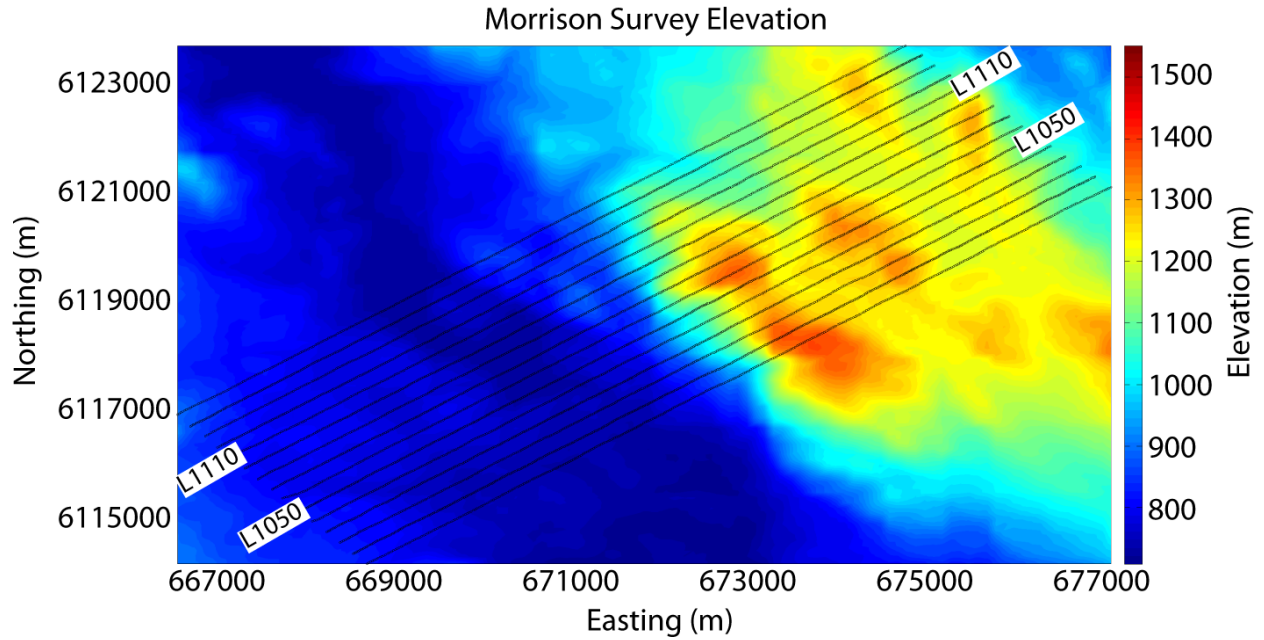


Figure 4.5: Elevation of the Morrison survey area from the Shuttle Radar Topography Mission (SRTM) data. Black lines are the 15 ZTEM flight lines. Flight lines L1050 and L1110 are labelled for reference. There is a large contrast between the southwest and northeast portion of the survey, with an elevation change of over 500 m along some flight lines.

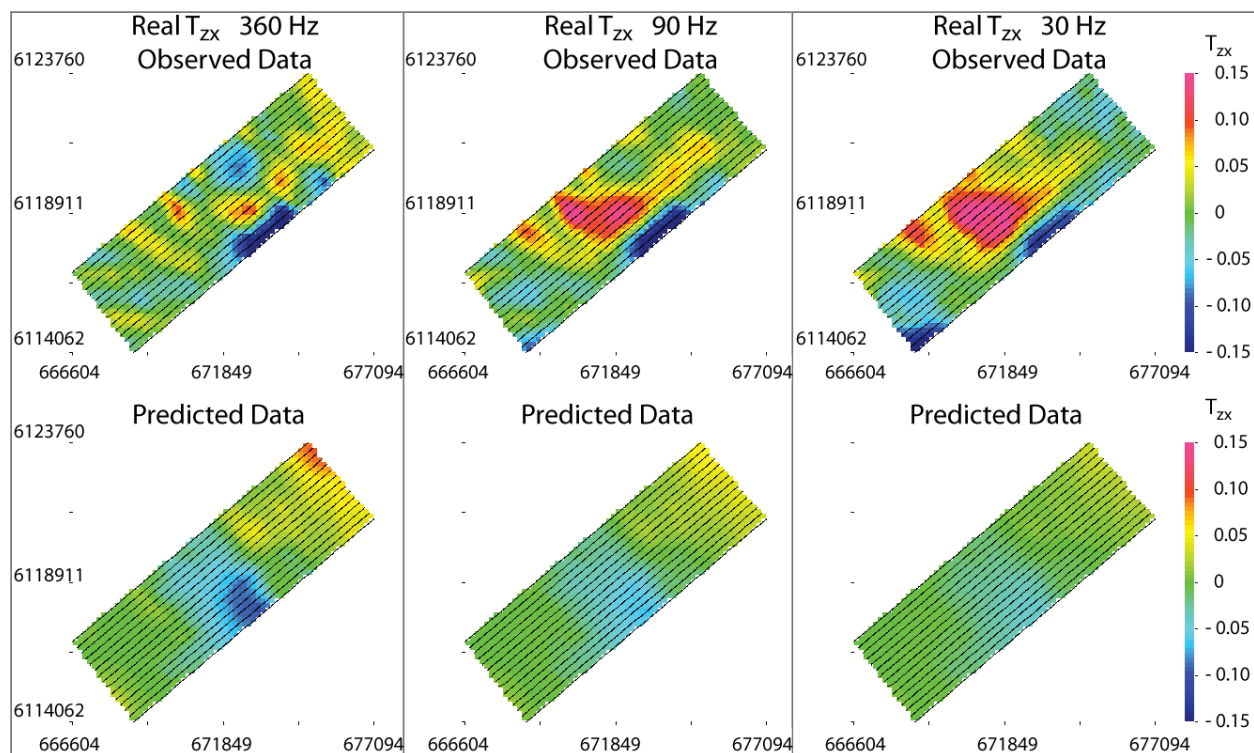


Figure 4.6: Forward modelled response of a 1000 Ωm halfspace with the Morrison survey topography. The top row contains the observed T_{zx} data at 360, 90, and 30 Hz while the bottom row shows the forward data at these frequencies. Features in the forward responses must be due to topographic resistivity contrasts. In the 360 Hz forward data some data are between -0.10 and -0.15, the same magnitude as the observed data. This implies that a significant portion of the 360 Hz observed data could be influenced by topography as well as buried conductors. The magnitude of the 90 and 30 Hz forward responses is lower since the tipper is sensitive to larger scale structures at these frequencies. The x-direction is oriented to geographic north, and the y-direction is oriented to geographic east.

4.4 MT Data at the Morrison Deposit

The MT impedance tensor is a complex valued function of signal frequency, with lower frequencies sampling deeper in the Earth. Impedance data are usually displayed as apparent resistivity and phase curves as derived in Chapter 2. Figure 4.7 shows the apparent resistivity and phase curves for stations MR18, MR24, MR29, and MR32 (see Figure 4.1 for station locations). For each station the red curves represent the xy mode (electric field polarized in x-

direction) and blue curves represent the yx mode (magnetic field polarized in x-direction). Each station is rotated to 0°N so that the x-direction is aligned with geographic north. The data characteristics of these stations will be briefly described to demonstrate the information these data curves contain.

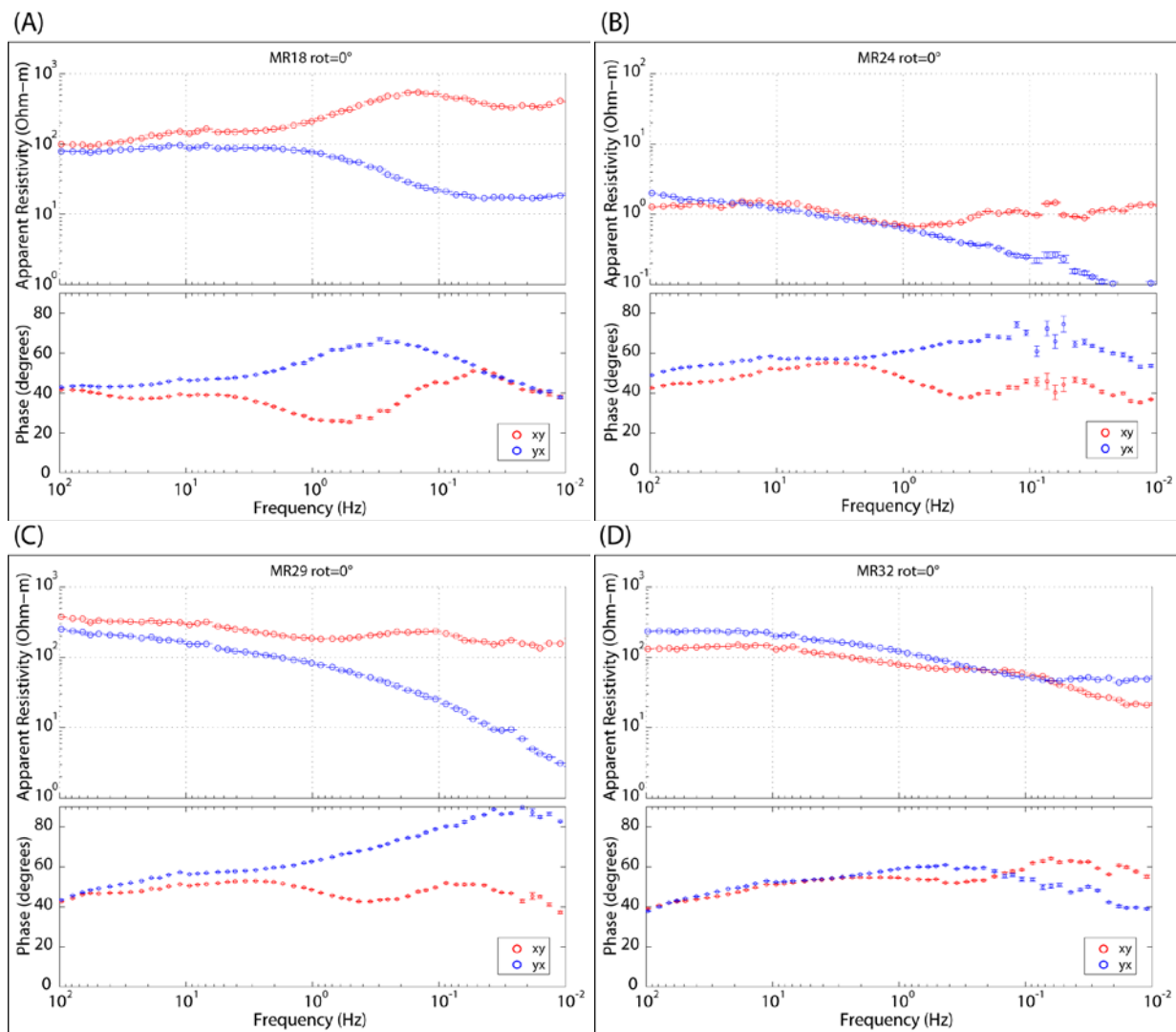


Figure 4.7: Apparent resistivity and phases curves for stations MR18, MR24, MR29, and MR32. Red curves represent the xy polarization (electric field oriented in the x-direction) and blue curves are the yx polarization.

Station MR18 was located southeast of the deposit within the Morrison Graben. Over the frequency range 100 – 5 Hz the apparent resistivity curves remain close to 100 Ωm , and the phase is close to 45°. Between the frequencies of 5 – 0.1 Hz, the xy and yx apparent resistivity curves diverge by about an order of magnitude. The xy apparent resistivity increases and the corresponding phase decreases below 45°. In contrast the yx apparent resistivity decreases and the phase increases above 45°. The Z_{xy} and Z_{yx} impedance elements clearly depend on azimuth in this frequency range, deviating from the nearly 1-D structure observed at high frequencies. At frequencies lower than 0.1 Hz both apparent resistivity curves flatten but remain an order of magnitude apart, and the phases return to 45°.

Station MR24 is located above the main BFP stock. There is clear galvanic distortion at this site as the apparent resistivity at the highest frequencies is two orders of magnitude lower than at stations MR18, MR29, and MR32. The xy and yx apparent resistivity curves show a similar split as seen at station MR18, but at a lower frequency of 1 Hz. The noisy data points at 0.1 – 0.05 Hz were removed prior to inversion.

Stations MR29 and MR32 are located about 500 m apart 1 km north of the main BFP stock. Between 100 and 1 Hz the apparent resistivity and phase curves have the same shape and overall trend of decreasing apparent resistivity. However, the xy apparent resistivity (red curve) appears to be statically shifted for one of these stations. While a static shift changes the level of the apparent resistivity curves by a constant amount, the phase curves should be very similar. The phase curves for MR29 and MR32 show the same character until 1 Hz, suggesting the apparent resistivity for at least one of these stations has been statically shifted. At frequencies below 1 Hz the MR29 yx mode apparent resistivity senses a deep conductor not seen in the MR32 data.

Overall, the apparent resistivity data are of high quality, although there is noticeable galvanic distortion present at some stations. This is clear when comparing station MR24 to the other stations in Figure 4.7. The stations were collected only 2 km from each other but the apparent resistivity values are more than an order of magnitude different. The survey terrain varied between outcropping bedrock and loose dirt, so this effect is noticeable in the data for some stations.

Figure 4.8 shows the Morrison MT impedance data at a frequency of 8.1 Hz. At this frequency the data are sensitive to the deposit and other shallow structures. The Z_{xx} and Z_{xy} components and the Z_{yx} and Z_{yy} components show similar features as they are computed from the same component of the electric field.

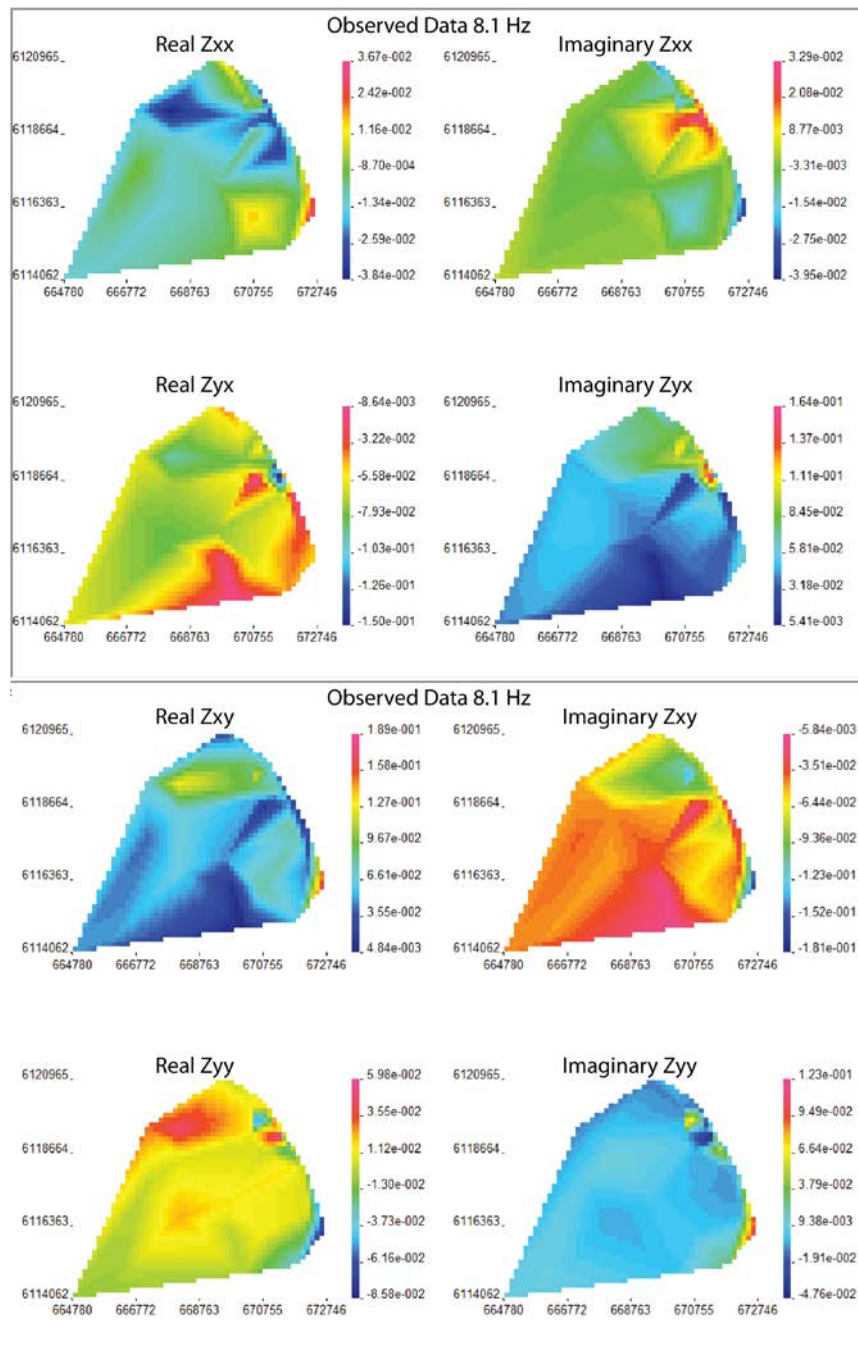


Figure 4.8: Measured MT impedance data for each component at a frequency of 8.1 Hz for the Morrison survey. There are deviations from the regional impedance at the northeast portion of the survey area, where the Morrison deposit is located. The x-direction is oriented to geographic north, and the y-direction is oriented to geographic east.

4.5 Ground and Airborne Tipper Comparison

Since both ZTEM and MT surveys obtained tipper data in the same area both datasets should exhibit similar features. After ensuring the data were in the same coordinate system (details in Chapter 5), the tipper data from each method can be directly compared. The observed tipper data at each MT station location were compared to the tipper data from the closest ZTEM recording location. There is good correlation between the airborne and ground tipper at the overlapping frequencies between 360 - 30 Hz (Figure 4.9).

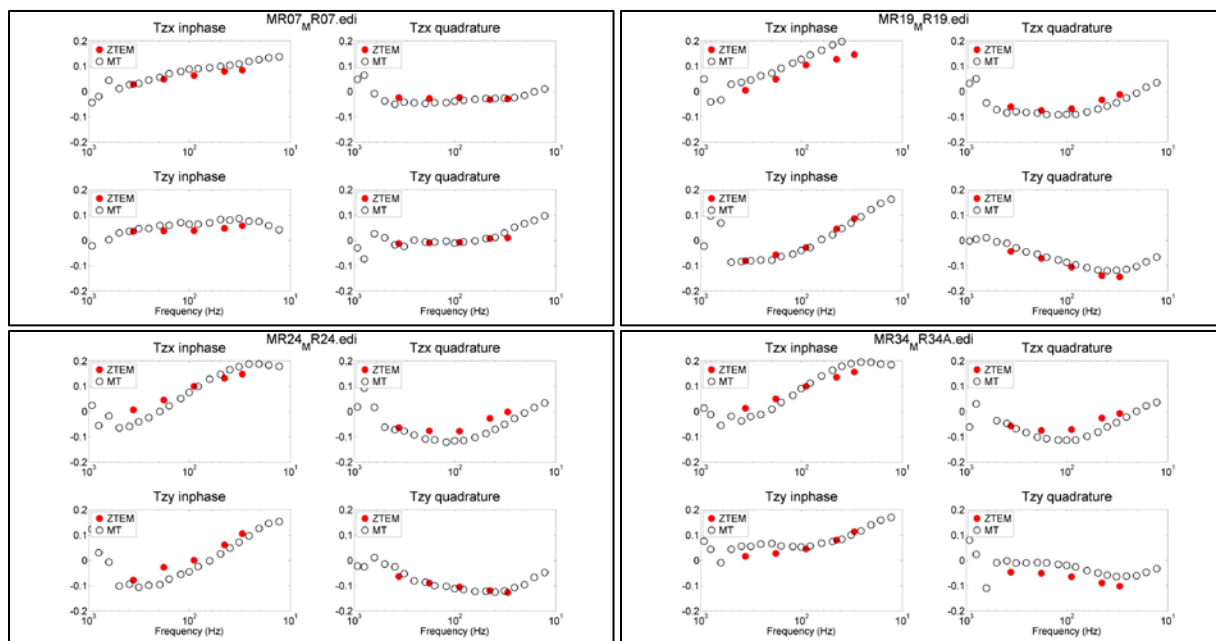


Figure 4.9: Comparison of airborne ZTEM (red circles) and ground MT (open circles) at four MT stations. There is good agreement for all four tipper components.

Another way to compare the two datasets is through a map view of induction arrows. Induction arrows are a graphical representation of the ratio between the real vertical magnetic field and the horizontal magnetic field components at an observation point (Eq. 2.20 and 2.21). Depending on the sign convention used, induction arrows will either point toward or away from resistivity contrasts. The magnitude of the induction arrow is related to the strength of the current flow that produces the vertical magnetic field. Vertical magnetic field data in the form of induction arrows can supplement tensor decomposition in determining the direction of regional geoelectric strike. Figure 4.10 shows a comparison of induction arrows for the airborne ZTEM data and ground MT data at 30 Hz. Since the spatial coverage for the ZTEM data is more widespread than the MT data, only every tenth recording is represented. The direction of induction arrows is somewhat scattered at higher frequencies (360 – 90 Hz) and could reflect small conductive anomalies near the surface. At lower frequencies (45 and 30 Hz) the induction arrow direction becomes more well-defined, and is consistent with the regional geologic strike direction of N45°W. The induction arrow direction of the ZTEM and MT surveys matches well at a frequency of 30 Hz.

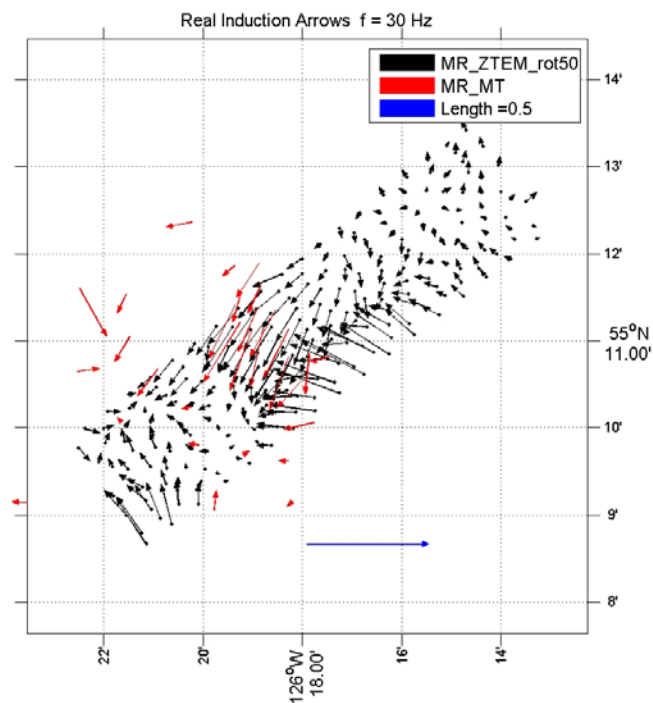


Figure 4.10: Induction arrows for the MT (red) and ZTEM (black) data at a frequency of 30 Hz. The arrows are in good agreement at this frequency. In the Parkinson convention the arrows point toward conductive features.

4.6 Summary

Airborne ZTEM data and ground MT data were collected over the Morrison deposit and the tipper data from each correlate with each other very well. The ZTEM tipper data are sensitive to topographic changes, and a significant portion of the high frequency response is due to topography alone. This suggests that a fine mesh must be used to accurately reflect the topography when creating the resistivity model. The MT data are mostly smooth after data processing; however there appears to be galvanic distortion present at some sites that shifts the magnitude of the apparent resistivity. In Chapter 5 the ZTEM and MT data are prepared for inversion and individual inversions with various parameters will be presented and evaluated.

Chapter 5: Individual ZTEM and MT Inversions of the Morrison Data

5.1 Introduction

In Chapter 4 the characteristics of the ZTEM and MT data collected at the Morrison porphyry deposit were described. The observed data are the MT impedance and the ZTEM tipper, both of which are a function of frequency. In this chapter these data will be used to create a 3-D resistivity model of the deposit where the resistivity varies spatially within the Earth in three dimensions. Construction of a resistivity model that fits the measured MT or ZTEM data could be done with trial and error forward modeling. However it is much more efficient to use an inversion algorithm to automatically construct a resistivity model that fits the measured data to within a specified statistical tolerance.

To understand the relationship between measured data and model, the characteristics of the geophysical forward and inverse problems should be understood. For a specified resistivity model, the predicted data (e.g. MT impedance) can be calculated uniquely. This is known as the forward problem in geophysics. However, converting measured MT or ZTEM data into a resistivity model of the subsurface requires that the inverse problem is solved and it is well known that this is non-unique; i.e. there are an infinite number of resistivity models that could explain a set of observed data (Backus and Gilbert, 1967). The goal of the inversion algorithm is to determine a suitable resistivity model whose forward response matches the observed data to within a specified tolerance, and which also satisfies additional requirements to overcome the non-uniqueness; i.e. spatial smoothness, close to a specified model, etc. Most inversion

algorithms start with an initial resistivity model, which is updated in a series of iterations until the data misfit is reduced to a specified value. As stated above, the inverse problem is non-unique, so additional knowledge is required to determine whether the final inversion model is realistic.

In 3-D inversion the number of model parameters, and thus the size of the system of equations to be solved, is much greater than in a 2-D inversion. However, complicated model geometries can be replicated in a 3-D inversion since no dimensionality assumptions need to be made about the subsurface and the full MT impedance tensor is used. Advances in computational power have made 3-D inversion more practical in recent years and this has fueled the development of 3-D inversion codes such as those of Newman and Alumbaugh (2000), Sasaki (2001), Farquharson et al. (2002), Siripunvaraporn et al. (2005), and Kelbert et al. (2014). For the study at the Morrison deposit, an inversion code with the flexibility to perform single and joint inversions and the ability to model topography and handle a fine topographic mesh was needed. A variant of the Farquharson et al. (2002) 3-D inversion code described in Holtham and Oldenburg (2010) was chosen for these reasons.

The ZTEM and MT data were initially inverted individually to investigate the resolution and sensitivity of each technique. A joint ZTEM-MT inversion was then run to utilize the advantages of each technique, and this will be described in Chapter 6. This chapter describes the process of preparing the data and choosing the optimal settings to guide the individual ZTEM and MT inversions. As discussed in Chapter 4, the survey areas covered by the ZTEM and MT studies overlapped over the Morrison deposit and should detect a similar resistivity signature. This chapter covers the inversion procedure for ZTEM and MT data, including:

- Data preparation
- Model mesh creation
- Choosing the initial model

It will be shown that the resistivity models for the separate ZTEM and MT inversions are generally similar in the area where the two surveys overlap. It is also clear that each technique is sensitive to different parts of the resistivity model considering the different frequency ranges used.

5.2 The Inversion Algorithm

The ZTEM and MT data were inverted using the UBC GIF e3dMTinv code. This algorithm was adapted by Holtham and Oldenburg (2010) for ZTEM inversion and was a development of the algorithm for MT inversion developed by Farquharson et al. (2002). The code is a Gauss-Newton algorithm variant that seeks to minimize the objective function Φ which consists of two terms (1) the misfit between observed and predicted data ϕ_d and (2) a model norm ϕ_m that quantifies the model properties:

$$\Phi = \phi_d + \beta \phi_m \quad (5.1)$$

where β is the cooling term that is gradually decreased at each iteration until the desired misfit is achieved. The measure of data misfit ϕ_d is the sum of squares weighted by the data uncertainty:

$$\phi_d = \|\mathbf{W}_d(\mathbf{d}^{obs} - \mathbf{d}^{pred})\|_2^2 \quad (5.2)$$

where \mathbf{d}^{obs} and \mathbf{d}^{pred} are vectors containing the observed and model predicted data, respectively; \mathbf{W}_d is a diagonal matrix containing the reciprocals of the data uncertainties, and $\|\cdot\|_2$ represents the l_2 norm. The model norm is defined as:

$$\phi_m = \sum_{k=1}^4 \alpha_k \|\mathbf{W}_k(\mathbf{m} - \mathbf{m}^{ref})\|_2^2 \quad (5.3)$$

where \mathbf{W}_1 is a diagonal matrix, and \mathbf{W}_2 , \mathbf{W}_3 , and \mathbf{W}_4 are the first order finite-difference matrices for the x , y , and z directions, respectively. The vectors \mathbf{m} and \mathbf{m}^{ref} contain the cell resistivities of the recovered and reference model, respectively. The factor α_1 (or α_s) controls the closeness of the inversion model to the reference model, and $\alpha_{x,y,z}$ controls the spatial smoothing in the x , y , and z directions, respectively.

At each iteration the resistivity model is updated to lower the misfit function, Φ . The inversion stops when the misfit reaches the desired amount, typically a sum of squares misfit equal to the number of data points. This typically requires 3 – 7 days using 6 – 18 processors (depending on the number of frequencies inverted) on a Compute Canada Westgrid cluster.

The inversion code utilizes an octree mesh generated by the UBC GIF software. The octree mesh consists of cells whose size is a multiple of the minimum cell size. This allows for increasingly larger cells away from the main survey area without prohibitively increasing the total number of model cells in the mesh (Figure 5.1). Choosing the minimum cell size is a trade-off between model resolution and computational efficiency. The cell size should be small enough to accurately reflect topographic changes in the survey area while providing resolution for the EM skin depth at the highest frequency data (see Chapter 2 for derivation of the frequency-dependent skin depth). For example, it is especially important with the airborne ZTEM survey to ensure the model correctly places the observation points above ground. In natural source EM data, the data frequency range is also an important consideration in mesh design. The modelling domain should be large enough to provide space for the lowest frequency (deep penetration) data to be fully represented. In contrast, the highest frequencies (shallow penetration) require small

cells around the observation points to ensure there is fine enough resolution. The mesh should also extend at least three skin depths (at the lowest frequency) away from the center to ensure that all signal has attenuated before reaching any boundary (Weaver, 1994). Three skin depths should be sufficient since the decay of the signal is proportional to $1/e$.

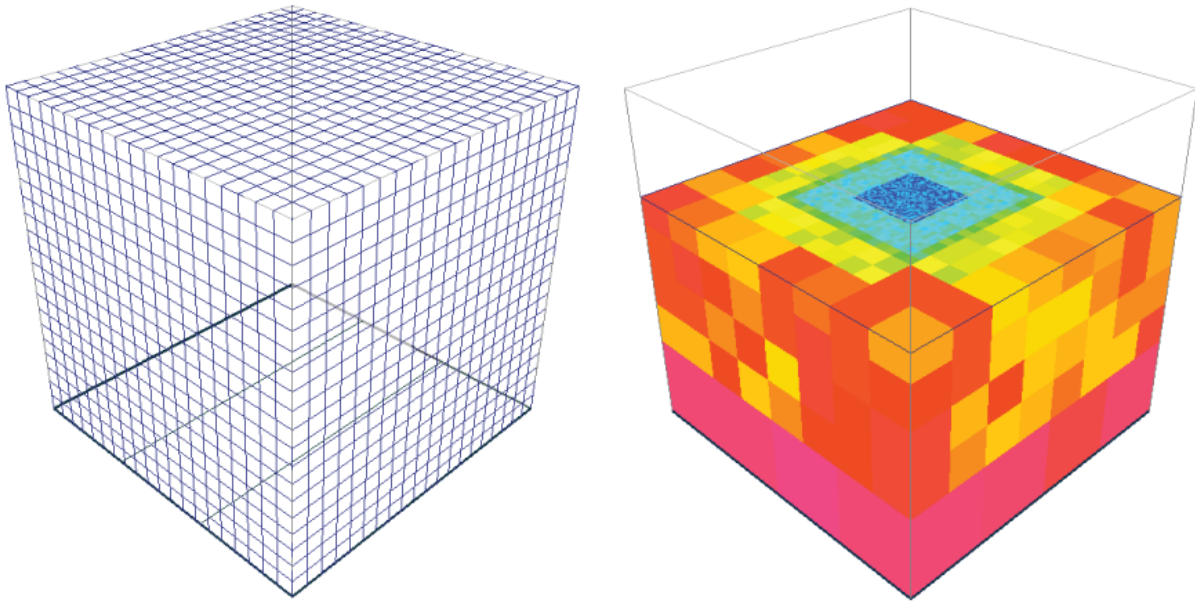


Figure 5.1: Example of a rectilinear mesh with a regular cell size (left) and an octree mesh with variable cell size (right). The octree mesh contains many small cells (indicated in blue) in the core region and larger cells (red and pink) near the mesh edges. This allows for a manageable number of total cells while satisfying electromagnetic skin depth conditions to accurately model the electromagnetic fields. Figure generated using UBC-GIF MeshTools3D software.

To summarize the inversion procedure, computations are done within the model domain (model cell resistivities) and the data domain as predicted data for the inversion resistivity model. The inversion begins with the starting model, a vector containing the resistivity of each cell in the mesh. Without any prior information, the initial model is usually set so that each cell has the same resistivity. At each iteration the sensitivity of the predicted model data due to changes in the model resistivity is calculated, and the model resistivities are updated so that the

misfit between the predicted model data and the observed data is decreased. In addition to the data misfit, the model norm also needs to be minimized. The model norm accounts for spatial smoothing and closeness to a reference model. If a reference model is defined, the inversion will keep the predicted model resistivities close to the reference model in order to keep the model norm low. To account for spatial smoothing, the inversion will reduce resistivity contrasts between neighboring cells if the smoothing parameter is increased for any of the spatial directions. The inversion is completed when the data misfit between the observed data and the predicted model response is decreased below a prescribed threshold. The desired misfit is typically equal to the number of data points (Eq. 5.2).

5.3 ZTEM and MT Data Convention

Before inverting data, it is crucial to ensure that all the data are in a consistent and appropriate coordinate system. For instance, MT data collection may use a non-geographic coordinate system, e.g. with instruments oriented in geomagnetic coordinates. For the Morrison MT survey the data were collected with reference to magnetic north, and subsequently the reference frame was rotated by positive 19° to correct for magnetic declination. The Geotech ZTEM survey was performed with the x-axis (in-line component) aligned to $N50^\circ E$ geographic, perpendicular to the regional geological strike. Thus the reference frame must be rotated by 50° to orient the ZTEM data components to geographic north. In addition, the right-handed coordinate system used for the ZTEM data treats the positive-z direction as upward, while the MT positive-z direction is downward into the ground. If both datasets treat the x direction as north, then the y coordinates of one must be negated to match.

The ZTEM profile sign convention must also be considered. Since tipper data change sign over resistivity contrasts, there are two possible conventions for the cross-over. The ZTEM data are processed to reflect a positive-negative sign change when flying over a conductor perpendicular to profile (Figure 5.2). The processed MT data exhibit the opposite convention, so the ZTEM tipper components were negated to match the convention. This sign change is analogous to the Parkinson or Wiese convention for induction arrow direction (Parkinson, 1959; Wiese, 1962). Each convention adopts the opposite direction of the induced vertical magnetic field, with Parkinson induction arrows pointing toward conductors and Wiese arrows pointing away.

Finally, the sign of the quadrature tipper component must be consistent for the ZTEM and MT data. This term arises from the choice of time variation used in data analysis. Although either choice of sign is appropriate, it is important to ensure a consistent convention when working with multiple datasets. The ZTEM data were processed assuming a time variation of the form $e^{-i\omega t}$, while the MT data processing used $e^{i\omega t}$. Since the UBC-GIF e3dMTinv inversion assumes $e^{-i\omega t}$, the sign for the MT quadrature impedance component must be negated prior to inversion.

The net results of data rotation and sign changes are summarized in the Table 5.1. Both datasets were rotated to align to geographic north, while the net effect of sign changes was negating the real and imaginary T_{zx} ZTEM components. In Chapter 4 the reference frames were shown to be the same by induction arrows and tipper plots as a function of frequency.

Data Acquisition Parameters				
	Magnetic ref	Tipper convention	Positive Y direction	Quad sign
ZTEM	N50°E	+/-	West	Positive
MT	N19°E	-/+	East	Negative
Rotations and Sign Corrections				
	Magnetic ref	Tipper convention	Positive Y direction	Quad sign
ZTEM	Rotated to 0°N	Negated	Negated	Negated
MT	Rotated to 0°N	None	None	None

Table 5.1: Survey conventions and corrections for the Morrison ZTEM and MT data.

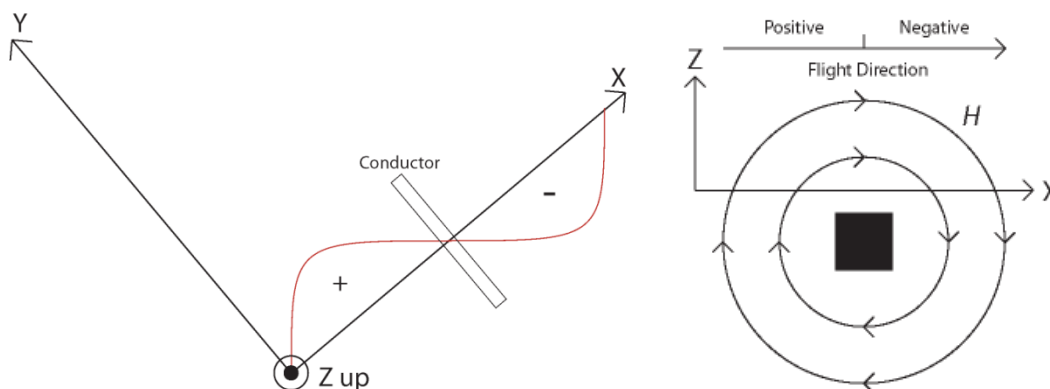


Figure 5.2: Sign convention of the Morrison ZTEM survey. Tipper values do not show minimums or maximums above anomalies, instead they exhibit zero-crossovers. Left: The sign of the tipper changes when traveling over a conductor in the positive x-direction from positive to negative. This is due to the change in the direction of the vertical magnetic field component. Right: Cross section view showing the sign change when flying over the same conductor.

5.4 ZTEM Inversion

After checking that the ZTEM data were in the correct geographic reference frame, the data uncertainty and starting model mesh were considered. The procedure for setting up these parameters will be described in sections 5.4.1 and 5.4.2. This includes assigning data uncertainties for the inversion and choosing a starting resistivity model. Next, the inversions were run in several stages:

Chapter 5: Individual ZTEM and MT Inversions of the Morrison Data

- (a) Preliminary inversions were run to determine an appropriate value for the ZTEM data uncertainties. The ZTEM data were inverted at individual frequencies to ensure that the uncertainty values allowed the inversion to closely fit the measured ZTEM data. These are described in Section 5.4.3.
- (b) The next set of inversions tested the number of observation points needed to obtain a coherent model. Even when the number of data points in the dataset was reduced through down sampling, there was not a significant change to the total computational time. These inversions are described in Section 5.4.4.
- (c) Finally, in Section 5.4.5 the ZTEM inversions were initiated with different starting model resistivities to see the effect on the final model.
- (d) After experimenting with inversion parameters, Section 5.4.6 shows the optimal model chosen that sufficiently reduces the data misfit and provides a resistivity model consistent with the known deposit geology.

5.4.1 Assigning Data Uncertainties

Uncertainties in ZTEM data measurement are caused by numerous factors, and it can be difficult to quantify each of them. These include, but are not limited to, sensor movement during data collection and theoretical approximations such as the plane wave assumption. Underestimating the data uncertainties may cause the inversion to fit noise in the ZTEM data. Conversely, overestimating the uncertainties may lead to a resistivity model that does not fully reflect all the features in the measured ZTEM data. For EM data inversion it is common to set data uncertainty as some percent of the data plus a small absolute error floor. ZTEM data are unique because they possess a small dynamic range, with typical tipper values between -0.5 and 0.5. For the ZTEM inversion the uncertainty was set as 2.5% of the observed data plus a small error floor of 10^{-9} .

5.4.2 Initial Model and Mesh

In contrast to MT impedance data, ZTEM data are derived from only the magnetic field components. Thus absolute values of electrical resistivity cannot be recovered in the ZTEM inversion model. As a result it is critical to begin the inversion with an initial resistivity model that closely reflects the true resistivity of the survey region. Even if the true resistivity is unknown, Holtham and Oldenburg (2010) showed that trial forward calculations can help determine a suitable starting model. The misfit between the observed ZTEM data and the forward modelled data for the first iteration was computed for various starting resistivities. The results showed that a 1000 Ω m starting model would provide the lowest initial misfit for the ZTEM data and serve as an appropriate starting model (Figure 5.3). The presence of Jurassic Hazelton volcanic sediments in the ZTEM survey block suggest a high starting resistivity, as this unit is expected to be highly resistive.

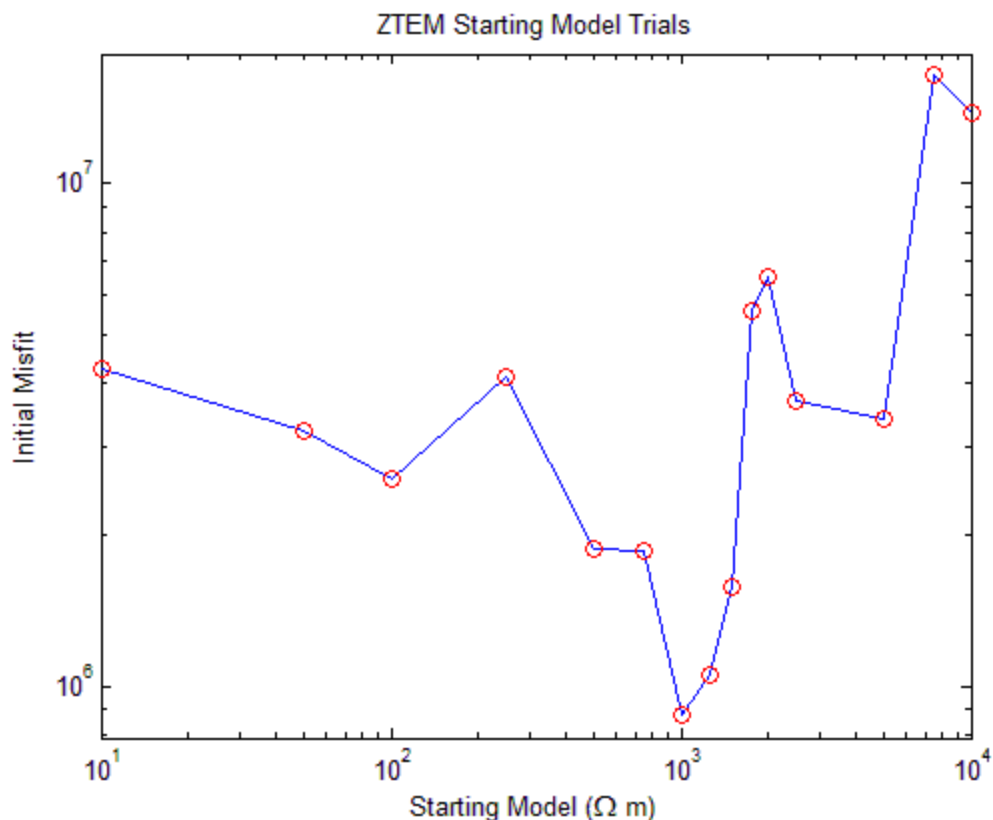


Figure 5.3: Initial inversion misfit using several starting model resistivities. A starting model of 1000 ohm-m was selected for the ZTEM inversion because of the lowest initial misfit.

As previously mentioned, a computational trade off must be considered when constructing the model mesh as decreasing the minimum cell size can prohibitively increase memory requirements and total inversion time. The mesh was designed so that each dimension was at least three times the maximum skin depth (calculated from the lowest frequency) from the center of the mesh. The octree mesh was constructed with 75 x 75 x 75 m as the smallest cell size, allowing small enough cells for the highest frequency (360 Hz) data to be modelled. These small cells extend to 1 km below sea level, which allows for resolution of shallow, small-scale features. The Morrison property contains a 700 m topographic change within the survey area, so it was important to have cells small enough to accurately reflect the topography (Figure 5.4).

This is crucial in ZTEM inversion as all measurement points are above ground. The cells expand in size closer to the edges of the mesh, since there is limited resolution due to signal attenuation farther from the survey area. The largest padding cells at the edges of the mesh were 256 times larger than the minimum cell size.

Finally, the ZTEM base station must also be included within the model domain. During data acquisition the base station can be placed many kilometers away from the ZTEM flight lines. This could add a large amount of cells to the inversion mesh. However, Holtham and Oldenburg (2010) showed that because no assumptions are made about the underlying conductivity structure, the actual base station location within the model does not significantly affect the inversion result. To minimize the number of cells in the mesh, the base station location was moved to the southwest corner of the ZTEM lines.

5.4.3 Single Frequency ZTEM Inversions

Before inverting all five ZTEM frequencies at once, it is important to run single frequency inversions to check data quality and to ensure that suitable uncertainties were applied. Inversions were run for single frequencies between 360 – 30 Hz, and all converged to their desired misfit. These inversions are summarized in Table 5.2. Each inversion used a starting resistivity model of 1000 Ωm , as determined from the test in section 5.4.2. Since each single frequency inversion was able to closely fit the ZTEM data, the next test was to simultaneously invert all five frequencies.

Single Frequency ZTEM Inversions						
Frequency	Data Points	Starting Model (Ωm)	Error %	Target Misfit	Final	Final/Target Misfit
30 Hz	13462	1000	2.5	53848	52342	0.97
45 Hz	13462	1000	2.5	53484	45071	0.84
90 Hz	13462	1000	2.5	53484	38273	0.72
180 Hz	13462	1000	2.5	53484	36611	0.68
360 Hz	13462	1000	2.5	53484	37276	0.70

Table 5.2: Inversion parameters for single frequency inversions of the Morrison ZTEM data.

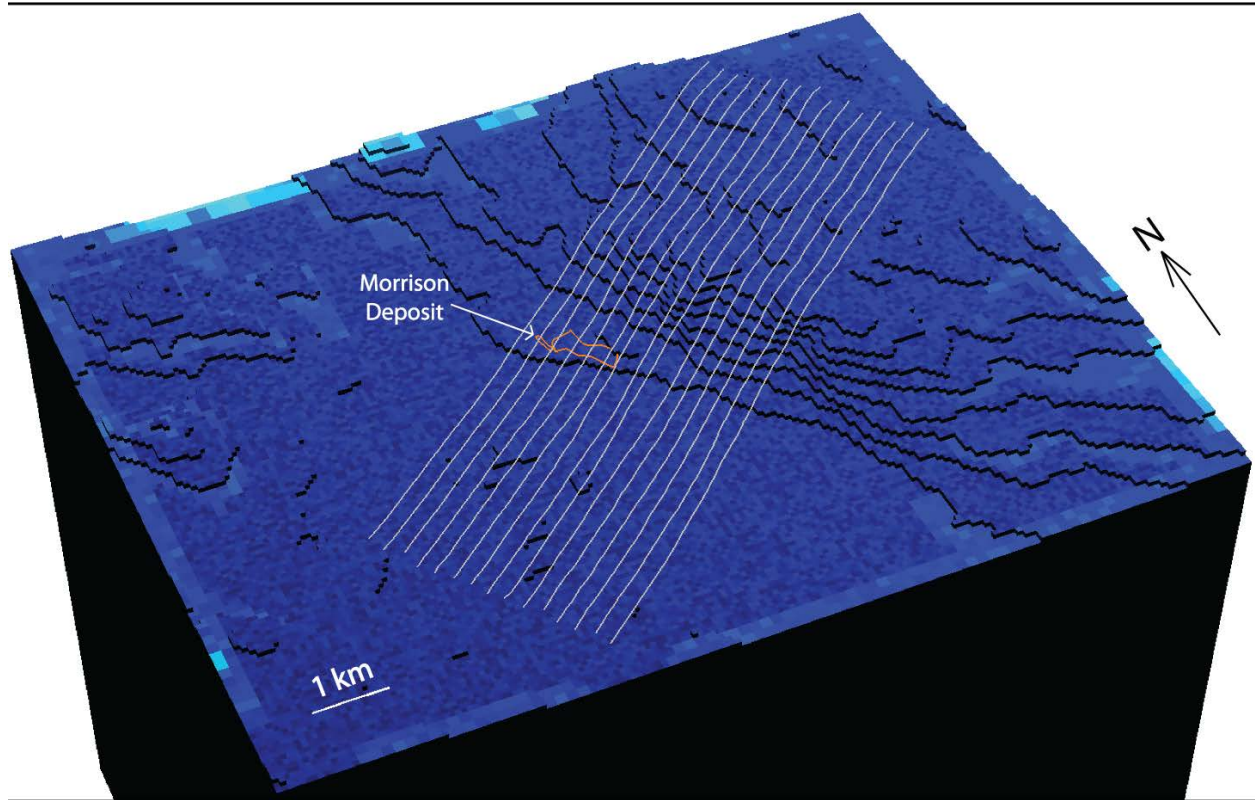


Figure 5.4: Core region of the inversion mesh containing 75 x 75 x 75 m cells. White lines are the ZTEM flight lines, and the Morrison deposit is outlined in red. The sharp rise in elevation to the east of the deposit must be finely discretized to accurately reproduce the true topography.

5.4.4 Spatially Downsampled ZTEM Inversion

The second set of inversions tested whether the resistivity model resolution would decrease from using a subset of the ZTEM data. Having more measurement locations should provide more information to recover an accurate resistivity value for each model cell. However, for the purpose of the joint ZTEM-MT inversion described in Chapter 6 the total amount of each type of data affects the data weighting in the inversion. ZTEM surveys typically collect a large amount of data, but it is beneficial to be close (within an order of magnitude) to the amount of MT data to avoid applying large scaling factors. For example, a scaling factor must be applied if a joint inversion contains 40,000 ZTEM data (10 flight lines, 1,000 observations per line, 4 tipper components) and only 800 total MT data (10 stations, 10 frequencies, 8 impedance components). The data scaling ensures that each individual data point is weighted equally so that the small amount of MT data influence the inversion model as much as the ZTEM data. The scaling factor is described in detail in Chapter 6. Here the ZTEM data are down-sampled by various amounts to test if the sparser ZTEM data can still be fit by the inversion and if the resistivity model remains stable and physically reasonable. This allows for a subset of the ZTEM data to be used in the joint inversion in Chapter 6.

If the ZTEM data are down-sampled too much, the inversion resistivity model resolution should decrease since there would be less data to accurately determine the resistivity of each cell. Comparing the minimum model cell size to the data spatial sampling gives an idea of the inversion resolution. The Geotech Ltd. airborne sensor had a digitizing rate of 2000 Hz and a data sampling rate of 2.5 Hz, equivalent to a measurement approximately every 9 m along each flight line. Each inversion was run using the same mesh with a minimum cell size of 75 x 75 x 75 m. Without down-sampling the ZTEM data, there should be approximately 8 measurements per

cell along each flight line. Seven inversions were run using a range of data from all 13,462 measurements down to approximately one-tenth of the measurements (1,347) to see if there was an effect on the recovered resistivity model. As the dataset is further down-sampled, there are fewer observation points per cell to determine the resistivity. These inversions are summarized in Table 5.3. Figure 5.5 shows the observed and predicted real T_{zx} component at 90 Hz for the inversion using all measurements (left panel), one half of the measurements (center panel) and one tenth of the measurements (right panel). It is clear that reducing the number of measurements by one half or even one tenth does not visibly affect the observed data. Furthermore, the three inversions were able to closely fit the predicted data to the observed data shown in the upper half of each panel. Each inversion was able to reduce the sum of squares misfit to 1. There is no noticeable difference in structure or resistivity values between the inversion resistivity models shown in Figure 5.6.

Downsampled ZTEM Inversions						
Frequencies	Data Points	Starting Model (Ωm)	Error %	Target Misfit	Final Misfit	Final/Target Misfit
360 – 30 Hz	13462	1000	2.5	269240	255010	0.95
360 – 30 Hz	6731	1000	2.5	134620	129435	0.96
360 – 30 Hz	1684	1000	2.5	26928	26001	0.97
360 – 30 Hz	1347	1000	2.5	21552	21395	0.99

Table 5.3: Inversion parameters for the down-sampled inversions of the Morrison ZTEM data.

Chapter 5: Individual ZTEM and MT Inversions of the Morrison Data

In addition to preparing for joint inversion, reducing the number of ZTEM measurement points without compromising the inversion model makes sense if it increases computational efficiency. However, the three inversions each took about 70 hrs to converge to the desired misfit. There was not a significant correlation between fewer data and lower computational times. This is because the number of cells used in the inversion model has a much larger impact than the number of data parameters on the computational speed of the UBC inversion code. However, the value of using a subset of the densely sampled ZTEM data will be discussed in Chapter 6.

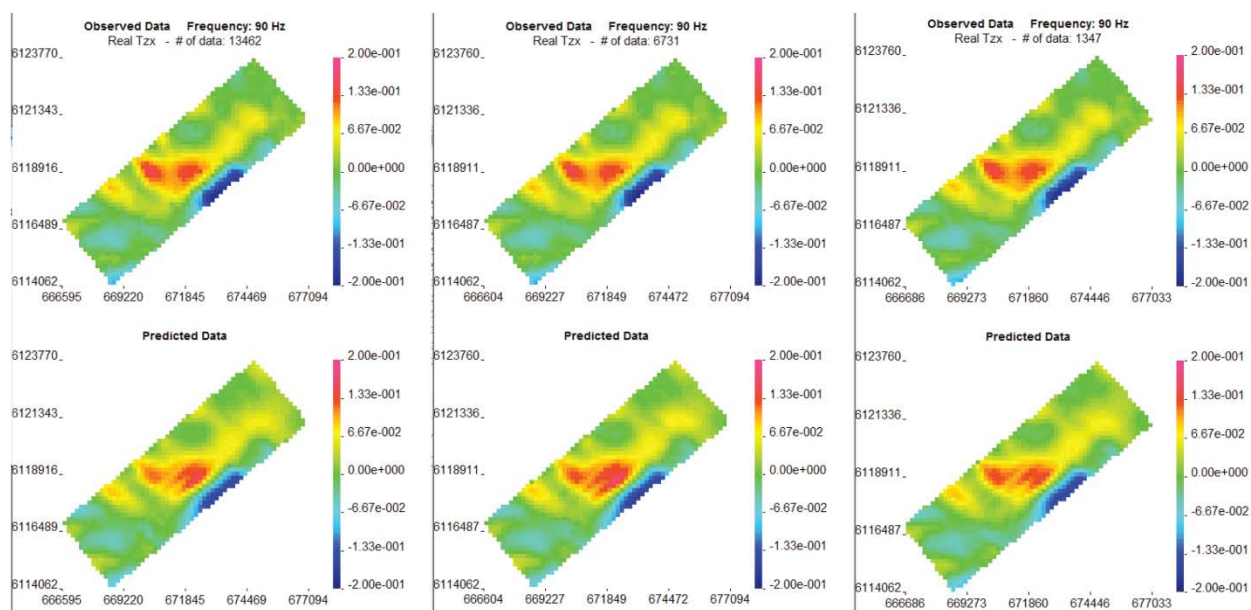


Figure 5.5: Observed and predicted T_{zx} component data (with x-direction oriented north) for ZTEM inversions with 13,462 observation points (left panel), 6,731 observation points (middle panel) and 1,347 observation points (right panel). In each panel the upper half is the observed data, and the bottom half is the model predicted data. The tipper amplitudes are extremely similar in all three cases, so it is not necessary to invert the entire dataset.

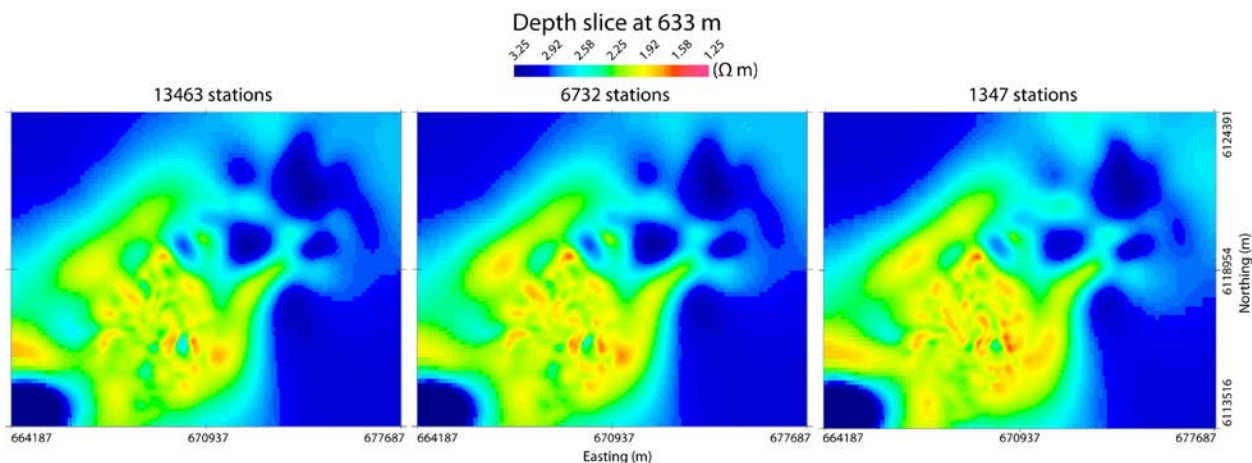


Figure 5.6: ZTEM inversion model depth slices at 633 m above sea level using all 13,462 ZTEM data points (left), one half (6,731) of the data points (middle), and one tenth (1,347) of the data points (right) The three models are extremely similar in structure and resistivity amplitude.

5.4.5 Effect of the Starting Model

The initial resistivity model must be chosen so that the relative resistivity contrasts reflect the character of the true model. Although 1-D layered resistivity models will not produce tipper data, the background resistivity still affects the resistivity values of any anomalies. Thus it is important to choose a starting model that results in a good estimate of resistivity contrasts and fits the observed data. To test the importance of the starting model resistivity, three additional ZTEM inversions were run using starting models of 100 Ωm , 500 Ωm , and 5000 Ωm (Table 5.4). The 100 Ωm and 5000 Ωm inversions seem too far from the true model as these inversions failed to reach the target misfit. Even though these models obtained relative resistivity contrasts, it is apparent that the resistivity values did not accurately match the true model. While the 500 Ωm inversion reached the target misfit, the 1000 Ωm inversion was chosen as the preferred inversion from the analysis in section 5.4.2. These initial resistivity model tests indicated that a 1000 Ωm background was a good initial estimate of the background resistivity because it provided the lowest misfit between the forward modelled data and the observed data.

ZTEM Starting Model Test Inversions						
Frequencies	Data Points	Starting Model (Ωm)	Error %	Target Misfit	Final Misfit	Final/Target Misfit
360 – 30 Hz	6731	100	2.5	134620	163458	1.21
360 – 30 Hz	6731	500	2.5	80772	79588	0.99
360 – 30 Hz	6731	5000	2.5	134620	2003440	14.9

Table 5.4: Inversion parameters for the Morrison ZTEM starting model test inversions.

5.4.6 Preferred ZTEM Inversion Model

The final ZTEM inversion used a combination of parameters determined from preliminary inversions. Since there was no effect on the model or computational time when down-sampling the data, the inversion with half (6,731) of the ZTEM data was chosen to ensure there was an adequate amount of data to accurately determine the resistivity. The mesh was the same one used for the final MT and joint inversions (details in section 5.4.2) and the initial model was a 1000 Ωm halfspace. It should be emphasized that since ZTEM data do not give absolute resistivity values, the ideal starting background resistivity can only be determined from additional resistivity measurements.

Horizontal sections of the preferred ZTEM inversion model are shown in Figure 5.7. With an error of 2.5% applied to each tipper component, the inversion resulted in a final sum of squares misfit of 1.29×10^5 which is below the target of 1.35×10^5 . Although the geological interpretation will be discussed in detail in Chapter 7, it is important to note that several features in the resistivity model correspond with known geologic information. The conductive (low resistivity) zone to the southwest of the deposit (C1) corresponds with the predominant Quaternary glacial till, while the more resistive area to the northeast (R1) is due to the Hazelton Group volcanics and sediments. A shallow resistor (R2) correlates with the position of the intrusive Eocene Babine Suite and is interpreted as the central potassic zone. It is flanked to the northeast and southwest by a pair of shallow conductors that correlate with the bounding faults

of the Morrison Graben. In particular, the low resistivity to the northeast of the deposit (C2) could be due to pyrite and clay enrichment from argillic alteration observed at the East Fault (Liu, 2015). It is also likely that fluid pathways along the fault and conductive sulfide mineralization contribute to the low resistivity feature, but the relative contribution of each is indistinguishable without additional geological information. The maximum penetration depth of the ZTEM survey around the Morrison deposit appears to be about 1-1.5 km, which is consistent with a moderately conductive subsurface (about 250 Ωm using Eq. 2.12).

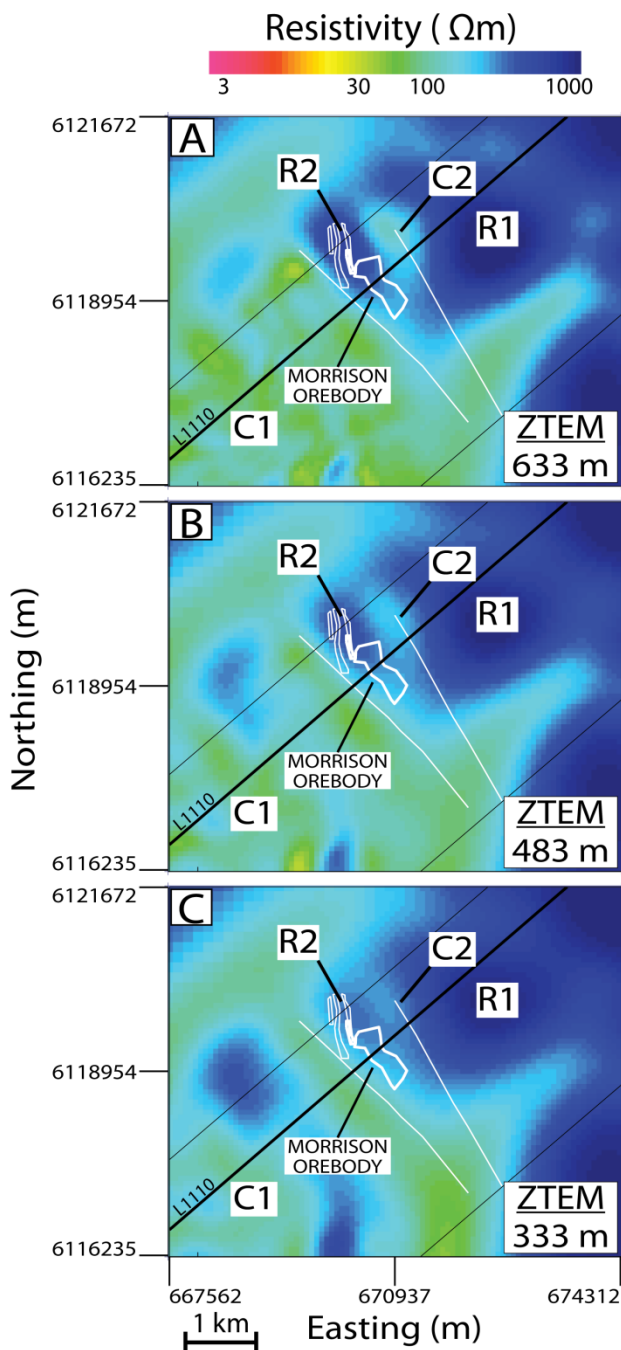


Figure 5.7: Horizontal slices of the preferred 3-D ZTEM inversion at three elevations above sea level: (A) 633 m elevation, (B) 484 m elevation, and (C) 333 m elevation. The Morrison deposit appears as a shallow resistive feature, and is bounded by conductors C1 and C2 that correlate with the edges of the Morrison Graben, as well as the pyrite enrichment zone.

5.5 MT Inversion

Data from the 33 MT stations collected in 2013 were inverted using the same octree mesh as the ZTEM data to allow for direct comparison between models. As previously stated, ZTEM data can only determine relative spatial variations in resistivity, because only magnetic fields are measured. In contrast MT apparent resistivity data curves can give constraints on the absolute value of subsurface resistivity and these can be used to guide the resistivity of the starting model in the ZTEM inversion. The MT impedance data were affected by distortions in the electric field, most likely caused by small-scale 3-D structure. Removing severely distorted MT stations was crucial to obtaining a reasonable inversion model. The final MT inversion model shows similar structure and resistivity values to the ZTEM inversion.

5.5.1 Parameters and Initial Model

The starting model for the first MT inversion was a 100 Ωm halfspace. This value was picked by qualitatively examining the MT apparent resistivity curves. Over half of the MT stations used in the inversion (20 out of 33) had apparent resistivity curves between 50 – 200 Ωm at the highest frequencies. An intermediate value of 100 Ωm was selected as the starting model to approximate this resistivity structure. The MT survey was conducted in the southwest half of the ZTEM survey area where Quaternary age sedimentary rocks are present, as opposed to the Jurassic Hazelton volcanics and sediments. This suggests that the MT inversion should have an overall lower apparent resistivity in the upper few kilometers with values between 10 – 500 Ωm common for sedimentary rocks.

Two inversions in Table 5.5 were run to test the initial model resistivity, one with a 1000 Ωm starting model (inversion B) and the other starting at 100 Ωm (inversion C). With all other

parameters the same, inversion C was able to reduce the data misfit to 4405, while inversion B reduced the misfit to 30684 (the target misfit was 2688). From this result the 100 Ωm halfspace was selected as the preferred starting model. However, the ZTEM preferred inversion used a 1000 Ωm starting model. This difference can be explained by the fact that the MT survey was predominantly deployed in Quaternary glaciolacustrine fill and the Morrison graben, so the measured apparent resistivity values were relatively low. In contrast the ZTEM survey extended about 5 km farther to the northeast over resistive mafic volcanics in the Lower Jurassic Hazelton Group. Further trials are required to determine if the same starting model can be used to invert both datasets.

In addition to the starting model, several other parameters were tested in subsequent inversions. These are listed in Table 5.5. While the lowest frequencies were included to provide more depth constraint than the ZTEM inversion, the inversion with frequencies as low as 0.176 Hz did not achieve a suitable final misfit. When the lowest frequency was raised to 0.7 Hz the inversion was able to achieve a better data misfit. Using 0.7 Hz still allows for deeper resolution than the lowest ZTEM frequency of 30 Hz.

Inversion	Frequencies (Hz)	Stations	Starting Model	Error	Target Misfit	Final Misfit	Final/Target Misfit
A	132 – 0.176	33	100 Ωm	1% max Z + 2.5%	4152	145997	35.2
B	132 – 0.7	28	1000 Ωm	10%	2688	30684	11.4
C	132 – 0.7	28	100 Ωm	10%	2688	4405	1.64
D	132 – 0.7	28	100 Ωm	Diagonal 20% Off-diagonal 10%	2688	2579	0.96
E	132 – 0.7	28	100 Ωm	Diagonal 15% Off-diagonal 7.5%	2688	5467	2.03
F	132 – 0.7	23	100 Ωm	Diagonal 20% Off-diagonal 10%	2208	1982	0.90

Table 5.5: Inversion parameters for several trial MT inversions. Diagonal and off-diagonal are the diagonal (Z_{xx} and Z_{yy}) and off-diagonal (Z_{xy} and Z_{yx}) terms in the impedance tensor.

5.5.2 Removal of MT Sites with Significant Distortion

As discussed in Chapter 4, the MT data showed a large degree of galvanic distortion at several stations. In inversion A, all 33 stations were used but the inversion was only able to decrease the misfit to 145997, while the target misfit was 4152 (Table 5.5). The small errors assigned to each component contributed to the large misfit, but the fit between observed and predicted MT data was especially poor at certain stations with galvanic distortion. The five most distorted stations (MR07, MR16, MR24, MR30, and MR33) had apparent resistivity values below 10 Ωm between the frequency range 132 – 0.7 Hz. This is one to two orders of magnitude lower than the rest of the stations. Inversion C was run with the five severely distorted stations excluded, and the misfit was reduced to 4405, which is much closer to the target of 2688. The misfit curves from the three inversions are shown in Figure 5.8. It is clear that removing these five stations from the inversion improves the overall misfit. One explanation for this is that the

75 x 75 x 75 m cell size was not small enough to accurately resolve the small, near-surface conductive bodies causing the galvanic distortion.

After removing the most severely distorted stations, an additional five stations (MR03, MR17, MR21, MR27, and MR36) were identified as galvanically distorted. Although not all of these stations displayed an obvious static shift, they either contained a large split in apparent resistivity (greater than one order of magnitude) or out-of-quadrant phases (not between 0 - 90°) between 132 – 0.7 Hz. The impedance phase represents the phase angle between the electric and magnetic fields, so a phase angle less than 0° or greater than 90° indicates that one of these fields has shifted in phase considerably. This type of distortion results from geometries that are difficult to model, so these stations were excluded from inversion F. Without the galvanically distorted stations, inversion F was able to achieve its target misfit while obtaining a reasonable resistivity model with the same features as the ZTEM model.

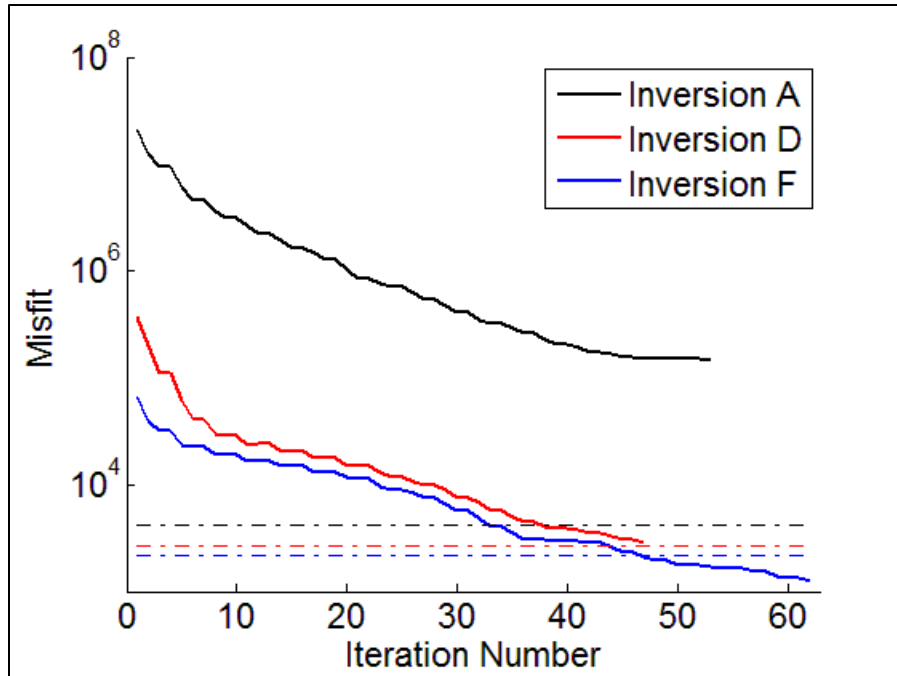


Figure 5.8: Comparison of inversion convergence curves for the MT inversions A (black line), D (red line) and F (blue line). Dashed lines represent the target misfit for each inversion. Inversions D and F excluded stations with severe galvanic distortion, and resulted in a much more acceptable final misfit.

5.5.3 Effect of Error Floor

Similar to the ZTEM inversions, the error floor has a large influence on how closely the inversion will fit the observed data. The error floor may be adjusted to vary for different impedance components. The diagonal components Z_{xx} and Z_{yy} for example are usually at least an order of magnitude smaller than the off-diagonal components Z_{xy} and Z_{yx} . A higher error floor may be applied to the diagonal components to account for noise. Another way to compensate for noise in the diagonal components is to apply a percentage of the maximum impedance component at a particular frequency plus a small error floor. In Table 5.5 inversion A uses 1% of the maximum impedance plus 2.5% of the individual datum. This ensures that a large enough error floor is applied to the diagonal components.

In inversions D - F the diagonal component errors were twice as large as the off-diagonal component errors. Since inversion D was able to reduce the misfit below the target amount, inversion E was run with a smaller error floor to see if more closely fitting the data would change the model. The same resistivity features are present in the models for inversions D and E even when the error floor is varied. This suggests that lowering the error floor does not introduce more subtle structure into the resistivity model, so the 10% error on off-diagonal components and 20% on diagonal components used in inversion D and F is an appropriate choice.

5.5.4 Preferred MT Inversion Model

Inversion F was chosen as the preferred model because it did not include the obviously distorted stations, converged to the target misfit, and contained the same resistivity features as the individual ZTEM inversion. There is good agreement between the observed data and the predicted model response at the stations shown in Figure 5.9. Here the four components of apparent resistivity and phase are plotted for three selected stations. Even the diagonal components (xx and yy), which tend to be noisier than the off-diagonal components, are well fit at most frequencies. There is generally a low misfit at high frequencies for all stations, but the misfit increases for frequencies below 1 Hz.

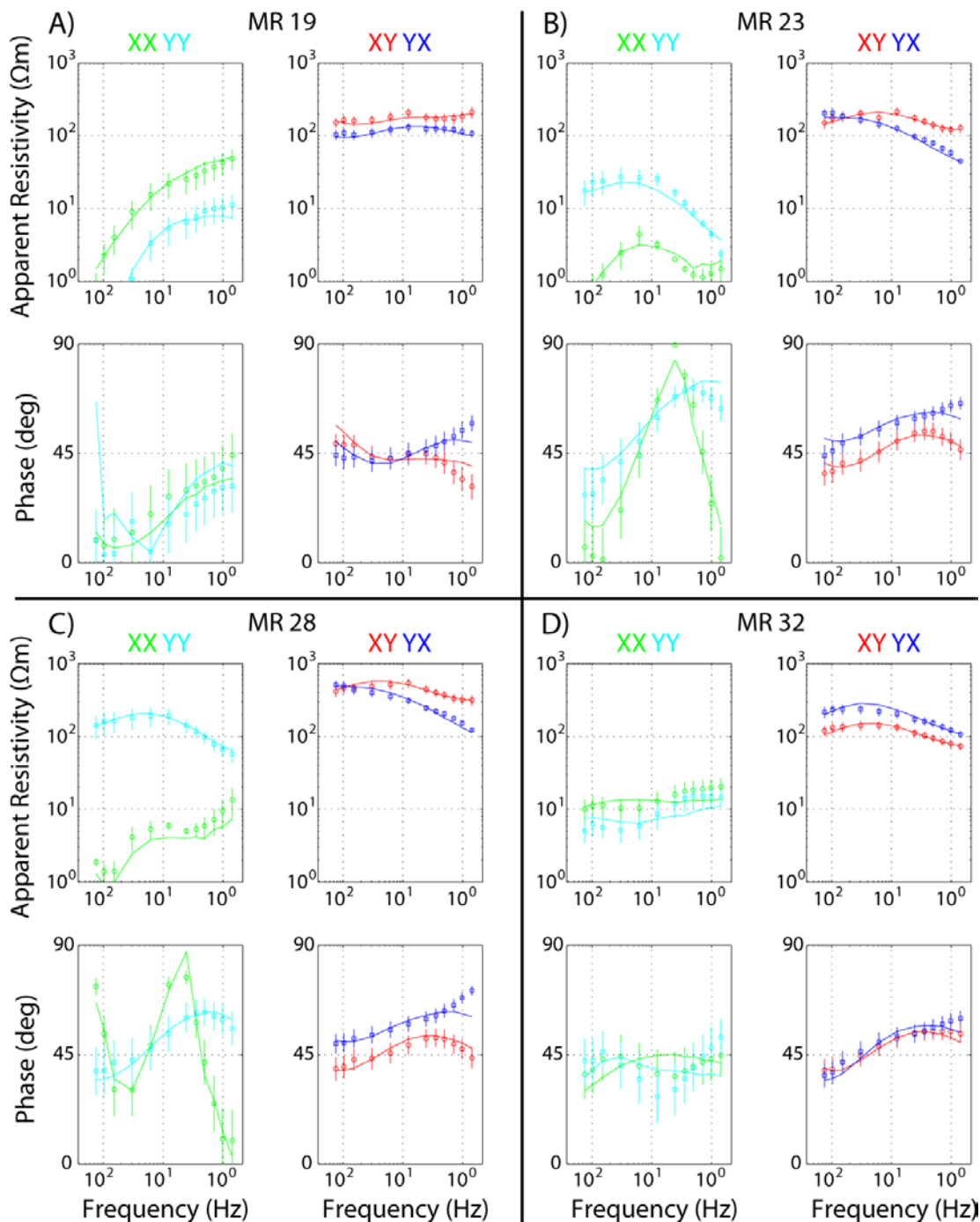


Figure 5.9: Selected plots of observed and predicted data for MT inversion F at MT stations (A) MR19, (B) MR23, (C) MR28, and (D) MR32. The four components of apparent resistivity and phase (xx , xy , yx , and yy) derived from the MT impedance tensor are shown for each station. Dots are the observed data and lines are the predicted model response. The predicted data match the observed data very closely. The inversion converged to a misfit of 1982 (target 2208).

Figure 5.10 shows horizontal slices through MT inversion F at elevations of 633, 483, and 333 m above sea level. In the first panel, 633 m elevation corresponds to a depth 100-200 m above the Morrison deposit. There is a broadly conductive area in the southwest quadrant of the survey area (C1) that is coincident with the Quaternary sedimentary cover. However, the station spacing is large in this area so the low resistivity ($< 20 \Omega\text{m}$) regions between stations are likely poorly constrained. The resistivity structure becomes more varied around the Morrison Graben to the northeast. In particular there are low resistivity features that correspond with the bounds of the graben structure, as these are probably conduits for fluids and hence have low electrical resistivity. The conductor C2 appears in the ZTEM inversion as well and is likely correlated with the pyrite enrichment zone or improved pore and fracture connectivity along the east side of the graben. To the east of the graben there is a highly resistive area (R1) that is consistent with the Hazelton Group volcanic rocks. Directly over the deposit (outlined in white) the resistivity varies over the main BFP stock, with a lower resistivity associated with the southeast portion. The northwest portion of the stock, including the thin, northward trending BFP dikes show a higher resistivity anomaly (R2) that extends to the 483 m slice (middle panel). At this depth there is a clearly resistive structure ($> 1000 \Omega\text{m}$) that correlates well with the main intrusive body and potassic alteration zone of the deposit. This seems to indicate a deeper intrusive stock below the argillic altered rocks observed above by Mitchinson et al. (2013).

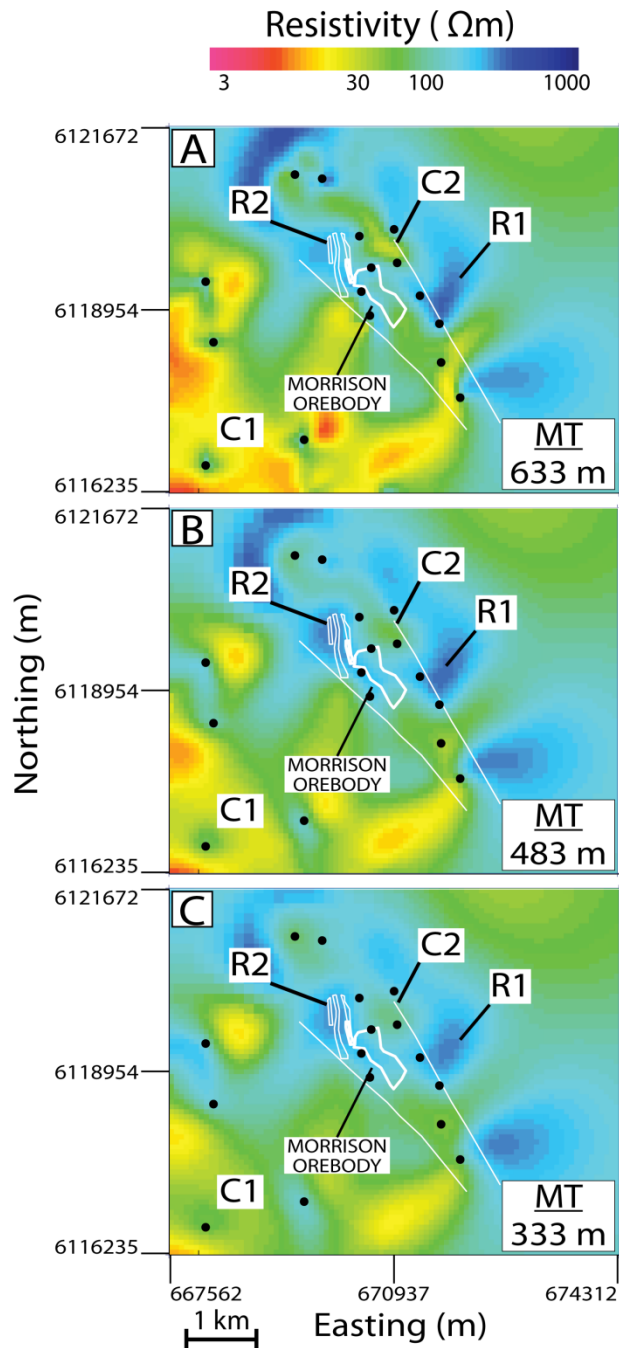


Figure 5.10: Horizontal slices of the 3-D MT inversion F at (A) 633 m, (B) 483 m, and (C) 333 m elevation above sea level. The Morrison deposit and geologic features are overlain in white, and MT stations are the black circles. The resistivity features C1, C2, R1, and R2 appear in the ZTEM-only inversion as well (see Chapters 5 and 7 for interpretation).

5.6 Summary

After ensuring that the ZTEM and MT datasets were in a consistent reference frame and had a common sign convention, the two datasets were inverted separately using the same discretization mesh. The ZTEM data were inverted at five frequencies between 360 and 30 Hz, while the MT inversion was performed with impedance data from twelve frequencies between 132 and 0.7 Hz. Although the MT inversion used impedance data from ground measurements of the electric and magnetic fields and the ZTEM inversion used tipper data derived from airborne and ground magnetic field measurements, the inversions contained the same resistivity features discussed below.

Figure 5.11 shows vertical sections of the preferred ZTEM and MT inversion models on flight line L1110. There are several resistivity features that are present in both models. Quaternary glaciolacustrine fill to the southwest of the deposit (C1) is a shallow conductive feature, while mafic volcanics from the Hazelton Group appear highly resistive to the northeast (R1). The Morrison deposit appears as an outcropping resistive body (R2) that extends to approximately 500 m below the surface. The deposit is flanked to the southwest and northeast (C2) by two conductive bodies that correlate with the bounding faults of the Morrison Graben. The resistivity contrast between the deposit and faults is stronger in the MT inversion, likely due to resistivity information provided by the impedance data. The ZTEM model seems to lose resolution below about -1000 m elevation, as the resistivity values are equal to the starting model (1000 Ωm). While the MT model contains features below this elevation, the large conductive body is likely not a well-constrained feature as the lower frequency MT data was not fit as well as the higher frequency data.

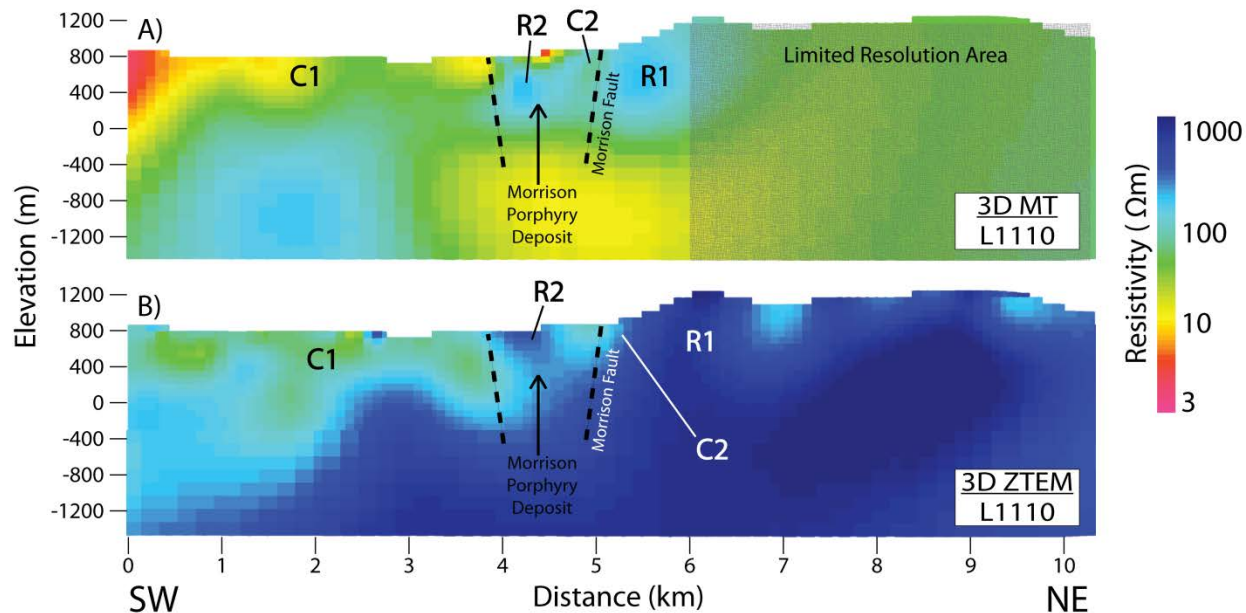


Figure 5.11: Vertical sections through flight line L1110 of the (A) MT inversion model and (B) ZTEM model. Both inversion models contain a shallow, conductive overburden to the west of the deposit (C1). The Morrison deposit contains an outcropping resistive body (R2) that extends to about 500 m below the surface and is flanked to the southwest and northeast (C2) by two conductive features. Hazelton Group volcanics and sediments appear resistive to the northeast (R1). The MT model contains a large conductor below the deposit while the ZTEM model contains a large resistor. Since the MT data misfit was high at lower frequencies, this is likely not a well-constrained feature. The northeastern portion of the MT section is not well resolved because no stations were located in this area.

Figure 5.12 shows depth slices of the MT and ZTEM inversions at 633 m, 483 m, and 333 m elevation above sea level. Both MT and ZTEM inversions show the shallow conductive Quaternary glacial overburden (C1) to the southwest of the deposit. The ZTEM inversion resolves the resistive Hazelton Group volcanics and sediments (R1) to the northeast of the deposit, while the MT model does not show this feature to the same extent because of the spatially limited station coverage. The resistive feature R2 appears in both models and is associated with the intrusive dikes to the northwest of the deposit as well as the northwestern half of the bisected BFP stock. C2 is a conductive feature that correlates with the eastern edge of the

Morrison Graben, but may also be due to conductive disseminated or interconnected sulfides at the periphery of the deposit.

Crossplots of the individual ZTEM and MT inversions (Figure 5.13) show that there is a correlation between the resistivity values in each model. Panels A – D show the correlation at lower elevations (deeper horizontal sections). The resistivity value for each individual model cell was plotted (x-axis is MT model resistivities, y-axis is the ZTEM model resistivities). If the resistivity values in both models were exactly the same, the plot would be a direct one-to-one relationship. In panels A and B there is a direct relationship between the resistivity values, but the trend appears to be above the one-to-one line. This is because the ZTEM inversion had a 1000 Ωm starting model compared to 100 Ωm for the MT inversion. In panels C and D the correlation appears weaker, presumably because the higher frequency ZTEM inversion loses resolution at shallower depths than the MT inversion. Further comparison and interpretation of the two inversion models will be discussed in Chapter 7.

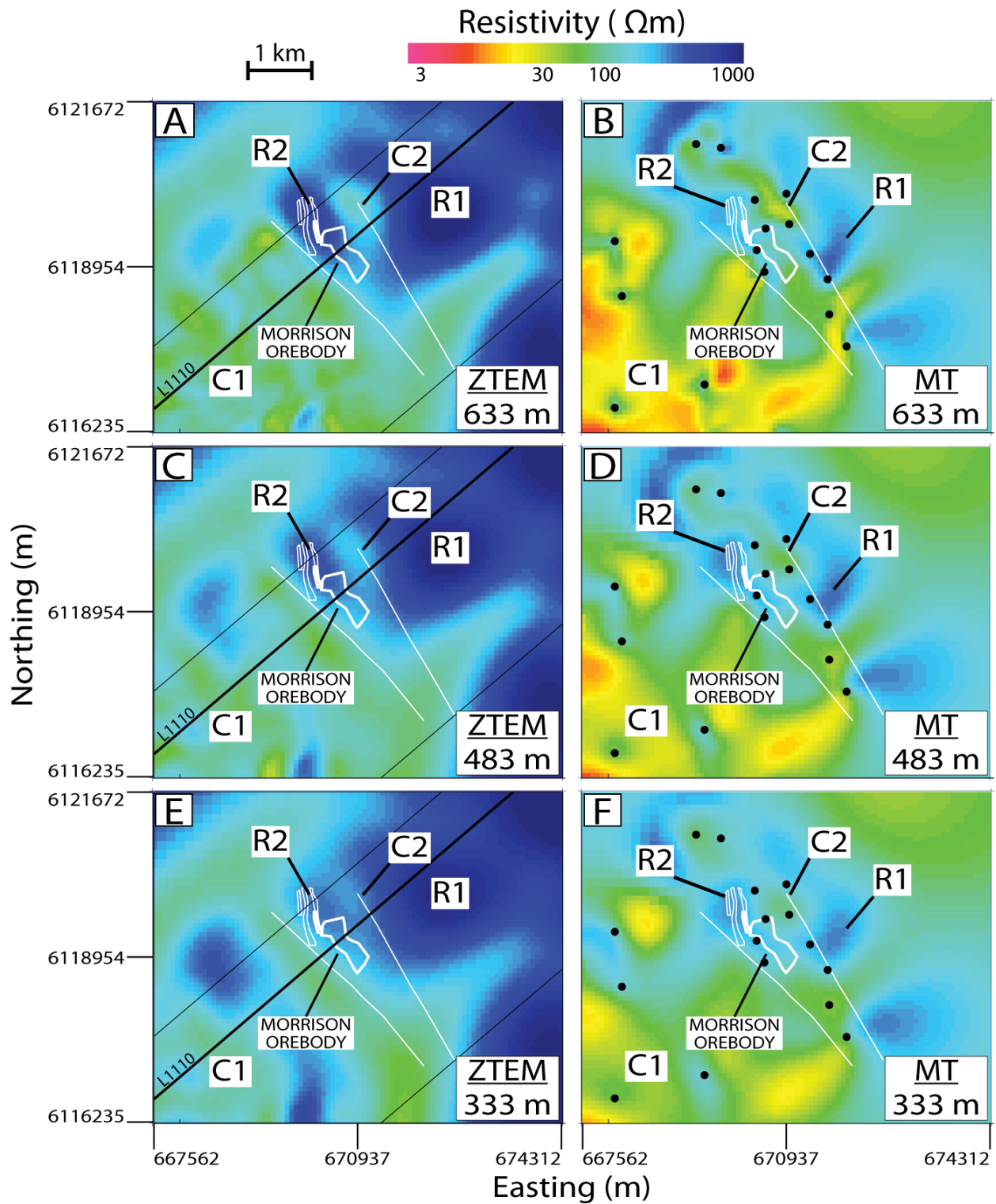


Figure 5.12: Horizontal slices through the ZTEM and MT inversions at three elevations above sea level: 633 m elevation (A and B), 483 m elevation (C and D), and 333 m elevation (E and F). The same resistivity features present in both ZTEM and MT models are described in section 5.6.

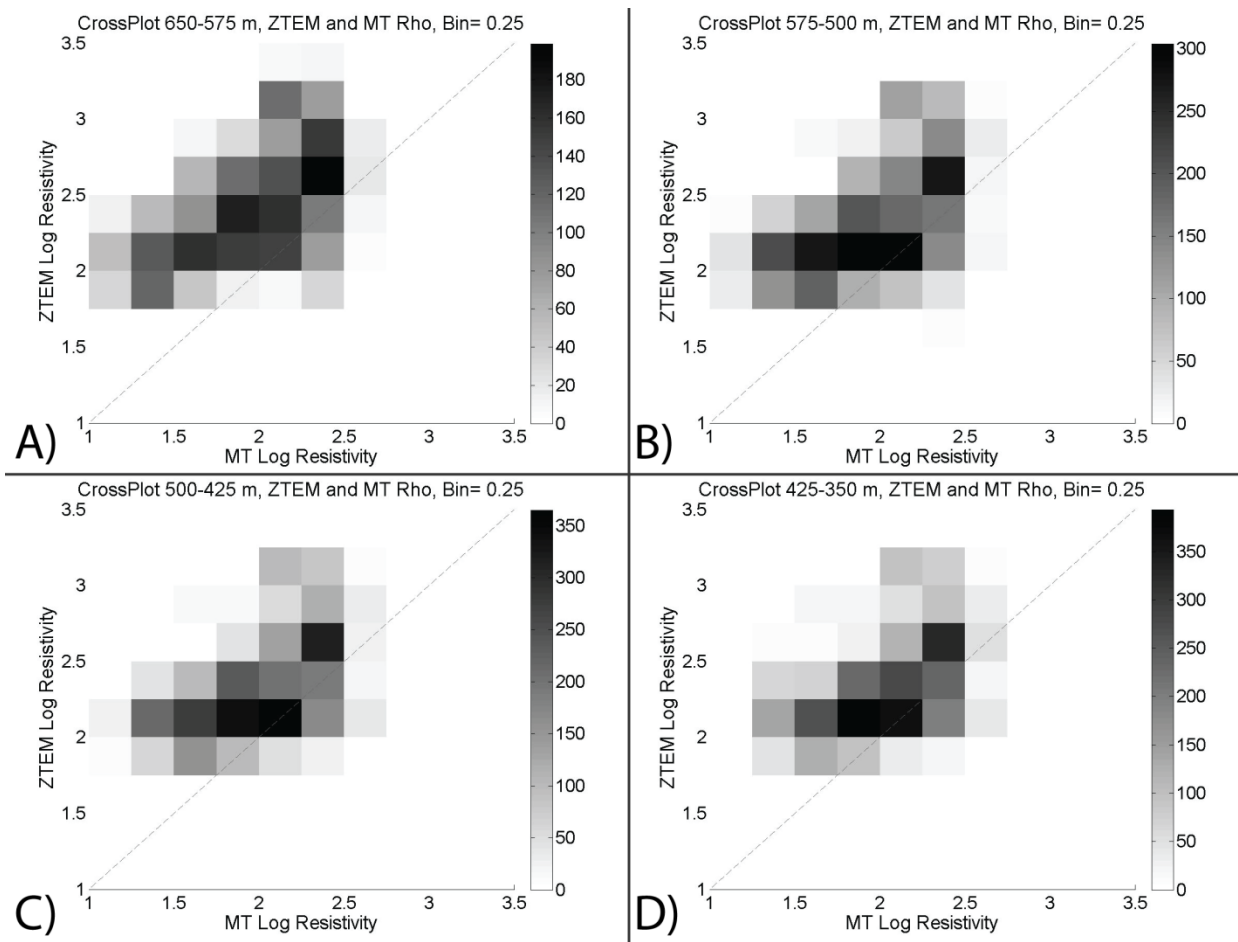


Figure 5.13: Correlation plots for the preferred ZTEM and MT inversions. Using the same mesh, the resistivity of each cell from the ZTEM and MT inversions was plotted at four depths. Darker squares correspond with more occurrences within a specific bin. The dashed grey line is a one-to-one correlation. The correlation appears nearly one-to-one in panels A and B, but is slightly offset because of the different starting models used for each inversion. In panels C and D the correlation is not as clear because the ZTEM inversion begins to lose resolution at these depths.

Chapter 6: Joint Inversion of the Morrison MT and ZTEM Data

6.1 Introduction

Correct interpretation in geophysical exploration always benefits from integrating multiple geophysical techniques and using all the available geoscientific information. Various EM methods share a similar theoretical background and may be inverted together to reduce the non-uniqueness that is inherently part of the inverse problem (Vozoff and Jupp, 1975). For example, a combination of marine controlled source EM (CSEM) and MT has been explored to improve resolution for offshore hydrocarbon mapping (Mackie et al., 2007; Commer and Newman, 2009). Synthetic examples from these authors showed that the sensitivity of CSEM to thin, resistive targets and the depth resolution of MT could together constrain inversions of the resistivity structure of a hydrocarbon reservoir. Methods sensitive to different earth properties such as seismic exploration are also invaluable in interpretation. For example, a case study by MacGregor et al. (2006) showed that combining seismic and well-log data with a CSEM inversion would improve resolution of the lateral extent of a hydrocarbon reservoir. A similar approach can be used in mineral exploration, where the natural source ZTEM and MT methods can be used to determine electrical resistivity to greater depths than controlled source methods alone. The airborne ZTEM method measures the vertical and horizontal magnetic field components in the frequency range 360 – 30 Hz and can resolve features at a depth of a few kilometers in moderately resistive environments. However, ZTEM data alone are unable to resolve 1-D resistivity structure since these resistivity models do not generate vertical magnetic

fields. MT surveys measure electric and magnetic fields at lower frequencies (up to 0.001 Hz for broadband systems) to obtain an estimate of absolute resistivity at much greater depths than ZTEM. However, MT surveys are more costly to deploy with a dense station layout over the region of interest. A solution is to simultaneously invert ZTEM and MT data (Holtham, 2012; Sasaki et al., 2014; Wannamaker and Legault, 2014; Sattel and Witherly, 2015) to take advantage of the spatial coverage of the ZTEM method and the depth resolution of the MT method. Joint inversion of ZTEM and MT data from the Morrison deposit is investigated in this chapter to determine if the combination of multiple EM methods would yield an improved resistivity model compared to the inversion of each dataset on its own.

6.2 Methodology

The inversion algorithm used for the joint inversions is the same as that used in Chapter 5 for the separate inversions of the ZTEM and MT data. However the data misfit term must be modified to accommodate both data sets. The objective function Φ is still dependent on the data misfit and model regularization:

$$\Phi = \phi_d + \beta \phi_m \quad (6.1)$$

where β is the regularization term, ϕ_m is the measure of model structure, and ϕ_d is the sum of the MT and ZTEM data misfits, ϕ_d^{MT} and ϕ_d^{ZTEM} . These are defined as in Chapter 5:

$$\phi_m = \sum_{k=1}^4 \alpha_k \|\mathbf{W}_k(\mathbf{m} - \mathbf{m}^{ref})\|_2^2 \quad (6.2)$$

$$\phi_d^{ZTEM} = \mathbf{W}_{d1}(\mathbf{d}_{ZTEM}^{obs} - \mathbf{d}_{ZTEM}^{pred})\|_2^2 \quad (6.3)$$

$$\phi_d^{MT} = \mathbf{W}_{d2}(\mathbf{d}_{MT}^{obs} - \mathbf{d}_{MT}^{pred})\|_2^2 \quad (6.4)$$

where \mathbf{W}_1 is a diagonal matrix, \mathbf{W}_2 , \mathbf{W}_3 , and \mathbf{W}_4 are the first order finite-difference matrices for the x , y , and z directions, and the α 's are adjustable parameters that control the closeness to the reference model (α_1) and the amount of spatial smoothing in the x , y , and z directions ($\alpha_{x,y,z}$). The vectors \mathbf{m} and \mathbf{m}^{ref} contain the cell resistivities of the recovered and reference model respectively. Equations 6.3 and 6.4 are the sum of squares data misfit between the observed and predicted ZTEM and MT data. \mathbf{W}_{d1} and \mathbf{W}_{d2} are diagonal matrices containing the reciprocals of the data uncertainties, \mathbf{d}^{obs} is the observed data, and \mathbf{d}^{pred} is the data predicted by the model.

In most cases the number of data points in the ZTEM survey will be much greater than the number of data points from the MT survey. For example an MT survey with 20 stations recording the full impedance tensor (8 components) at 10 frequencies will have 1,600 total data points. A similar scale ZTEM survey with fifteen 10 km flight lines measuring approximately every 10 m will have 300,000 data points (4 tipper components at 5 frequencies). Without compensating for over one hundred times as many ZTEM data points as MT data points the inversion misfit in this example will be dominated by the ZTEM data. Even if the inversion reaches the desired sum of squares misfit, the resulting resistivity model may contain mostly shallow structure required by the higher frequency ZTEM data. The data misfit terms for ZTEM and MT must be balanced so that they equally influence the overall data misfit function. Following the method of Holtham (2012), the total data misfit ϕ_d is weighted by the term γ :

$$\phi_d = \|\mathbf{W}_{d1}(\mathbf{d}_{ZTEM}^{obs} - \mathbf{d}_{ZTEM}^{pred})\|_2^2 + \gamma \|\mathbf{W}_{d2}(\mathbf{d}_{MT}^{obs} - \mathbf{d}_{MT}^{pred})\|_2^2 \quad (6.5)$$

where \mathbf{W}_{d1} and \mathbf{W}_{d2} are diagonal matrices whose elements are the reciprocals of the ZTEM and MT data uncertainties, respectively. The vector \mathbf{d}^{obs} is the observed data and \mathbf{d}^{pred} is the model predicted data. For n data points, the data vectors will have the form:

$$\mathbf{d} = \begin{bmatrix} d_1 \\ \vdots \\ d_n \end{bmatrix} \quad (6.6)$$

The data uncertainties were first determined by individually inverting each dataset in Chapter 5. The parameter γ from Equation 6.5 is directly related to the uncertainties of the MT data. This means γ can be changed by appropriately scaling the MT data errors in the inversion. In order for both datasets to equally influence the inversion, γ should be approximately equal to the number of ZTEM data, N_{ZTEM} , divided by the number of MT data, N_{MT} , i.e.

$$\gamma = N_{ZTEM}/N_{MT} \quad (6.7)$$

This effectively increases the weight of the MT data misfit in the misfit function by forcing the inversion to more closely fit the few MT data points. The optimal γ value must be determined through trial inversions. The γ parameter for joint ZTEM-MT inversion was introduced by Holtham (2012) but not formally implemented in the inversion algorithm used in this study. Section 6.4 describes the method that was used to vary the relative weighting of the ZTEM and MT datasets in the joint inversion.

6.3 Synthetic Joint Inversion Example

A synthetic inversion was run to test the effect of jointly inverting ZTEM and MT data. In particular the ability of the MT data to provide depth resolution was studied. The same synthetic porphyry model from Chapter 2 (Figure 6.1) was used. The model consists of a 1 km x 1 km 1000 Ωm core that extends from the surface to 2 km depth. The resistive core is surrounded by a low resistivity 10 Ωm ring, and both features are embedded in a 100 Ωm background. ZTEM tipper data were in the range 30 – 720 Hz at 962 locations above the porphyry (Figure

6.1) and the lower frequency MT impedance data from 64 stations were in the range 300 – 0.5 Hz.

Figure 6.2 shows the resistivity model obtained from joint inversion of ZTEM and MT data over the synthetic porphyry model. In the map view the inversion resolves the resistivity boundaries at the surface and recovers the resistivity magnitudes well. In the vertical section the lateral contrasts are well-defined but the vertical resolution is not much improved from the synthetic ZTEM inversion in Chapter 2 (Figure 2.12). The joint inversion smears the conductive bodies together below the resistive core, similar to the MT-only synthetic inversion (Figure 2.13). This is an artifact of the inversion as the low resistivity ring is not connected in the synthetic porphyry model. Although this deep structure is required by the MT data, the joint inversion does not match the resistivity value of the deep conductor in the MT-only inversion. This means the joint inversion is not fully fitting the MT data and additional reweighting is required. Despite this, it is clear that the joint inversion is incorporating structure required by both the ZTEM and MT datasets. The next step is to determine the proper weighting for the ZTEM and MT datasets from the Morrison study area.

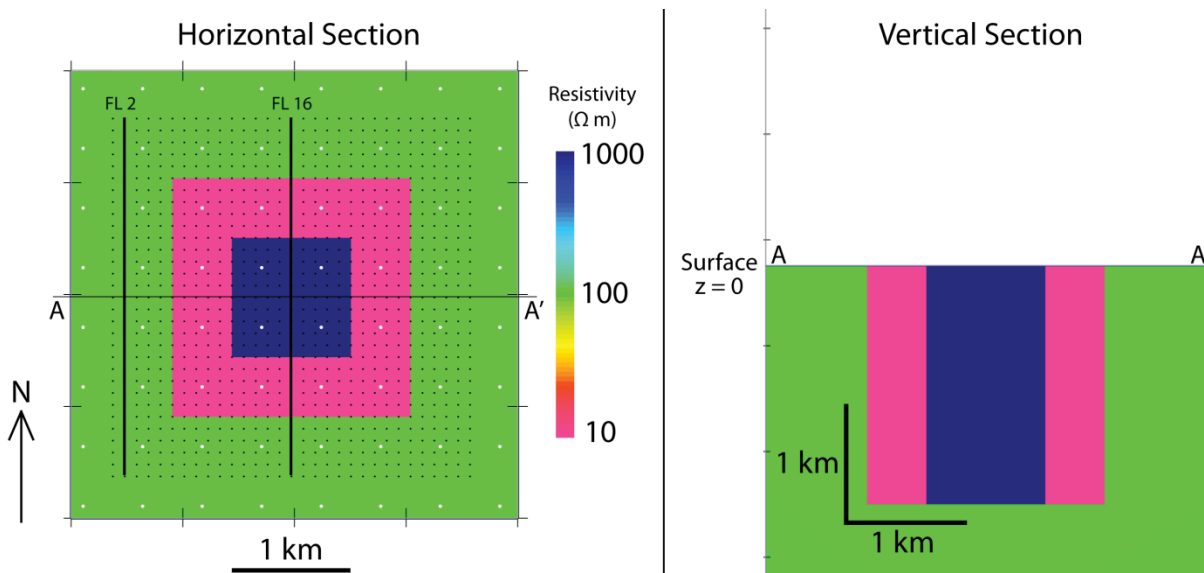


Figure 6.1: Plan view (left) and vertical section (right) of the synthetic porphyry model. The core is a 1 x 1 km wide, 1000 Ωm resistor, surrounded by a 2 x 2 km wide 10 Ωm conductor. These two features extend to 2 km depth and are embedded in a 100 Ωm halfspace. In plan view the black dots represent ZTEM observation points, grey lines are the ZTEM flight lines (FL2 and FL 16), and sparse white dots are MT station locations.

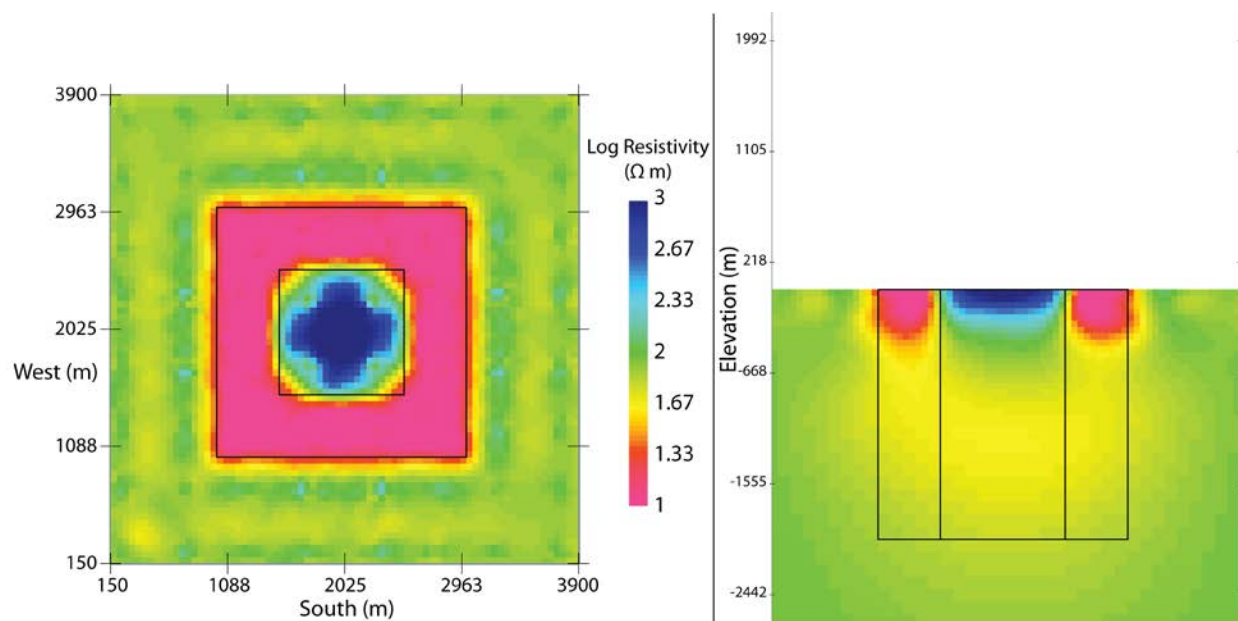


Figure 6.2: Joint inversion model of the ZTEM and MT data over the synthetic porphyry model (Figure 6.1). The left panel shows a map view at the surface (0 m) and the right shows a vertical section through 2000 m West. Black lines are the outlines of the original synthetic porphyry model. The joint inversion defines the resistivity boundaries well and has more resolution at depth compared to the ZTEM-only synthetic inversion in Chapter 2 (Figure 2.12).

6.4 Joint Inversion of the Morrison Data

The ZTEM and MT data collected at the Morrison deposit were first inverted individually to assess the resolution of each technique (see Chapter 5). When suitable individual inversions were obtained, the data were jointly inverted using the UBC e3dMTinv iterative solver. This is possible because the forward modeling in the inversion process is the same for each dataset. To allow for direct comparison, the joint inversion used the same mesh as the single ZTEM and MT inversions with 75 x 75 x 75 m cells in the core region as described in Chapter 5. The initial resistivity model was set to 1000 Ωm , as determined by forward modeling tests in Chapter 5. For the joint inversion the same ZTEM data at five frequencies between 360 and 30 Hz were used, and MT data at 16 frequencies between 132 and 0.176 Hz were used. This allowed for an overlap of two frequency decades and for lower frequency data from the MT to constrain deeper structure. The ZTEM data uncertainties were assigned as 2.5% of the data value. Several joint inversions were run to test the optimal weighting and thus the uncertainties assigned to the MT data. This procedure allowed the MT data to gradually influence the final inversion result. Each inversion was then evaluated based on misfit and model structure, as seen in Figure 6.3.

6.4.1 Joint Inversion Results

Figure 6.3 shows horizontal slices through each joint inversion model at an elevation of 483 m. In each progressive slice the MT data error (a percent of the data value) decreases, thereby increasing the weight of the MT data on the inversion. The bounding faults of the Morrison Graben are overlain along with the main ore body associated with the BFP stock and dikes. The diagonal line is ZTEM flight line L1110, which is used for the vertical sections shown in Figure 6.4.

Chapter 6: Joint Inversion of the Morrison MT and ZTEM Data

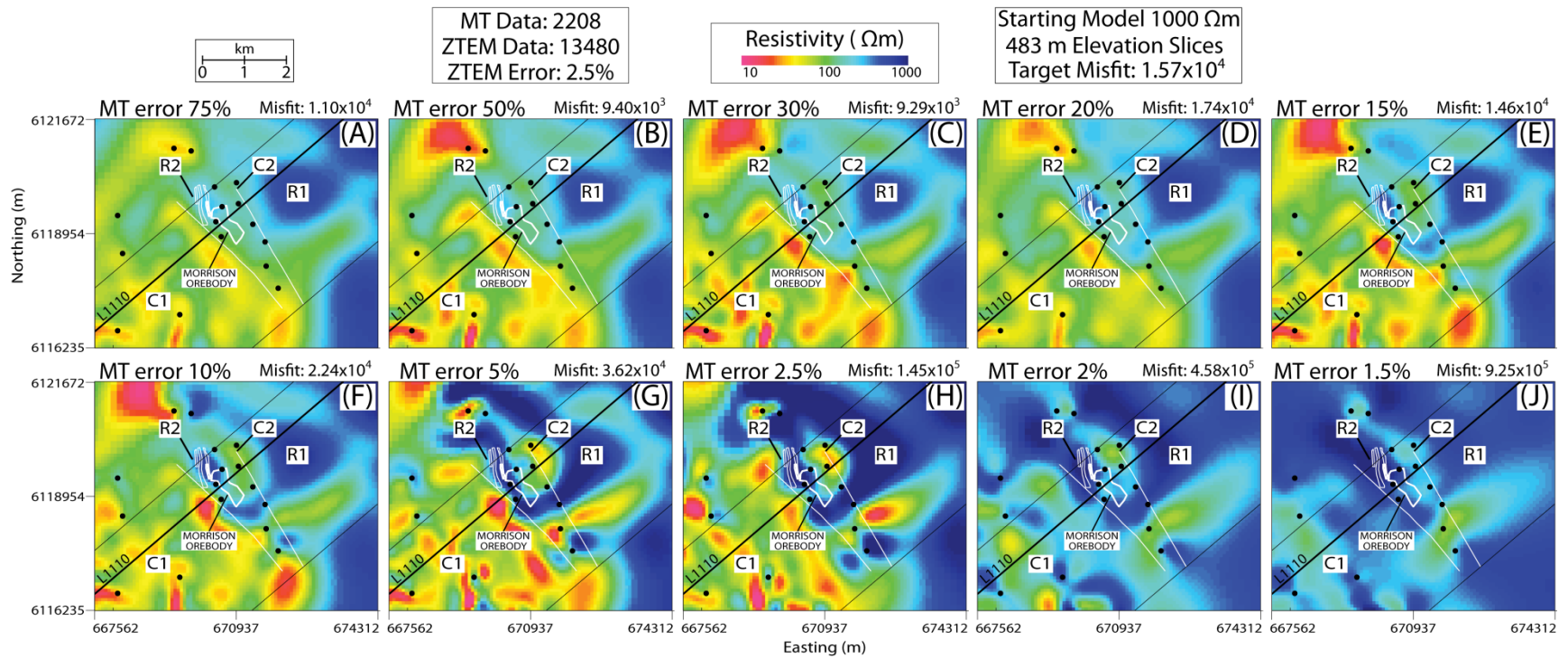


Figure 6.3: Horizontal slices at 483 m elevation through joint ZTEM-MT inversion models with various MT data weights. The diagonal thick black line represents flight line L1110. The main BFP stock and dikes are overlain in white, along with the bounding faults of the Morrison Graben. Black circles are MT stations and thin black lines are the extent of the ZTEM survey. As the MT data error is decreased, the relative weighting of the MT data in the inversion is increased. In panels A-H it is clear that the inversion is incorporating information about absolute resistivity values from the MT data. The inversions in panels I and J were not able to fit the ZTEM and MT data, and do not contain the same features as the other inversions.

The horizontal sections show that the MT data gradually influence the joint inversion as the weighting is increased. Figure 6.3 (panel A) shows the inversion model obtained from an inversion using MT data with errors assigned as 75% of the data values. Compared to the ZTEM-only inversion obtained in Chapter 5, it is clear that introducing MT data with very large uncertainties into the joint inversion has a minimal effect on the final inversion model. The features C1, C2, R1, and R2 are resolved in the same locations as the ZTEM-only inversion in Figure 5.7 panel B. The inversion is easily able to fit the MT data because large errors remove requirements on model resistivity structures. On the other hand, the ZTEM data use 2.5% error as in Chapter 5, so the inversion preferentially creates resistivity features to fit the ZTEM data. The model does not change significantly to the northeast of the Morrison Graben since there are no MT stations in that area so the resistivity structure should not be greatly changed when MT data are introduced throughout the joint inversions.

As the MT error is lowered further (Figure 6.3 B-E) the inversion models begin to change significantly from the model shown in panel A. Most noticeably the conductive feature C1 to the southwest of the Morrison Graben decreases in resistivity as the MT data weighting increases. These features correlate well with MT station locations but appear localized likely because of the irregular MT station spacing away from the deposit. To the northwest of the ore body the resistive feature R2 increases in resistivity and the conductor C2 decreases in resistivity from Panels C to E. The MT stations seem to be changing the magnitude of the resistivity values compared to the tipper-only ZTEM inversion. While the ZTEM-only inversion delineates resistivity contrasts well, the addition of MT data appears to influence the actual resistivity of these features.

Chapter 6: Joint Inversion of the Morrison MT and ZTEM Data

In Panel F (Figure 6.3) the 10% MT error is the closest to the error used in the preferred MT inversion (Chapter 5). This is the preferred joint inversion model because the data misfit increases greatly in panels G-J and these models do not appear to be discretely resolving features C1, C2, R1, and R2. The higher resistivity values associated with R2 is a consistent feature as in previous Figure 6.3 panels. The resistivity of this feature increases sharply in panel F when the MT error is set to 10% of the data. To the southeast of the main BFP stock there is a strongly resistive body that spans the width of the Morrison Graben. This area is slightly more resistive than its surroundings in the ZTEM-only inversion but seems to increase in resistivity as the MT data weighting is gradually increased. In panels E and F this feature becomes much more prominent.

Figure 6.3 (G-J) are the inversions performed with MT error in the range 5 – 1.5 %. While the previous models (A-F) gradually changed with decreasing MT error floor, these models vary significantly because the inversion is no longer able to fit the MT data closely. The inversion in Panel G images the four features C1, C2, R1, and R2, but features such as R1 and R2 are spatially connected. This is not observed in the individual ZTEM and MT inversions. However, the inversion in Panel G (Figure 6.4) is the only one to place a highly conductive body directly below the Morrison deposit as seen in the individual MT inversion (Figure 5.11 panel A). The optimal weighting appears to be between an MT error of 5 – 10% (Panels F and G) since the inversion in panel F reproduces all the resistivity features of the individual ZTEM and MT inversions, while the inversion in panel G incorporates the most structure at depth from the lower frequency MT data. However, the final misfits of the inversions in panels G-J are much higher than the target misfit of 1.57×10^4 . It is especially clear in panels I and J that the inversion is not significantly changing the model from the original 1000 Ωm starting model. At these small MT error floors the inversion is not able to simultaneously fit the ZTEM and MT data.

Figure 6.4 shows the vertical inversion sections through flight line L1110. Like Figure 6.3, the inversions are ordered to show the effect of gradually increasing the MT data weight in the joint inversion. In panels C-E the resistivity structure begins to change in the western portion of the profile as the MT data are being introduced into the joint inversion. The resistivity of the shallow conductive feature (C1) decreases sharply in panels C-G. While this may more closely resemble the true resistivity than in panel A, the features are not laterally smooth. This may be due to the large distance between MT stations away from the deposit. A more realistic model would have a smoothly varying resistivity structure and could be achieved by varying the inversion smoothing parameters. Another prominent feature of the joint inversions in panels C-G (Figure 6.4) is the shallow resistive body (R2) corresponding with the deposit location. Compared to panel A, the resistive feature has a much higher resistivity ($> 1000 \Omega\text{m}$) than its surroundings. The conductive features bounding the deposit are still largely present in Panels C-G, and correlate well with the bounding faults of the Morrison Graben. The eastern part of the model does not change as the MT data errors are varied. This is because due to logistical reasons, no MT data were collected there.

As the inversion uses an MT error below 10% it becomes clear that the inversion is unable to fit the ZTEM and MT data simultaneously, and the resistivity model contains spurious features in panels G-H. As previously mentioned, the inversion in panel G (Figure 6.4) contains the most similar deep structure to the MT-only inversion, suggesting that the 5% data error is close to the optimal MT weighting. The inversion does not change the model appreciably from the starting $1000 \Omega\text{m}$ halfspace in panels I – J and the data misfit is much higher than the target misfit.

Chapter 6: Joint Inversion of the Morrison MT and ZTEM Data

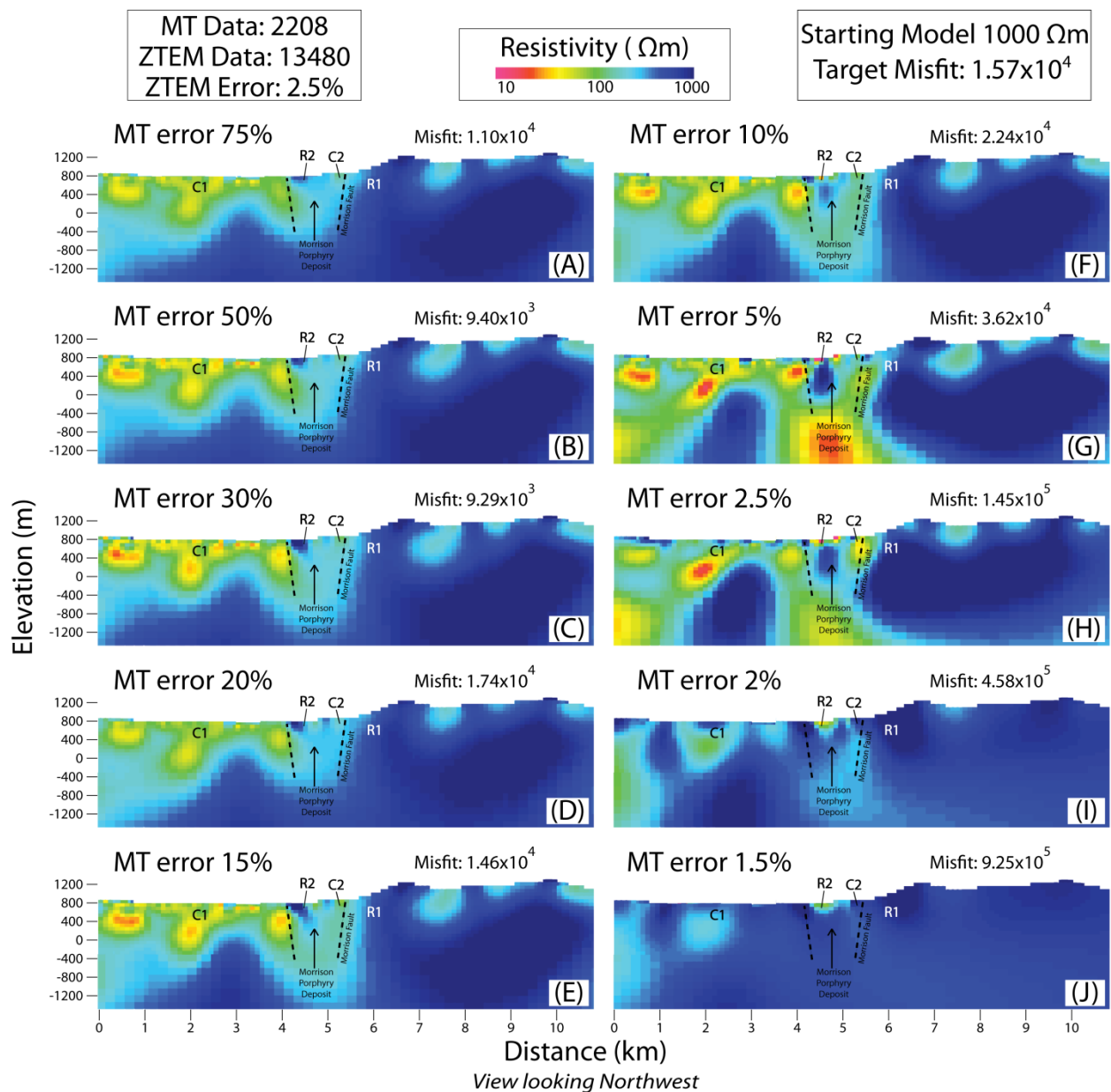


Figure 6.4: Vertical slices through joint inversion models with various MT data weights. As the MT error is decreased, the relative weighting of the MT data increases in the joint inversion and features required by the MT data should be replicated in the resistivity model. The inversions in panels F – H appear to be including the most structure from the MT data as there are features below the resolution of the higher frequency ZTEM data. In panels I – J the inversion is not able to closely fit either dataset, and the model does not change appreciably from the starting 1000 Ωm . Resistivity features are labelled as C1, C2, R1, and R2 (see text for interpretation).

6.5 Summary

Ten inversion models were presented that represent a gradually increasing weight of MT data in the joint ZTEM-MT inversion. The weighting of the MT data in the joint inversions was increased by decreasing the error estimates of the MT data, forcing the inversion to more closely fit the MT data. While the joint inversion with MT errors set to 75% of the data closely resembled the ZTEM-only inversion, decreasing the MT data gradually to 50 – 1.5% of the data increased the influence of the MT data on the inversion model.

The joint inversions showed prominent resistivity features associated with the Morrison deposit. The resistive feature R2 associated with the northwest half of the BFP stock and dikes was a consistent feature in all inversions. This feature had a higher resistivity in the MT-only inversion and expectedly became more pronounced in the joint inversion with the highest MT data weight. The conductive feature C2 similarly became more conductive as the MT error floor was lowered. This suggests that the ZTEM inversion produced a model with the correct relative resistivity contrasts, and the addition of the MT data provided constraint on the absolute resistivities of these features. Decreasing the MT error floor below 5% and below resulted in inversions with higher misfits and variable models. The inversion appears to have difficulty fitting the MT data below this threshold, as 10% error was also used for the preferred MT inversion in Chapter 5. One promising result was the large conductor at depth in the inversions shown in panels F – H (Figure 6.4). These inversions most clearly contained this structure seen in the individual MT inversion from Chapter 5. This suggests that the inversion is able to include structure required by the lower frequency MT data while still imaging the shallow structure required by the higher frequency ZTEM data. Chapter 7 will provide interpretations for the features observed in the inversion models from additional geologic and geophysical information.

Chapter 7: Interpretation

7.1 Introduction

Chapters 5 and 6 described the results of the individual and joint ZTEM-MT inversions for the Morrison deposit. The higher frequency and dense spatial sampling of the ZTEM data means that the ZTEM inversion gives good resolution of the shallow resistivity structure with a fine horizontal resolution. However, one limitation of tipper data is that they are only able to detect relative changes in resistivity. In contrast, the lower frequency MT data with broader station spacing produced an inversion model with absolute resistivity values and deeper structure. The joint inversion in Chapter 6 sought to use both datasets to create an inversion model with the advantages of both techniques. The joint inversion models improved upon the individual ZTEM and MT inversion models by synthesizing information from these complementary datasets. This chapter will address the reasons for similarities and differences in resistivity features between the three inversion models. The ZTEM and MT inversions presented in this thesis have also imaged similar features to previous EM studies of the Morrison deposit. This includes 2-D inversions of the same ZTEM data (Legault, 2013), an Aeroquest time domain electromagnetic (TEM) survey (Mitchinson et al., 2013), and magnetic data collected in each airborne survey (Aeroquest Surveys, 2009).

The individual ZTEM and MT inversion models and the joint ZTEM-MT model were compared to address the objective of this thesis: Is there value in conducting a small-scale MT survey to supplement a ZTEM survey? ZTEM case studies have been published for several types of mineral deposits including porphyry copper, massive sulfide, and unconformity uranium, and there is interest in incorporating additional geophysical information to further improve the

ZTEM results (Kaminski et al., 2010; Orta et al., 2013). The MT method is a natural choice to integrate with ZTEM inversion because of its sensitivity to deeper resistivity structure and its ability to provide absolute resistivity values. The joint ZTEM-MT inversion for the Morrison deposit was more challenging to implement than the individual ZTEM and MT inversions, but provided more information than the individual ZTEM and MT inversions. Depending on the exploration strategy at a particular deposit, this study of the Morrison deposit suggests there is value in conducting a small-scale MT survey to integrate with the ZTEM data. However, from this study it is clear that a reasonable number of stations above the target and uniform station spacing are needed to be useful. The Morrison MT and ZTEM surveys only overlapped spatially in a small area over the deposit, and the MT stations were not uniformly spaced like the ZTEM observation points. A more uniform MT station spacing would help constrain resistivity features in the resistivity model.

7.2 Model Resistivity Features

The 3-D ZTEM and MT inversion models were presented in Chapter 5. The ZTEM inversion used airborne tipper data at five frequencies in the range 360 – 30 Hz collected in a 38 km² area around the Morrison deposit. The MT inversion used impedance data at 12 frequencies between 132 – 0.7 Hz to allow for some frequency overlap with the ZTEM data. The MT survey area was about 20 km² and did not extend as far to the northeast as the ZTEM survey. The individual ZTEM and MT inversion models contained similar resistivity features due to hydrothermal alteration zones and geologic features. However there are noticeable differences including the resistivity values associated with these features.

Chapter 7: Interpretation

The joint inversion tests in Chapter 6 varied the weight of the MT data in separate inversions. The contributions from each dataset were made clear by studying the model structure as the MT data weight was gradually increased. The MT data provided resistivity value constraints for the joint inversions, and also provided improved depth resolution compared to the ZTEM-only inversions.

The features from the inversions and additional geophysical studies will be considered in two categories: geologic and alteration related (Table 7.1).

Feature	Geology or Alteration	3D ZTEM	3D MT	3D joint ZTEM-MT	2D ZTEM	AeroTEM tau data
R1	Lower Jurassic Hazelton Group volcanics and sediments	Highly resistive	Highly resistive	Highly resistive	Highly resistive	Highly resistive
R2	Potassic alteration assoc. with Eocene Babine intrusives	Highly resistive	Moderately resistive	Moderately resistive	Moderately resistive	Highly resistive
C1	Quaternary glaciolacustrine fill	Moderately conductive	Highly conductive	Highly conductive	Moderately conductive	Highly conductive
C2	Sulfide halo, argillic clay minerals, or faulting	Moderately conductive	Highly conductive	Weakly conductive	Moderately conductive	Weakly conductive

Table 7.1: Resistivity features at the Morrison deposit. The second column indicates the geologic or alteration feature interpreted to cause the resistivity feature. Columns 3 – 7 list whether or not the features were present in various EM studies.

7.2.1 Deposit Lithology

The deposit geologic setting was described in Chapter 3, and will be briefly reviewed here. The Morrison deposit is located over a stock of Eocene Babine Igneous Suite Biotite Feldspar Porphyry (BFP) intrusives. This main stock is offset about 300 m by a north trending dextral strike-slip fault. To the west there are three thin, north-northwest trending BFP dikes

Chapter 7: Interpretation

adjacent to the central BFP stock. The intrusives are hosted by Middle-Late Jurassic Bowser Lake Group (MLJB) sediments, which are confined within the northwest trending Morrison Graben. The area west of the graben is overlain by Quaternary sediments, while Lower Jurassic Hazelton Group volcanics and sediments are present to the east. The ZTEM and MT inversions are able to image these features based on properties that produce a low resistivity such as pore connectivity and presence of fractures.

The main deposit lithologies are well resolved by the individual ZTEM and MT inversions. Volcanic rocks tend to have a higher resistivity because of their crystalline form and lack of fluid pore space compared to sedimentary rocks. The Lower Jurassic Hazelton Group (LJHG) volcanic sequence is represented by a prominent resistive feature R1 ($> 1000 \Omega\text{m}$) in the ZTEM and MT inversion models (Figure 7.1). The position of this resistive feature to the northeast of the Morrison Graben correlates well with the known geology. Since vertical magnetic field data such as ZTEM data sharply define conductive boundaries, it is a well defined feature in the ZTEM tipper inversion and also appears in the MT impedance inversion. R1 extends about 1 km further to the northeast in the ZTEM inversion since the ZTEM survey area was larger than the MT. In the MT model R1 is in the same position as the ZTEM model but the northeastern edge is not constrained due to a lack of MT stations.

The Quaternary sediments (QS) to the southwest of the deposit appear as the large conductive zone C1 in the ZTEM model (Figure 7.1). This is typical of recent glaciolacustrine deposits that have large amounts of fluid pore space. The edge of this low resistivity zone correlates well with the western edge of the Morrison Graben, representing the interface between the QS and the MLJB sedimentary rocks within the graben. This interface is not as sharply defined in the MT model. Although there is a low resistivity within the QS area, the lack of MT

stations over the QS gives the model a patchy appearance. This was due to Morrison Lake to the west of the Morrison graben making it impossible to collect ground MT data in this area.

In the joint inversion the features R1 and C1 do not change appreciably as the MT weighting is increased (Figure 7.2) since these resistivity features were present in the individual ZTEM and MT inversions. However, as the MT error is lowered below 5%, R1 and C1 are less distinguishable because the inversion does not closely fit the MT data, resulting in a model that remains close to the starting 1000 Ωm halfspace.

7.2.2 Hydrothermal Alteration

The alteration at Morrison is concentrically zoned over the main BFP intrusive stock. The central potassic core grades outward into a propylitic halo, with argillic alteration overprinting other alteration types. The resistive feature R2 (Figure 7.1) appears in the ZTEM and MT inversions and matches the location of the main BFP intrusive stock. This is likely the signature of the potassic core as well as the BFP intrusive dikes to the northwest of the deposit. In the ZTEM model, R2 has a high resistivity at shallower depth (633 m elevation above sea level) but is not as clearly defined 150 m deeper (483 m elevation). However in the MT model, R2 is present but not highly resistive at 633 m elevation. At 483 m elevation R2 is more resistive and matches the location in the ZTEM model. It is possible that the lower frequency MT data have more resolution than the ZTEM data at 483 m elevation since this is about 300 m below the surface. The Morrison deposit is outlined in Figure 7.1 but does not appear as a strong resistivity anomaly in either the ZTEM or MT inversions. The porphyry deposit model in Figure 3.3 predicts a higher resistivity at the deposit core associated with potassic alteration, but the

inversions show that the highly resistive feature R2 is closely associated with the intrusive dikes to the northwest of the Morrison deposit.

The conductor C2 is also a prominent feature in both inversion models. In the ZTEM model C2 is a moderately conductive feature to the northeast of the Morrison orebody, but it becomes less distinguishable at 483 m elevation. In the MT model C2 appears as a strong conductor at both 633 m and 483 m elevation. As in the case of R2, this suggests that the lower frequency MT data have resolution at 483 m elevation while the ZTEM resolution has decreased due to signal attenuation. C2 is possibly a portion of the propylitic alteration halo with a high conductivity due to the presence of disseminated sulfides, explaining the resistivity contrast adjacent to the potassic core. C2 may also be a fault-controlled resistivity feature since it matches well with the eastern edge of the Morrison Graben. However, neither inversion model shows a continuous low resistivity along the eastern edge of the graben. This suggests that the low resistivity of C2 is in part influenced by alteration at the deposit. A low resistivity is also consistent with the presence of clay minerals, the product of argillic alteration. Argillic alteration at Morrison overprints potassic and propylitic alteration, and may be another explanation for C2 (Mitchinson et al., 2013; Liu, 2015).

R2 and C2 are stable features in the joint inversion models, as seen in horizontal sections at 483 m elevation (Figure 7.2). The resistivity values of R2 and C2 change as the MT weighting is increased, which suggests that the joint inversion is incorporating the resistivity magnitudes provided by the MT data. For MT error lower than 10%, the resistivity features become less discrete as a result of the inversion not being able to closely fit the MT data.

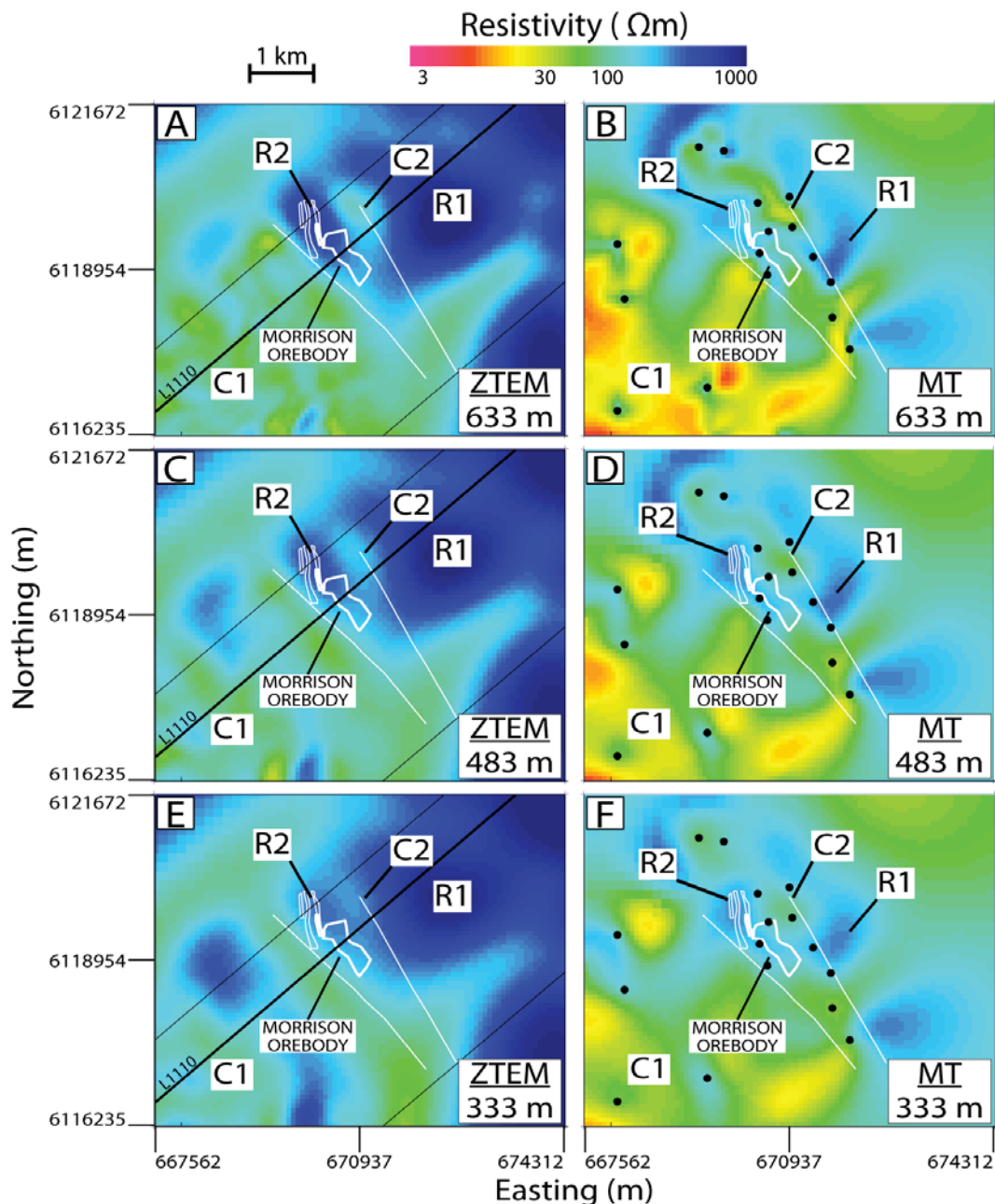


Figure 7.1: Horizontal slices through ZTEM inversion model (A,C,E) and MT inversion model (B,D,F) at 633 m, 483 m, and 333 m elevation above sea level. Red colors represent conductive features while blue features are more resistive. The Morrison orebody and 3 BFP dikes are outlined in white, along with the bounding faults of the Morrison Graben. Black dots are MT station locations. The flight line L1110 is the profile for the vertical sections. Thin black lines show the spatial extent of the ZTEM survey. The resistive feature R2 and the conductive C2 may be associated with hydrothermal alteration, and appear in both the ZTEM and MT models. C1 and R1 are consistent with the known deposit lithologies.

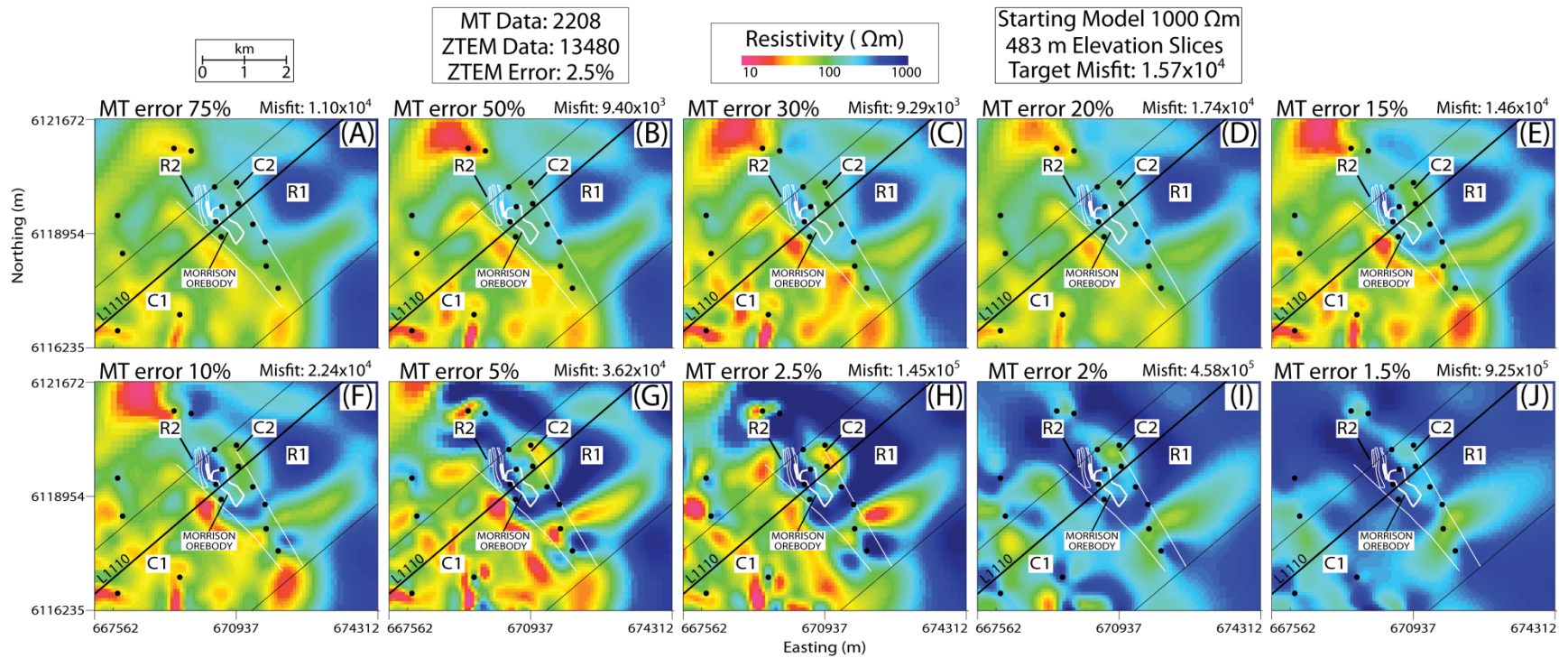


Figure 7.2: Horizontal slices at 483 m elevation through joint ZTEM-MT inversion models. From panels A to J the MT data error is decreased in order to increase the relative weight of the MT data in the joint inversion. The diagonal thick black line represents flight line L1110. The main BFP stock and dikes are overlain in white, along with the bounding faults of the Morrison Graben. Black circles are MT stations and thin black lines are the extent of the ZTEM survey. As the MT data error is decreased, the relative weighting of the MT data in the inversion is increased. In panels A-H it is clear that the inversion is incorporating information about absolute resistivity values from the MT data. The inversions in panels I and J were not able to fit the ZTEM and MT data, and do not contain the same features as the other inversions.

7.2.3 Summary of Resistivity Features

The ZTEM and MT inversion models contain most of the same features around the Morrison deposit. The low resistivity QS glaciolacustrine sediments (C1) and high resistivity LJHG volcanics (R1) are present in both models to the southwest and northeast of the Morrison Graben, respectively. Both models also contain smaller features likely due to hydrothermal alteration. R2 is present in the ZTEM and MT models, and is more resistive in the MT model about 300 m below the surface. The high resistivity is likely due to the contrast between the BFP intrusive and the host sedimentary rocks in the Morrison Graben. C2 appears in both the ZTEM and MT models northeast of the main BFP stock. This feature is more subtle in the ZTEM model and is more resistive around 300 m below the surface. In contrast the MT model shows C2 as a strong conductor that is well defined even to 300 m depth.

Since ZTEM data do not contain electric field information, the model resistivity values depend greatly on the choice of resistivity used for the starting model. Compared to the ZTEM model, the joint inversion models contain larger resistivity contrasts when the MT data are introduced. The large shallow conductor associated with the Quaternary glaciolacustrine sediments becomes a lower resistivity feature when the MT error is 50 – 15%. The R1 resistor also increases in resistivity when the MT error is decreased from 50% to 10%. This suggests that the MT impedance data are providing absolute resistivity values for these model features. While the ZTEM data accurately resolve contrasts in resistivity, the addition of MT impedance data appears to make these contrasts sharper and closer to their actual resistivity values.

The deposit lithologies associated with R1 and C1, as well as the alteration likely associated with R2 and C2 are stable features as the MT weighting is increased in the joint inversions. However, as the MT error is lowered below 5% (G – J) the inversion misfit is much

Chapter 7: Interpretation

larger than the target misfit and the model features are not as distinct. It is clear in these inversions that the MT error is too low for the inversion to acceptably fit the data. Additional reweighting of the two datasets may be required to obtain a reasonable inversion result with these small MT errors.

The expected improvement in depth resolution is seen in Figure 7.3 when jointly inverting the ZTEM and MT data. As shown in Chapter 2, the penetration depth of an EM signal is dependent on the signal frequency and the resistivity of the ground. Considering the lowest frequencies for the ZTEM (30 Hz) and MT (0.7 Hz) surveys, the penetration depth is about 1 km for the ZTEM data and about 6 km for the MT data in a uniform 100 Ωm earth. This implies that a joint ZTEM-MT inversion should have deeper resolution than the individual ZTEM inversion. The vertical sections in Figure 7.3 panels F – H clearly show that deeper structure is being imaged with the addition of the lower frequency MT data. However, further trial inversions are needed to improve the data fit in panels F – H.

If the ZTEM and MT data are not equally weighted, the inversion can converge to an acceptable misfit by only adding shallow structure to satisfy the higher frequency ZTEM data. The approach to joint inversion presented in Chapter 6 gradually increased the MT data weighting by decreasing the errors on the MT data in the joint inversion. However, even when the MT error is set to 10% of the data, the weighting parameter γ is not equal to the number of ZTEM data divided by the number of MT data. When γ approaches this value (Figure 7.3; panels G – J), the inversion misfit is unacceptably high. From inspecting the data misfit, the low frequency MT data are poorly fit when the two datasets approach equal weight. In addition the inversion appears to preferentially change shallow portions of the model where there is an overlap in ZTEM and MT frequencies.

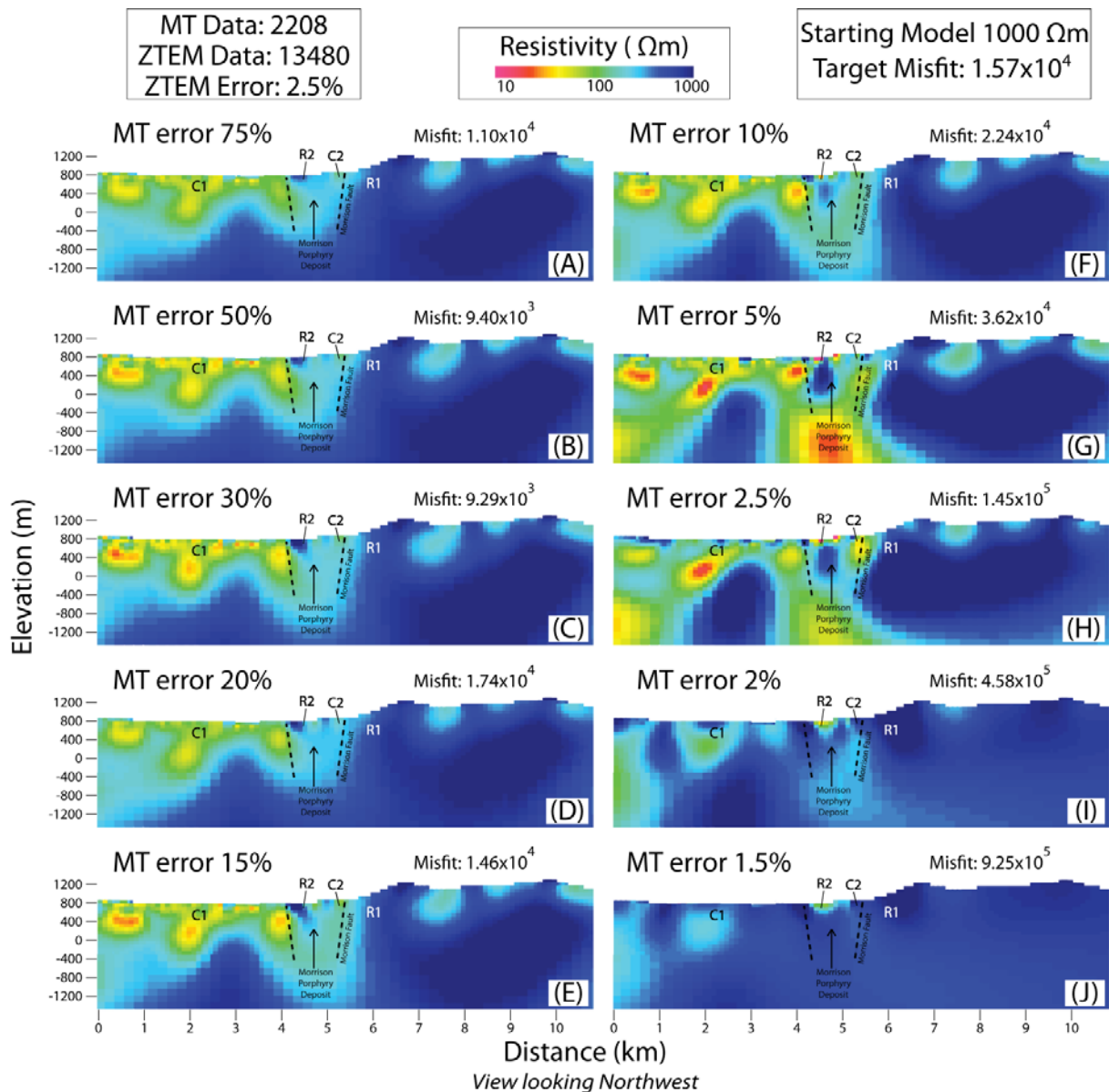


Figure 7.3: Vertical slices along ZTEM flight line L1110 through joint inversion models. Between panels A – J the MT error is lowered to increase the relative weighting of the MT data in the joint inversion. The resistivity models in panels A – E are not very different from the ZTEM-only model since the inversion does not closely fit the MT data. In panels F – H the joint inversion is clearly adding deeper structure that is required as the MT weighting is increased. In panels I – J the MT data error is too low and the inversion cannot closely fit the data or recover a reasonable model.

7.3 Previous EM and Aeromagnetic studies at Morrison

Additional geophysical and geologic studies are available to compare with the ZTEM and MT inversion results. The Geotech 2-D ZTEM inversion, airborne magnetic survey, and AeroTEM late-time tau data provide geophysical information that will be related to the ZTEM and MT inversions. Geologic knowledge of alteration zones and mineralization also contribute to understanding resistivity features in the inversion models.

7.3.1 Geotech 2-D ZTEM

Using the same ZTEM data as the previous 3-D inversions, Geotech Ltd. performed a 2-D ZTEM inversion along flight line L1110 (Legault, pers. comm., 2013). The inversion included topography changes along the profile and began from a 1000 Ωm halfspace. The model is shown in Figure 7.4 (panel B), and bears close resemblance to the 3-D ZTEM inversion (panel A). The western part of the profile contains a shallow conductive zone (C1) corresponding to the QS sediments, while the eastern resistive half correlates with the LJHG volcanics (R1). Both resistivity models show the outcropping resistive Morrison deposit associated with BFP intrusives and the potassic alteration zone (R2). The deposit is flanked on both sides by more conductive features that correlate with the Morrison Graben bounding faults. As previously mentioned, these conductive features may be due to pyrite enrichment outside of the potassic alteration zone, or clay minerals from argillic alteration. The main difference from the 3-D inversion slice is the large conductive body that extends to 2 km depth. This feature does not appear in the corresponding 3-D inversion slice in panel A and may be an artifact of the 2-D inversion. The 2-D inversion is susceptible to features that are off profile, and may compensate by smearing features deeper in the model. Even so, the main deposit features are clearly defined in both the 2-D and 3-D inversion models.

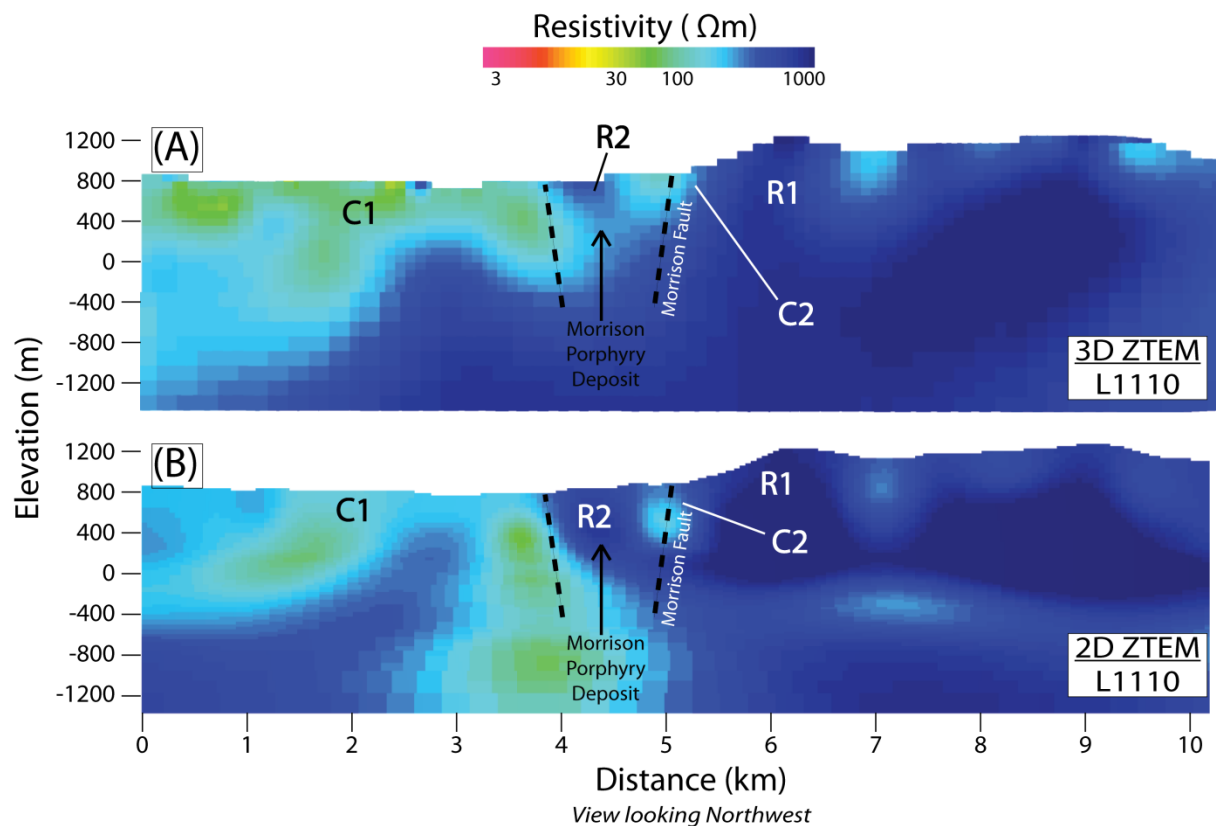


Figure 7.4: Panel A: Vertical section through flight line L1110 of the preferred 3-D ZTEM inversion from Chapter 5 and B) 2-D ZTEM inversion by Geotech Ltd. of Morrison flight line L1110. Both inversions started with a 1000 Ωm starting model. The 2-D inversion used the in-line T_{zx} component at five frequencies between 360 – 30 Hz. The deposit potassic zone and flanking conductors correlate very well with their positions in the 3-D ZTEM inversion. (Modified from Legault, pers. comm., 2013.)

7.3.2 Aeromagnetic Data

The magnetic response of a porphyry deposit is dominated by the spatial distribution of magnetite from intrusive bodies. At Morrison the Eocene Babine Intrusives are hosted by the MLJB sediments, so magnetite should cause local positive magnetic anomalies because there is likely a negligible amount in the host sedimentary rock. This can be seen in the magnetic data collected over the Morrison deposit during the Aeroquest AeroTEM survey in 2009 (Figure 7.5, panel C). The R2 resistor in the ZTEM and MT inversion models matches well with the

Chapter 7: Interpretation

magnetic highs for the intrusive dikes and northwest half of the main BFP stock. In the southeast half of the BFP stock there is a local magnetic high centered on the zone of potassic alteration that did not appear particularly resistive in the ZTEM and MT inversions. The location of the C2 conductor coincides with a magnetic low adjacent to the main BFP stock. This suggests an absence of magnetite, possibly caused by distal propylitic alteration. The QS and MLJB sediments appear nonmagnetic, while the mafic volcanic LJHG appears as a magnetic high to the east of the deposit.

The magnetic high located over the Morrison deposit is likely associated with high magnetite content in the potassic alteration zone (Figure 3.3). The potassic alteration is also expected to be highly resistive, but the ZTEM and MT inversion models do not contain a highly resistive feature coinciding with the location of the deposit; in fact the highly resistive feature R2 appears to be correlated more strongly with the intrusive dikes to the northwest of the deposit.

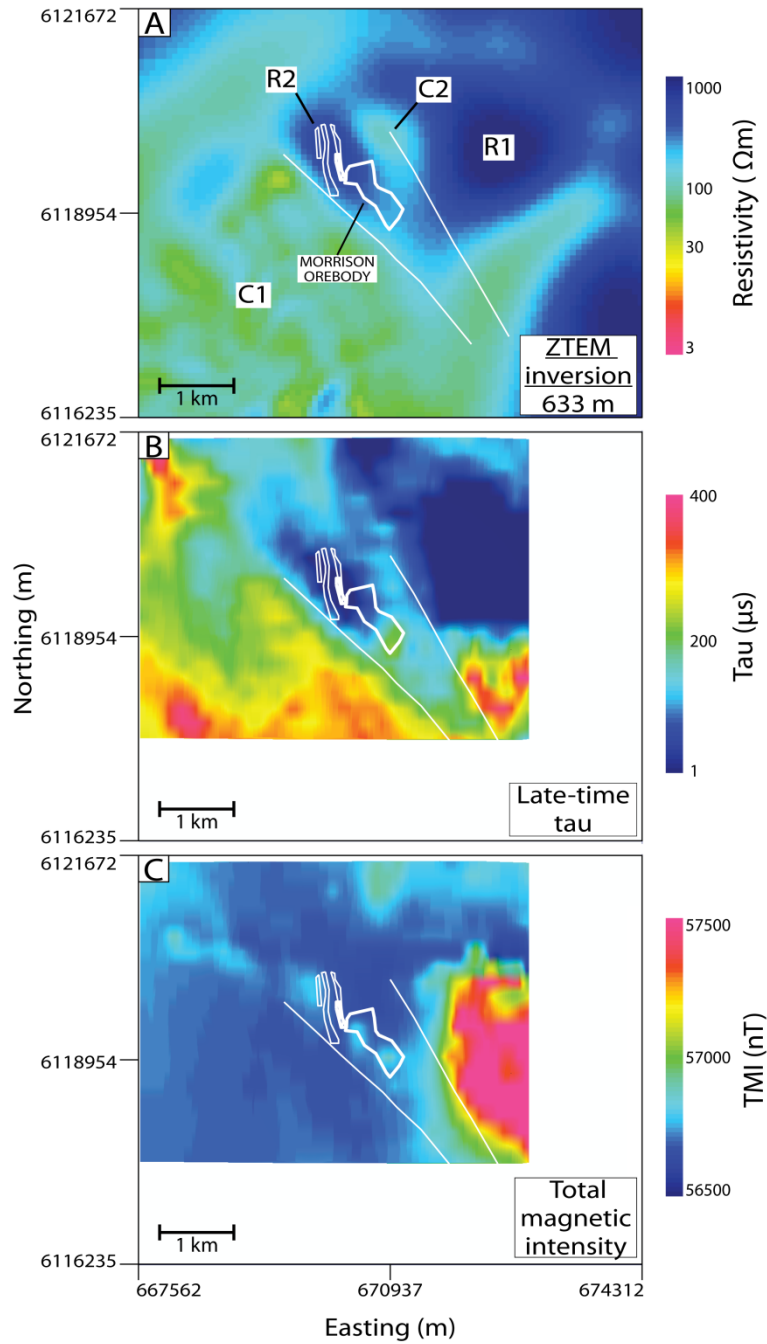


Figure 7.5: Comparison of ZTEM inversion resistivity model, TEM late-time tau data, and airborne total magnetic intensity map of the Morrison deposit. Panel A: Horizontal section of the ZTEM only inversion at 633 m elevation above sea level. Panel B: AeroTEM late time tau map from Aeroquest Surveys (2009). Larger values of tau correspond to lower resistivity. Panel C: Morrison total magnetic intensity map from Aeroquest Surveys (2009).

7.3.3 AeroTEM Late-time Tau

In time domain electromagnetic (TEM) surveys, a transmitter induces electric currents in the Earth and the temporal decay of these currents is monitored by measurements of the magnetic fields generated by these currents (Figure 7.6). In a conductive earth the electric currents are able to flow for a longer period of time, and the induced magnetic field decays at a higher rate during late time.

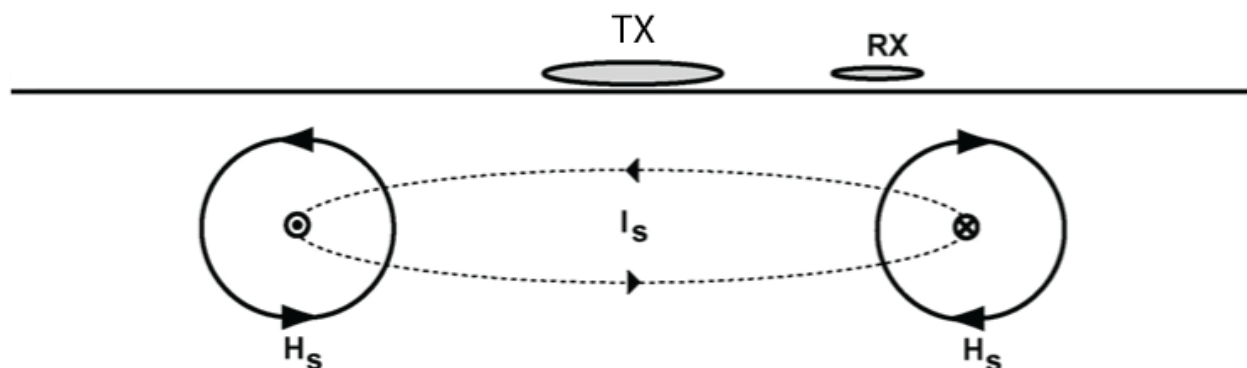


Figure 7.6: Time domain electromagnetic (TEM) survey with transmitting loop (TX), receiver (RX), secondary electric current (I_s) and induced secondary magnetic field (H_s). The resistivity of the Earth is determined by measuring the time decay of the secondary magnetic fields at the receiver. Modified from Unsworth, (2014).

Maps of a decay constant, tau, show which areas are relatively conductive (i.e. current flows for a longer time, and higher tau values) or resistive (lower tau values). Figure 7.5, panel B, shows the late time tau map for the Morrison deposit. Higher values of tau correspond to regions with lower resistivity. The higher tau values in Figure 7.5 to the southwest of the Morrison deposit match well with the low resistivity zone seen in the ZTEM and MT models. This area is interpreted as the Quaternary glaciolacustrine deposits around Morrison Lake. The low tau values to the northeast of the deposit correlate well with the high resistivity feature seen in the ZTEM and MT. Both match the known location of the LJHG volcanic to the east of the Morrison Graben. Within the deposit, there is a low tau anomaly that covers the northwestern

half of the main BFP stock and the three intrusive BFP dikes. This matches the location of the R2 resistor seen in both the ZTEM and MT inversion models. In the southeast half of the central BFP stock, there is a slightly elevated tau that could be explained by disseminated sulfides outside the potassic alteration zone or clay minerals in argillic alteration along the bisecting fault. C2 does not appear as a strong tau anomaly in late-time tau map.

It is important to note that similar to the frequency domain EM (i.e. ZTEM and MT) skin depth, the sampling depth of a time domain survey depends on the resistivity of the subsurface. However, in a TEM survey late-time measurements of the secondary magnetic field H_s correspond to a greater sampling depth. In principle the secondary magnetic field, H_s , or the decay of the secondary magnetic field over time, dH_s/dt , decreases rapidly during late-time and can only be measured above the noise floor specified by the equipment. The TEM sampling depth (analogous to frequency domain EM skin depth) can be approximated in a halfspace as

$$\delta_T = \frac{1}{2.3} \sqrt{\frac{2\rho t}{\mu}} \quad (7.1)$$

where δ_T is the sampling depth, ρ is the resistivity of the halfspace, t is the measurement time of the secondary magnetic field, and μ is the magnetic permeability (Unsworth, 2014).

Equation 7.1 can be used to estimate the depth that is sampled in the late-time tau map shown in Figure 7.5, panel B. For example, in a low resistivity area the tau value will be relatively high. Using representative values of 400 μs for tau and a resistivity of 10 Ωm and assuming the free space value of magnetic permeability, the sampling depth δ_T is 35 m. In a more resistive environment where tau is 100 μs and the resistivity is 1000 Ωm , the sampling depth is 175 m. While these are rough estimates for the TEM sampling depth, this calculation

shows that the TEM method should be sensitive to near-surface resistivity features in a shallow porphyry deposit such as the Morrison deposit.

7.4 Implications for Exploration at the Morrison Deposit

The joint ZTEM-MT inversion yielded a resistivity model that contained all the resistivity features seen in the individual ZTEM and MT inversion models (Table 7.1). Since the MT data contained lower frequencies than the ZTEM there was a conductive structure resolved at greater depth in some joint inversions than the individual ZTEM inversion. Despite this result, the correct weighting of the datasets could not be implemented without decreasing the MT error to unreasonable amounts. When the MT error was lowered below 10%, the data misfit was unacceptably high and the resistivity models became either unstable or did not change from the starting model. The ZTEM data were much smoother than the MT data, so smaller MT errors prevented the inversion from closely fitting the MT data and resulted in an inappropriately large misfit. One way to alleviate the disparity in data points is to collect more MT stations around the area of interest, particularly in a regular array (Sattel and Witherly, 2015).

7.5 Implications for Mineral Exploration

The objective of this study was to find out if there is value in collecting ground MT stations to complement an airborne ZTEM survey. From comparison of the two individual inversion models it is clear that the tipper-only ZTEM data are able to image most of the same features as the MT impedance data. The consistency of the ZTEM, MT, and joint ZTEM-MT inversions shows that even without a follow-up MT survey, the ZTEM data may be enough to create a realistic resistivity model. For the Morrison deposit a small-scale MT survey benefited

the inversion process by providing apparent resistivity values to guide the choice of starting model resistivity. Otherwise there would have to be more trial and error in the ZTEM inversion to find a realistic starting model. When the MT data weight was increased in the joint ZTEM-MT inversion, resistivity contrasts from the ZTEM data became stronger and perhaps closer to their true resistivity values. This suggests that MT impedance data could supplement the ZTEM inversion by providing more accurate resistivity values for strong anomalies. The joint inversions also showed that deeper structure from the lower frequency MT data can be incorporated into the joint resistivity model at the correct relative weighting.

While the joint inversion implemented information from both the ZTEM and MT data, it is important to use data in overlapping frequency bands. At frequencies below the lowest ZTEM frequency of 30 Hz, the MT data are sampling greater depths than the ZTEM data. Using low frequency data (> 0.01 Hz) may not benefit the joint inversion because they are sensitive to structure far deeper than the depth of interest for mineral exploration. While lower frequency MT data may provide more information at depth, incorporating both datasets at the same high frequencies will allow the inversion to place shallow structure based on information from both datasets.

Finally, incorporating topographic information into the inversion model is especially important for ZTEM inversions. It is important to place the ZTEM observation points at their proper locations above the ground, especially with large topographic changes as seen in the Morrison survey area. The topographic response in the tipper data can be significant at high frequencies so it is important to have finely discretized model cells to accurately reflect topographic variations.

7.6 Summary

While the methodology of joint ZTEM-MT inversion is still under continued development, these results show that information from both datasets can be incorporated in a joint 3-D inversion. These two methods have proven effective at detecting resistivity contrasts associated with alteration at the Morrison porphyry deposit. When both datasets were used in a joint inversion, the resistivity model contained the same shallow resistivity features as the ZTEM-only inversion while including some deeper structure from the MT data at certain levels of data weighting. There are opportunities for future research on these joint inversions outlined in the following chapter.

Chapter 8: Conclusion

8.1 Summary

The ZTEM and MT methods have been shown as exploration techniques able to map resistivity contrasts associated with porphyry copper deposits. Synthetic examples of ZTEM and MT inversions demonstrate that these techniques are sensitive to the resistivity structure of an idealized porphyry deposit. I have shown that the ZTEM and MT tipper data collected at the Morrison deposit correlate well in the overlapping frequency range 360 – 30 Hz. In addition, separate inversions of the Morrison ZTEM tipper data and MT impedance data resulted in models with very similar resistivity features. This shows that airborne ZTEM surveys, which are fast to deploy and have dense spatial resolution, could be a reliable alternative to slower ground-based electromagnetic induction methods like MT. The resistivity features in the ZTEM and MT inversions are also seen in aeromagnetic and airborne time-domain EM surveys conducted over the Morrison deposit. Finally, joint ZTEM-MT inversion was attempted to utilize the high spatial sampling of ZTEM data and the depth resolution and absolute resistivity information from MT data. Incorporating the MT data in the joint inversion changes the magnitude of resistivity contrasts resolved by the ZTEM data. Deeper structures in the joint resistivity models required by the lower frequency MT data are also resolved in some joint inversions. However, the two datasets were not able to be appropriately weighted so that they equally influence the inversion. I have also shown that it is possible to decrease the relative weight of the ZTEM data in the joint inversion by taking a small subset (about 5%) of the original data without significantly changing the data fit or model.

8.2 ZTEM and MT Inversions

The ZTEM method relates airborne measurements of the vertical magnetic field to measurements of the horizontal magnetic fields at a ground base station. The resulting tipper data are sensitive to lateral resistivity contrasts. The ground based MT method relates orthogonal electric and magnetic fields measured at the earth's surface to obtain an average subsurface resistivity. Even though the ZTEM tipper data and MT impedance data are collected in drastically different ways and give different information about subsurface resistivity, the individual inversions resulted in similar models. The resistivity features resolved by the ZTEM and MT inversions include a shallow resistor coincident with the known potassic alteration zone and a conductor that correlates with sulfide enrichment in the pyrite halo or fractures along a known fault. However, the resistivity model is not enough to determine the extent of mineralized zones, as the ZTEM and MT techniques are most sensitive to bulk physical properties that enhance or inhibit electrical current flow. At porphyry deposits such as Morrison, where much of the mineralization is contained in disseminated sulfides, the resistivity response will not be as strong as mineralization developed in interconnected veins. Thus a ZTEM or MT survey alone may not be enough to define specific targets within a porphyry deposit. Additional geophysical information, such as the aeromagnetic survey shown in section 7.3.2 which was sensitive to the magnetic high in the Morrison deposit, should be incorporated when possible. Both techniques are also sensitive to the relatively conductive ($\sim 10 \Omega\text{m}$) Quaternary lake sediments and resistive ($\sim 1000 \Omega\text{m}$) Jurassic volcanics and sediments adjacent to the deposit. The ZTEM inversion displayed impressive depth resolution for an airborne method (about 1 km). The MT inversion was sensitive below 2 km, but the data was not adequately fit at the lowest frequencies.

8.3 Joint ZTEM-MT Inversion

The ZTEM technique is a cost-effective way to rapidly explore mineral deposits up to about 2 km depth. While ZTEM provides excellent spatial sampling (about every 10 m along flight lines) the tipper data do not provide information about resistivity magnitudes and have limited depth resolution in conductive environments at 360 – 30 Hz frequency. Broadband MT operates at much lower frequencies (up to 0.001 Hz) allowing for much greater depth resolution. However, MT requires ground contact and may be extremely costly to deploy in a dense array. Jointly inverting both datasets is a solution to bring out the advantages of both techniques. A densely sampled ZTEM dataset provides good resolution at higher frequencies while a sparse MT survey can provide constraint on background resistivity values and deeper structure.

The field example from the Morrison deposit shows that the MT data indeed change resistivity values of contrasts defined by the ZTEM data. The joint inversion was also able to incorporate deeper structure in the resistivity models when the MT data were weighted within a certain range. Since there may be at least an order of magnitude more ZTEM data points than MT data points, the two datasets need to be properly weighted to influence the inversion approximately equally. In Chapter 6 the MT error floor was varied to test different weighting in the inversion. The joint inversion obtained a resistivity model containing the same features as the individual inversions, but more trial inversions need to be run to properly weight the two datasets. One inconsistency encountered was the non-uniform MT station spacing compared to the uniformly sampled ZTEM data. In an ideal case, a uniform grid of MT stations jointly inverted with ZTEM data would constrain the resistivity model equally in all areas.

The deep conductor seen underneath the Morrison deposit (Figure 7.3) only appears in the joint inversions when the MT data error is set at 5% and 2.5%. Since the MT data were not fit

Chapter 8: Conclusion

at every station at the lowest frequencies, this low resistivity feature may be an artifact of the inversion. In fact, the synthetic MT inversion (Figure 2.13) and joint ZTEM-MT inversion (Figure 6.2) both contained an artificial conductor below a shallow resistive body. Further synthetic studies, such as removal of the conductive body below the Morrison deposit, are required to test the validity of this feature.

The Morrison joint inversion shows that information from ZTEM and MT data can be incorporated into a resistivity model. However, extra survey planning is required to collect ground-based MT data in addition to an airborne ZTEM survey. In addition it is currently faster and more inexpensive to use 2-D inversion algorithms to create resistivity models. More accessible and faster 3-D inversion algorithms may be required for exploration companies to fully implement the joint 3-D ZTEM-MT approach in porphyry deposit exploration.

8.4 Opportunities for Further Work

While the individual ZTEM and MT inversions obtained comparable resistivity models for the Morrison deposit, more work can be done to prepare the two datasets for joint inversion. For instance, a smaller spatial subset of each dataset could be used to match the starting model of each inversion. While the two datasets overlap in an approximately 30 km² area, the MT survey extended over conductive glaciolacustrine sediments to the southwest while the ZTEM survey extended over the relatively resistive mafic volcanics to the northeast. Excluding these areas from the 3-D modelling may allow each dataset to be inverted from the same starting resistivity model. This is especially important for the ZTEM inversion which relies heavily upon the starting model to determine resistivity contrasts.

Chapter 8: Conclusion

Further work must also be done to properly weight the ZTEM and MT datasets for joint inversion. Since there are typically many more data points in a ZTEM survey than an MT survey, the data misfit term must be scaled proportionally to the number of data in each survey. No scaling should be necessary if there is the same number of data points in each dataset. While the ZTEM dataset was reduced to 13,480 data points compared to 2,208 MT data points, the MT error could not be lowered enough for each dataset to equally influence the joint inversion. In Chapter 5, an inversion of the downsampled ZTEM dataset containing about 5% of the original dataset (13,480 data points) still resulted in a similar resistivity model as inverting the entire dataset. This was an important first step in approaching the same number of data for the ZTEM and MT. Another possible approach is to reweight the two datasets by adjusting the errors on both simultaneously. For example, increasing the errors on the ZTEM data while decreasing the errors on the MT data would bring the weighting closer to equal if there are still many more ZTEM data points than MT data points. Similarly, the MT error could be held constant while the ZTEM data error is increased to effectively increase the weight of the MT data. These approaches would require more test inversions to determine the optimal weighting for each case.

Further improvements to the airborne ZTEM system could potentially reduce survey time and cost. For example, adapting the ZTEM system for use by an unmanned aircraft system (UAS) could substantially reduce the survey cost by removing the cost of helicopter operation. An unmanned system would still have the benefits of constant surveying velocity and altitude. One obstacle is being able to adapt the vertical sensor for towing by the UAS. The noise characteristics of an UAS would also have to be studied and the data processing scheme adjusted accordingly. If this technology is eventually implemented, the ZTEM survey could be performed faster and more efficiently without sacrificing data quality.

Chapter 8: Conclusion

For mineral exploration it is important to incorporate as much geophysical and geologic information as possible when interpreting a target. Another inversion strategy involving ZTEM and MT would be to impose constraints from other types of data. For example, borehole resistivity measurements could help provide background resistivity values at target areas of a mineral deposit. This could particularly help a ZTEM inversion recover resistivity contrasts at the correct resistivity magnitudes.

References

- Abbassi, B., Huebert, J., Liu, L., Lee, B., Cheng, L., Richards, J. P., Unsworth, M. J., and Oldenburg, D., (2013). 3D inversion of magnetic and electrical resistivity-induced polarization data for an epithermal Au-Ag and underlying porphyry deposit: A case study from British Columbia, Canada. *American Geophysical Union, Fall Meeting 2013, abstract NS43A-1794*.
- Aeroquest Surveys, (2009). Report on a helicopter-borne AeroTEM system electromagnetic & magnetic survey; Geoscience BC Report.
- Backus, G.E. and Gilbert, J.F., (1967). Numerical application of a formalism for geophysical inverse problems. *Geophys. J. R. astr. Soc.*, **13**, 247-276.
- Bertrand, E., Unsworth, M., Chiang, C. W., Chen, C. S., Chen, C. C., Wu, F., and Hill, G., (2009). Magnetotelluric evidence for thick-skinned tectonics in central Taiwan. *Geology* **37**(8), 711-714.
- British Columbia Geological Survey, (2005). BCGS Geological map, Mapplace.ca.
- Cagniard, L., (1953). Basic theory of the magnetotelluric method of geophysical prospecting, *Geophysics* **18**, 605-635.
- Clark, D. A., (2014). Magnetic effects of hydrothermal alteration in porphyry copper and iron-oxide copper–gold systems: a review. *Tectonophysics* **624**, 46-65.
- Clark, D. A., French, D. H., Lackie, M. A., Schmidt, P. W., (1992). Magnetic petrology: application of integrated rock magnetic and petrological techniques to geological interpretation of magnetic surveys. *Exploration Geophysics* **23**, 65-68.
- Commer, M., and Newman, G. A., (2009). Three-dimensional controlled-source electromagnetic and magnetotelluric joint inversion. *Geophys. J. Int.* **178**, 1305-1316.
- Farquharson, C.G., Oldenburg, D. W., Haber, E., and Shekhtman, R., (2002). An algorithm for the three-dimensional inversion of magnetotelluric data. Proceedings of the 72nd Annual International Meeting, *SEG Expanded Abstracts*, 649-652.
- Geotech Ltd., (2010). ZTEM Tipper AFMAG Results over the Morrison Copper/Gold Porphyry deposit. *Geotech.ca/papers/*
- Gunn, P. J., & Dentith, M. C., (1997). Magnetic responses associated with mineral deposits. *AGSO Journal of Australian Geology and Geophysics* **17**, 145-158.

References

- Gurk, M., Bosch, F. P., and Tougiannidis, N., (2013). Electric field variations measured continuously in free air over a conductive thin zone in the tilted Lias-epsilon black shales near Osnabrück, Northwest Germany. *Journal of Applied Geophysics* **91**, 21-30.
- Holliday, J. R., & Cooke, D. R., (2007). Advances in geological models and exploration methods for copper±gold porphyry deposits. *Proceedings of Exploration* **7**, 791-809.
- Holtham, E. M., (2012). 3D Inversion of Natural Source Electromagnetic Data. Unpublished Ph.D. Thesis, The University of British Columbia, Vancouver, Canada, 137 p.
- Holtham, E., & Oldenburg, D. W., (2010). Three-dimensional inversion of ZTEM data. *Geophysical Journal International* **182**(1), 168-182.
- John, D.A., Ayuso, R.A., Barton, M.D., Blakely, R.J., Bodnar, R.J., Dilles, J.H., Gray, F., Graybeal, F.T., Mars, J.C., McPhee, D.K., Seal, R.R., Taylor, R.D., and Vikre, P.G., (2010). Porphyry copper deposit model. Chap. B of Mineral deposit models for resource assessment. *U.S. Geological Survey Scientific Investigations Report 2010–5070–B*, 169 p.
- Jones, A. G., (1988). Static shift of magnetotelluric data and its removal in a sedimentary basin environment. *Geophysics* **53**(7), 967-978.
- Kaminski, V., and Oldenburg, D. W., (2012). The geophysical study of Drybones Kimberlite using 3D time domain EM inversion and 3D ZTEM inversion algorithms. 22nd International Geophysical Conference & Exhibition Conference, ASEG, Brisbane, Australia.
- Kaminski, V., Legault, J.M., and Kumar, H., (2010). The Drybones Kimberlite: a case study of VTEM and ZTEM airborne EM results. *ASEG Extended Abstracts 2010*, 1-4.
- Kelbert, A., Meqbel, N., Egbert, G. D., and Tandon, K., (2014). ModEM: A modular system for inversion of electromagnetic geophysical data. *Computers & Geosciences* **66**, 40-53.
- Lezaeta, P., Chave, A., Jones, A. G., and Evans, R., (2007). Source field effects in the auroral zone: Evidence from the Slave craton (NW Canada). *Physics of the Earth and Planetary Interiors* **164**, 21-35.
- Liu, L., (2014). Geochemistry, Geochronology, and Fluid Inclusion Study of the Newton Epithermal Gold, and Morrison Porphyry Copper Deposits, British Columbia. Unpublished M.Sc. Thesis, University of Alberta, Edmonton, Canada, 139 p.
- Lo, B., and Zang, M., (2008). Numerical modeling of Z-TEM (airborne AFMAG) responses to guide exploration strategies, *SEG Technical Program Expanded Abstracts* **27**(1), 1098–1102.
- MacGregor, L. M., Andreis, D., Tomlinson, J., and Barker, N., (2006). Controlled-source electromagnetic imaging on the Nuggets-1 reservoir. *The Leading Edge* **25**, 984-992.

References

- MacIntyre, D.G., Villeneuve, M.E., and Schiarizza, P., (2001). Timing and tectonic setting of Stikine Terrane magmatism, Babine-Takla lakes area, central British Columbia. *Canadian Journal of Earth Sciences* **38**, 579–601.
- Mackie, R. M., Watts, M. D., and Rodi, W., (2007). Joint 3D inversion of marine CSEM and MT data. *SEG Technical Program Expanded Abstracts* **26**, 574-578.
- Macnae, J., (2010). Electric Field measurements in air. *SEG Technical Program Expanded Abstracts* **29**, 1773-1777.
- Maxwell, J. C., (1861). On physical lines of force. *Philosophical Magazine*.
- McClenaghan, L., (2013), Geology and Genesis of the Newton Bulk-Tonnage Gold-Silver Deposit, Central British Columbia. Unpublished M.Sc. thesis, The University of British Columbia, Vancouver, Canada, 185 p.
- McMillan, W.J., Thompson, J.F.H., Hart, C.J.R., and Johnston, S.T., (1995). Regional geological and tectonic setting of porphyry deposits in British Columbia and Yukon Territory, in Porphyry deposits of the northwestern Cordillera of North America, *Canadian Institute of Mining, Metallurgy and Petroleum Special Volume* **46**, 40-57.
- Mitchinson, D. E., Enkin, R. J., and Hart, C. J. R., (2013). Linking Porphyry Deposit Geology to Geophysics via Physical Properties: Adding Value to Geoscience BC Geophysical Data. Geoscience BC Report 2013-14.
- Monger, J., and Price, R., (2002). The Canadian Cordillera: Geology and Tectonic Evolution. *CSEG Recorder* **2**, 17-36.
- Nelson, J., and Colpron, M., (2007). Tectonics and metallogeny of the British Columbia, Yukon and Alaskan Cordillera, 1.8 Ga to the present. In Goodfellow, W.D. (ed.); *Geological Association of Canada, Mineral Deposits Division, Special Publication* **5**, 755-791.
- Nelson, P. H., & Van Voorhis, G. D., (1983). Estimation of sulfide content from induced polarization data. *Geophysics* **48**(1), 62-75.
- Newman, G. A., and Alumbaugh, D. L., (2000). Three-dimensional magnetotelluric inversion using non-linear conjugate gradients. *Geophys. J. Int.* **140**, 410-424.
- Oldenburg, D. W., Li, Y., and Ellis, R.G., (1997). Inversion of geophysical data over a copper gold porphyry deposit: A case history for Mt. Milligan. *Geophysics* **62**(5), 1419-1431.
- Orta, M., Legault, J. M., Prikhodko, A., Plastow, G., Zhao, S., and Ulankys, C., (2013). Passive and active helicopter EM survey comparisons over the 501 Project Cu-Zn volcanogenic massive sulphide at McFauld's Lake, northern Ontario. *ASEG Extended Abstracts 2013*, 1-4.

References

- Paré, P., and Legault, J. M., (2010). Ground IP-Resistivity and Airborne Spectrem and Helicopter ZTEM Survey Results Over Pebble Copper-moly-gold Porphyry Deposit Alaska. *SEG Annual Meeting Expanded Abstracts* **29**, 1734-1738.
- Parkinson, W. D., (1959). The influence of continents and oceans on geomagnetic variations. *Geophys. J. R. astr. Soc.* **6**, 441-449.
- Pellerin, L., and Hohmann, G. W., (1990). Transient electromagnetic inversion: A remedy for magnetotelluric static shifts. *Geophysics* **55**(9), 1242-1250.
- Richards, J. P., (2009). Postsubduction porphyry Cu-Au and epithermal Au deposits: Products of remelting of subduction-modified lithosphere. *Geology* **37**(3), 247-250.
- Richards, J. P., (2011). Magmatic to hydrothermal metal fluxes in convergent and collided margins. *Ore Geology Reviews* **40**, 1-26.
- Robertson, J., (2009). Morrison Copper/Gold Project – Feasibility Study.
- Sasaki, Y., (2001). Full 3-D inversion of electromagnetic data on PC. *Journal of Applied Geophysics* **46**, 45-54.
- Sasaki, Y., Yi, M. J., and Choi, J., (2014). 2D and 3D separate and joint inversion of airborne ZTEM and ground AMT data: Synthetic model studies. *Journal of Applied Geophysics* **104**, 149-155.
- Sattel, D., & Witherly, K., (2015). The 3D joint inversion of MT and ZTEM data. *ASEG Extended Abstracts 2015*, 1-4.
- Sillitoe, R. H., (2010). Porphyry copper systems. *Economic Geology* **105**(1), 3-41.
- Simpson, R.G., (2007). Mineral resource update: Morrison project. Pacific Booker Minerals Inc. NI43-101 Report, 66 p.
- Simpson, F., and Bahr, K., (2005). Practical Magnetotellurics. Cambridge: Cambridge University Press, 270 p.
- Siripunvaraporn, W., Egbert, G., Lenbury, Y., and Uyeshima, M., (2005). Three-dimensional magnetotelluric inversion: data-space method. *Physics of the Earth and Planetary Interiors* **150**, 3-14.
- Smith, R., (2014). Electromagnetic Induction Methods in Mining Geophysics from 2008 to 2012. *Surv Geophys* **35**, 123-156.
- Smith, R.S., Wood, G.R., and Powell, B., (2010). Detection of alteration at the Millenium uranium deposit in the Athabasca Basin: a comparison of data from two airborne

References

- electromagnetic systems with ground resistivity data. *Geophysical Prospecting* **58**, 1147-1158.
- Sternberg, B. K., Washburne, J. C., and Pellerin, L., (1988). Correction for the static shift in magnetotellurics using transient electromagnetic soundings, *Geophysics* **53**(11), 1459-1468.
- Tikhonov, A.N., (1950). On determining electrical characteristics of the deep layers of the Earth's crust, *Doklady* **73**, 295-297.
- Unsworth, M., (2014). Time Domain EM Methods. *Geop 424 Class Notes, 2014*.
- Unsworth, M., Wenbo, W., Jones, A. G., Li, S., Bedrosian, P., Booker, J., and Handong, T., (2004). Crustal and upper mantle structure of northern Tibet imaged with magnetotelluric data. *Journal of Geophysical Research: Solid Earth (1978–2012)* **109**(B2).
- Vozoff, K., and Jupp, D. L. B., (1975). Joint Inversion of Geophysical Data. *Geophys. J. Int.* **42**, 977-991.
- Wannamaker, P. E., and Legault, J. M. (2014). Two-dimensional joint inversion of ZTEM and MT Plane-Wave EM data. *GeoConvention 2014 Conference Paper*, 1-4.
- Ward, S. H., (1959). AFMAG-airborne and ground. *Geophysics* **24**(4), 761-787.
- Weaver, J. T., (1994). *Mathematical Methods for GeoElectromagnetic Induction*, Res. Stud. Press, Taunton, Mass.
- Wiese, H., (1962). Geomagnetische Tiefentellurik, 11, Die Streichrichtung der Untergrundstrukturen des elektrischen Widerstandes, erschlossen aus geomagnetischen Variationen, *Geoj. Pura Appl.* **52**, 83-103.